Coupled Spatial Variability in the Sea Ice-Ocean System: From Ice Growth to Internal Waves

Laura Crews

A dissertation

submitted in partial fulfillment of the

requirements for the degree of

Doctor of Philosophy

University of Washington

2024

Reading Committee:

Craig M. Lee, Co-chair

Luc Rainville, Co-chair

Jennifer Hutchings

Program Authorized to Offer Degree:

Oceanography

University of Washington

Abstract

Coupled Spatial Variability in the Sea Ice-Ocean System:

From Ice Growth to Internal Waves

Laura Crews

Co-chairs of the Supervisory Committee:

Craig M. Lee

Luc Rainville

Ocean Physics Department, Applied Physics Laboratory

Changes in the extent, thickness, drift speed, and phenology of sea ice are altering atmosphere-ice-ocean interactions with the potential to modify climate feedback mechanisms. This dissertation shows how spatial heterogeneities of the sea ice pack and the ocean mixed layer affect the coupled evolution of both media. Chapter 2 demonstrates how lateral variability in mixed layer properties feeds back into ice growth during the autumn freeze up. Chapter 3 and Chapter 4 examine how sea ice variability impacts inertial oscillation development and internal wave generation.

In Chapter 2, we used observations from autonomous vehicles, remote sensing, and a mixed layer model to show how advected sea ice meltwater cooled and restratified the mixed layer, causing earlier freeze up than in adjacent waters. By demonstrating how melt-related temperature and stratification anomalies precondition freeze up in predictable ways, our results can improve freeze up forecasting.

Chapter 3 used moored velocity observations, remote sensing, and an idealized ice-ocean slab model to demonstrate how sea ice lead opening permitted inertial oscillation development in winter despite persistently high ice concentrations, whereas an unfractured ice pack selectively filtered out near-inertial motions. Our results indicate that wintertime near-inertial motion predictions should account for the lateral scales of ice fracturing and cannot rely on free-drift proxies like ice concentration.

Chapter 4 investigated ways in which sea ice affected the fate of energy contained in mixed layer inertial oscillations, including near-inertial internal wave generation. Moored observations, drifting buoys, and ice floe tracking in satellite imagery were used to quantify the spatial coherence scales of inertial oscillations in the marginal ice zone. Our results support the hypothesis that sea ice properties can promote spatially divergent inertial oscillations, resulting in internal wave generation.

This research demonstrated reciprocal impacts between spatial variability in the sea ice and the ocean. In addition to the process-level conclusions described above, this dissertation also contributed methods for integrating data from distributed observational platforms, remote sensing, and simple models to generate system-level understanding of the coupled evolution of the atmosphere-ice-ocean system.

Table of Contents

Figures

Acknowledgements

I acknowledge with gratitude the Coast Salish and Dena'ina peoples, on whose lands I have lived and worked while completing this dissertation. I have additionally passed through the lands and waters of the Unangax̂ and Iñupiat peoples while conducting field work for this research. I am deeply thankful for their stewardship of these lands over many generations, stewardship which continues to this day.

This work was funded by the Office of Naval Research through the Stratified Ocean Dynamics of the Arctic experiment as well as by the National Science Foundation through a Graduate Research Fellowship. This research was made possible by the exemplary engineering and operational support work of Jason Gobat, Eric Boget, and Ben Jokinen of the University of Washington Applied Physics Laboratory. In addition, I thank the captains and crews of USCGC *Healy* for their hard work and professionalism during the 2018 and 2019 SODA research cruises.

I offer my deepest gratitude to my advisors, Craig Lee and Luc Rainville, whose guidance and support have been the foundation of this dissertation. Thank you for fostering my scientific intuition, valuing my work, and generously bringing me into our scientific community. Your kindness, humility, and commitment to excellence have set a standard that I will strive to emulate throughout my career.

Thank you to my collaborators and especially my committee, Jodi Young, Jennifer Hutchings, Cecilia Bitz, and Mark Warner, for years of discussions that yielded renewed motivation and newfound perspective. I am particularly grateful that I

met Jenny during a summer school on Svalbard, where her lessons on sea ice mechanics allowed me to approach physical oceanography with new eyes. It has been very exciting to work at the nexus of our respective disciplines. Jenny's mentorship and feedback has gone far beyond what I expected of a committee member.

I would never have started my doctoral journey without the mentors who encouraged me to follow this path. Thank you to Chris Backstrum, Richard Nevle, and Arild Sundfjord, who, at various critical moments, ensured that I believed in myself enough to imagine myself as a scientist.

I am incredibly grateful for the community of friends, scientific and otherwise, that have supported me over the years. My first-year physical oceanography cohort, Erin Broatch and Jade Sauvé, were essential to my survival of the first year of graduate school. Thank you for endless patience and good cheer through many, many pages of GFD equations. Sam Brenner has been the best lab-mate, friend, and collaborator I could ever hope to find. I still haven't found the right words to thank Aurora Roth the friendship, kindness, and love that she has shown me over the years. It goes without saying that I could not have done this without her. Thank you also to the many, many other friends with whom I have lived, shared meals, and found joy over the years. You always remind me of what matters most in life.

I owe so much to the support of my family. I know I have asked a lot of you in these past years. Thank you to my parents, Paul and Barb, who have never questioned my path, even when my choices probably haven't seemed to make me particularly happy. Thank you for taking the long view, for trusting me to know myself, and for

trusting me to know what's important and worthwhile even when it might not make that much sense. Thank you to my sister Abbie, who has always fiercely believed in the value of science and fought to make sure I would keep believing that my work counts for something. Thank you to my brother Nick, who has been one of my best friends and always had a deep sense of curiosity about what I do.

Chapter 1 Introduction

This dissertation studies physical processes mediating Arctic Ocean air-sea heat and momentum exchanges on temporal scales of days to weeks and spatial scales of 10-100 km. The approach combines in situ observations collected by moored and autonomous instruments during the Office of Naval Research Stratified Ocean Dynamics Experiment (SODA; Lee et al., 2016), satellite observations, and idealized mixed layer models. A key theme that emerges from this work is the importance of horizontal structure in the sea ice and ocean to physical processes in both media. This theme is manifest in the timing of ice freeze up (Chapter 2), the development of inertial oscillations in the ice and mixed layer (Chapter 3), and the generation of near-inertial internal waves (Chapter 4).

In polar regions, the atmosphere, ice, and ocean are connected through thermodynamic processes that regulate heat and energy exchange among these layers. During summer, solar radiation contributes to the melting of sea ice, exposing open water to the atmosphere. In winter, upward heat fluxes to the atmosphere cool the ocean mixed layer, allowing ice to form and thicken. As winter progresses, ice growth is limited by the insulating effects of increasing ice thickness and accumulated snow.

Ice retreat in the spring and ice growth in the autumn are spatially heterogeneous. Colder sea surface temperatures can persist in areas that experienced later ice retreat, preconditioning earlier freeze up in autumn (Blanchard-Wrigglesworth et al., 2011; Day et al., 2014). Sea surface salinity and near surface stratification can

also vary in space according to the history of ice melt. **Chapter 2 examines processes that create spatial variability in the timing of freeze up**, finding that 1) colder sea surface temperatures caused by late ice retreat advect with the surface circulation, promoting earlier freeze up in neighboring areas, and 2) late ice melt can create persistent, anomalously shallow mixed layer depths that also promote early freeze up.

In addition to heat exchanges, sea ice mediates air-sea momentum transfer. The wind pushes on the topside of the ice, and the accelerating ice imposes stresses on the ocean surface. In a consolidated ice pack, momentum can be diverted to collisions between ice floes, limiting the wind's ability to accelerate the underlying ocean. As ice thins and weakens in response to climate change, the importance of these internal ice stresses may decline, resulting in more direct coupling between the atmosphere and ocean (Brenner et al., 2023; Martin et al., 2014).

Atmospheric storms blowing over the ocean excite inertial oscillations in the mixed layer. A transient adjustment to the change in surface forcing, inertial oscillations are characterized by mixed layer velocities that resonantly oscillate at the Coriolis frequency. When viewed on a map, the trajectories of tracked floats undergoing inertial oscillations look like anticyclonic loops superimposed on the low frequency background flow.

Inertial oscillations link energy input by the wind to ocean mixing. Inertial oscillations can cause shear-driven mixing at the base of the mixed layer, entraining the top of the pycnocline. Diverging mixed layer oscillations can also radiate energy into the stratified ocean interior as near-inertial internal waves. When these internal waves

ultimately break, the resulting turbulence can vertically transport important quantities like heat, nutrients, and carbon.

It has been hypothesized that Arctic sea ice loss could increase near-inertial internal wave-driven mixing, creating a positive wind-ice-ocean feedback loop (e.g., Fine and Cole, 2022). This process would consist of several steps. First, sea ice loss increases the energy contained in mixed layer inertial oscillations. Next, near-inertial energy is transferred to the pycnocline as propagating internal waves. Internal wave breaking then increases diapycnal mixing, bringing heat from warm, subsurface layers toward the ocean surface. Finally, upward heat fluxes melt ice, increasing near-inertial energy input and furthering the feedback loop.

Several decades of study have investigated the various steps of this feedback loop. These studies have found that the scale of inertial oscillations has increased as ice has weakened (Gimbert et al., 2012), pycnocline near-inertial energy has increased with decreasing sea ice concentration (Fine and Cole, 2022), and summertime vertical heat fluxes have increased by an order of magnitude in some parts of the Arctic (Dosser et al., 2021). Yet some details of this near-inertial energy pathway remain poorly understood in the presence of sea ice.

Observations indicate that the Arctic near-inertial internal wave response to atmospheric storms depends on ice strength and mobility and that some – but not all – storms in ice-covered conditions generate energetic near-inertial internal waves (Halle and Pinkel, 2003; Martini et al., 2014). Chapter 3 and Chapter 4 investigate the role of sea ice characteristics in determining the ocean near-inertial response to storms.

Chapter 3 examines how sea ice modifies near-inertial energy input to the mixed layer, finding that fractured ice allowed inertial oscillations to develop in a dense, midwinter ice pack. **Chapter 4 examines how sea ice affects the fate of near-inertial energy in the mixed layer**, finding that sea ice may promote internal wave generation by reducing the horizontal coherence scales of inertial oscillations.

1 The Changing Beaufort Gyre

This dissertation focuses on air-ice-ocean dynamics in the Beaufort Gyre, the dominant circulation system of the Western Arctic's Canada Basin. The Beaufort Gyre's anticyclonic (clockwise) geostrophic sea ice and upper ocean circulation is driven by elevated dynamic ocean topography (Armitage et al., 2017), caused in turn the dominant winds of the atmospheric Beaufort High (Serreze and Barry 2014). Gyre spin-up is balanced by Ekman pumping arising from friction in the ice-ocean boundary layer (Meneghello et al., 2018; Dewey et al., 2018), and eddy fluxes generated by baroclinic instability (Manucharyan and Spall, 2016; Meneghello et al., 2020). The Beaufort Gyre is a major reservoir for heat and freshwater in the Arctic (Aagaard and Carmack, 1989; McLaughlin et al., 2011; Timmermans et al., 2018), and its coupled ice-ocean system is undergoing rapid transformation in response to climate change. These changes include sea ice loss (Stroeve and Notz, 2018), warming (Timmermans et al., 2018), and increasing freshwater storage (Proshutinsky et al., 2009; Proshutinsky et al., 2020).

Sea ice plays a central role in setting ocean properties and dynamics in the Beaufort Gyre. The areal extent of sea ice has declined over the satellite record in the

Beaufort Gyre region, with September sea ice extent declining by nearly 70% from 1979 to 2018 (Stroeve and Notz, 2018). Earlier ice retreat and later ice advance, along with increasingly large seasonally ice-free areas, have led to an expansion of the marginal and seasonal ice zones (Onarheim et al., 2018; Strong and Rigor, 2013; Thomson et al., 2016). In addition, sea ice is now thinner (Rothrock et al., 2008; Kwok, 2018), drifting faster (Hakkinen et al., 2008; Kwok et al., 2013; Spreen et al., 2011), and deforming more readily (Rampal et al., 2009). The most substantial ice loss (in extent and thickness) in the Arctic has occurred in the Beaufort Gyre region (Liu et al., 2021; Timmermans and Toole, 2023). These changes in sea ice strength and morphology are altering atmosphere-ocean momentum transfer. Historically, thick multiyear ice limited the impact of surface winds on the underlying ocean, but the atmosphere and ocean are becoming increasingly coupled as the ice becomes more mobile (Brenner et al., 2023; Martin et al., 2014).

Within the annual cycle, brine rejection during sea ice growth in autumn and winter (October-May) produces salty water that deepens the ocean mixed layer. Ice melt from June-September restratifies the upper ocean, shoaling the mixed layer. Sea ice melt exposes the low-albedo ocean surface to solar radiation, increasing energy absorption. Subsequent surface warming fuels further ice melt in a process known as ice-albedo feedback (Perovich et al., 2007; Perovich and Richter-Menge, 2009). As the Arctic is primarily salinity stratified, warm layers exist at depth. These warm layers include a near-surface temperature maximum formed seasonally due to summer solar radiation (Jackson et al., 2010; Steele et al., 2011), as well as deeper, long-lasting warm

layers associated with boundary-sourced watermasses originating in the Pacific and Atlantic (Timmermans and Toole, 2023). Warming on the inflow shelf seas has increased subsurface temperatures in the Beaufort Gyre (Timmermans et al., 2018).

2 Near-inertial internal waves

Internal gravity waves are an essential component of ocean dynamics, influencing energy propagation, vertical mixing, and the structure of the ocean's stratified interior. These waves, which are oscillatory perturbations that transport energy horizontally and vertically, are generated by winds, and tidal and geostrophic flow over topography (D'Asaro 1985; Garrett and Kunze, 2007; Nikurashin and Ferrari, 2011).

Assuming the vertical velocity *w* can be described as a plane wave

$$w = Ae^{i(kx+ly+mz-\sigma t)} \quad 1.1$$

with amplitude *A,* horizontal wavenumbers *k* and *l*, vertical wavenumber *m*, and frequency σ, internal wave propagation is governed by the dispersion relation

$$\frac{m^2}{k^2+l^2} = \frac{N^2-\sigma^2}{\sigma^2-f^2}. \quad 1.2$$

Here *f* is the local Coriolis frequency $f = 2\Omega\, sin(\phi)$, where Ω is the Earth's angular velocity and ϕ is the latitude. The buoyancy frequency $N^2 = -\frac{g}{\rho_o}\frac{\partial \rho}{\partial z}$ is imposed by the local stratification.

For internal waves to propagate, *k, l,* and *m* must be positive. Thus, from the dispersion relation, internal waves are restricted to frequencies between *f* (the low

frequency limit) and N (the high frequency limit). Changes in stratification refract internal waves, altering their amplitude and vertical wavenumber m. This refraction increases energy in regions of stronger stratification, an effect that can be accounted for by the WKB approximation.

An internal wave's phase velocity is perpendicular to its group velocity, with energy propagating with the group velocity. Thus, upward phase propagation indicates downward energy propagation. The angle at which waves propagate is given by the aspect ratio of vertical to horizontal wavenumbers found on the left hand side of the dispersion relationship (Equation 1.2). For given Coriolis and buoyancy frequencies, the angle of the wavenumber vector is determined by the wave frequency. Purely inertial-frequency oscillations do not propagate and experience purely horizontal velocities. Orbits tilt for waves of increasing frequency, with gravity becoming increasingly important as a restoring force.

Waves with frequencies near the naturally resonant Coriolis frequency are called near-inertial internal waves. These waves are typically generated at the surface by storms (Gill, 1984; D'Asaro, 1989), and thus are much more intermittent than internal tides (Alford et al., 2016). Near-inertial internal waves have orbital motions that are nearly horizontal and are affected by the Earth's rotation. These waves generally must propagate equatorward (in the direction of decreasing f) so that their frequency remains above the local Coriolis frequency. They rotate clockwise in the northern hemisphere and typically have horizontal scales of 10-100 km (Alford et al., 2016).

The amount of work done by the wind on near-inertial motions in the mixed layer is not precisely known, due in part to differences among reanalysis wind products, but is thought to be in the range of 0.3-1.4 TW (Alford, 2003; Rimac et al., 2013; Watanabe and Hibiya, 2003; Whalen et al., 2020). Globally, this wind work is greatest along midlatitude storm tracks and peaks in winter (Alford and Whitmont, 2007). The amount of this wind work that escapes the mixed layer and enters the ocean interior as propagating internal waves may be as high as 50%, but this number is poorly constrained (Furuichi et al., 2008; Whalen et al., 2020; Zhai et al., 2009). Strong velocity shear associated with near-inertial internal waves can yield critical Richardson numbers $Ri = {N^2}/{\left(\frac{\partial \boldsymbol{U}}{\partial z}\right)^2} < 0.25$, with the resulting instabilities producing vertical mixing and dissipation. Breaking internal waves transfer buoyant water downwards, counteracting the Meridional Overturning Circulation and maintaining the abyssal stratification (Kunze, 2017; Munk and Wunsch; Wunsch and Ferrari, 2004).

3 Sea ice dynamics

Sea ice responds to stresses imposed by the wind and ocean currents at the air-ice and ice-ocean interfaces. Its motion is further modified by mechanical forces within the ice pack and the Coriolis force. The sea ice momentum equation can be written (following Weiss, 2013):

$$\rho_i d \left(\frac{\partial \boldsymbol{U}_i}{\partial t} + \boldsymbol{U}_i \cdot \nabla \boldsymbol{U}_i + f\boldsymbol{k} \times \boldsymbol{U}_i \right) = \tau_{ai} + \tau_{io} + \nabla \cdot \sigma \qquad 1.3$$

where ρ_i is the ice density, d is the ice thickness, $\boldsymbol{U}_i$ is the horizontal ice velocity, τ_{ai} is the air-ice stress, τ_{io} is the ice-ocean stress, and σ is the layer-integrated internal ice

stress. This formulation neglects forces out of the sea surface plane, such as gravitational acceleration arising from sea surface tilt. Alternatively, the sea surface tilt can be combined with the Coriolis acceleration using geostrophic balance, which would give rise to a dependence on the ocean geostrophic velocity (Leppäranta, 2011).

Typically, the dominant terms in the sea ice momentum equation at daily timescales are the air-ice stress τ_{ai}, ice-ocean stress τ_{io}, and internal ice stress divergence $\nabla \cdot \sigma$, with minor contributions from the Coriolis term and negligible contributions from the remaining terms (Hyatt, 2006; Steele et al., 1997). Thus, the sea ice momentum balance can be reduced to:

$$\tau_{ai} \approx \tau_{io} + \nabla \cdot \sigma \, . \qquad 1.4$$

Sea ice is said to be in *free drift* if the internal stress divergence term is negligible; ice concentrations below 0.85 and wind factor values above 2% are approximate thresholds beyond which internal stresses can be neglected. During periods of free drift, it follows from Equation 1.4 that momentum from the atmosphere is transferred directly through the ice to the ocean (i.e., $\tau_{ai} \approx \tau_{io}$).

Below the free-drift limit, the ice-ice interactions that comprise the internal stress divergence term reduce the total momentum transfer through the ice to the ocean. This is because the air-ice stress is primarily determined by wind speed and is therefore independent of ice dynamics, so increasing the internal stress divergence decreases the ice-ocean stress for a given wind forcing. Consolidated ice can transfer internal stresses hundreds of kilometers through the ice pack (Richter-Menge et al., 2002), so the local internal stress divergence term may be impacted by nonlocal ice dynamics.

4 References

Aagaard, K., and Carmack, E. C. (1989). The role of sea ice and other fresh water in the Arctic circulation. *Journal of Geophysical Research*, 94 (C10), 14485–14498. doi:10.1029/JC094iC10p14485

Alford, M. H. (2003). Improved global maps and 54-year history of wind-work on ocean inertial motions. *Geophysical Research Letters*, 30, 1424. doi:10.1029/2002GL016614

Alford, M. H., and Whitmont, M. (2007). Seasonal and spatial variability of near-inertial kinetic energy from historical moored velocity records. *Journal of Physical Oceanography*, 37, 2022–2037. doi:10.1175/JPO3106.1

Alford, M. H., MacKinnon, J. A., Simmons, H. L., and Nash, J. D. (2016). Near-inertial internal gravity waves in the ocean. *Annual Review of Marine Science*, 8, 95–123. doi:10.1146/annurev-marine-010814-015746

Armitage, T. W. K., Bacon, S., Ridout, A. L., Petty, A. A., Wolbach, S., and Tsamados, M. (2017). Arctic Ocean surface geostrophic circulation 2003–2014. *The Cryosphere*, 11, 1767–1780. doi:10.5194/tc-11-1767-2017

Blanchard-Wrigglesworth, E., Armour K. C., Bitz C. M., and DeWeaver, E. (2011). Persistence and inherent predictability of Arctic sea ice in a GCM ensemble and observations. *Journal of Climate*, 24(1), 231–250. doi:10.1175/2010JCLI3775.1

Brenner, S., Thomson, J., Rainville, L., Crews, L., and Lee, C. M. (2023). Wind-driven motions of the ocean surface mixed layer in the western Arctic. *Journal of Physical Oceanography*, 53(7), 1787–1804. doi:10.1175/JPO-D-22-0112.1

D'Asaro, E. A. (1985). The energy flux from the wind to near-inertial motions in the surface mixed layer. *Journal of Physical Oceanography*, 15 (8), 1043–1059. doi:10.1175/1520-0485(1985)015<1043:TEFFTW>2.0.CO;2

D'Asaro, E. A. (1989). The decay of wind-forced mixed layer inertial oscillations due to the β effect. *Journal of Geophysical Research*, 94 (C2), 2045–2056. doi:10.1029/JC094iC02p02045

Day, J. J., Tietsche, S., and Hawkins, E. (2014). Pan-Arctic and regional sea ice prediction: Initialisation month dependence. *Journal of Climate*, 27, 4371–4390. doi:10.1175/JCLI-D-13-00614.1

Dewey, S., Morison, J., Kwok, R., Dickinson, S., Morison, D., and Andersen, R. (2018). Arctic ice-ocean coupling and gyre equilibration observed with remote

sensing. *Geophysical Research Letters*, 45, 1499–1508. doi:10.1002/2017GL076229

Dosser, H. V., M. Chanona, S. Waterman, N. C. Shibley, and M.-L. Timmermans, 2021: Changes in internal wave-driven mixing across the Arctic Ocean: Finescale estimates from an 18-year pan-arctic record. *Geophysical Research Letters*, 48 (8), e2020GL091 747, doi:10.1029/2020GL091747.

Fine, E. C., and Cole, S. T. (2022). Decadal observations of internal wave energy, shear, and mixing in the western Arctic Ocean. *Journal of Geophysical Research: Oceans*, 127 (5). doi:10.1029/2021JC018056

Furuichi, N., Hibiya, T., and Niwa, Y. (2008). Model-predicted distribution of wind-induced internal wave energy in the world's oceans. *Journal of Geophysical Research*, 113, C09034. doi:10.1029/2008JC004768

Garrett, C., and Kunze, E. (2007). Internal tide generation in the deep ocean. *Annual Review of Fluid Mechanics*, 39, 57–87. doi:10.1146/annurev.fluid.39.050905.110227

Gill, A. E. (1984). On the behavior of internal waves in the wakes of storms. *Journal of Physical Oceanography*, 14(7), 1129–1151. doi:10.1175/1520-0485(1984)014⟨1129:OTBOIW⟩2.0.CO;2

Gimbert, F., Jourdain, N. C., Marsan, D., Weiss, J., and Barnier, B. (2012). Recent mechanical weakening of the Arctic sea ice cover as revealed from larger inertial oscillations. *Journal of Geophysical Research: Oceans*, *117*(C11). doi:10.1029/2011JC007633

Hakkinen, S., Proshutinsky, A., and Ashik, I. (2008). Sea ice drift in the Arctic since the 1950s. *Geophysical Research Letters*, 35 (19). doi:10.1029/2008GL034791

Halle, C., and R. Pinkel (2003). Internal wave variability in the Beaufort Sea during the winter of 1993/1994, *Journal of Geophysical Research: Oceans*, 108(C7), doi:10.1029/2000JC000703

Hyatt, J. (2006). Wind, sea ice, inertial oscillations and upper ocean mixing in Marguerite Bay, Western Antarctic Peninsula: Observations and modeling (Ph.D. thesis). Massachusetts Institute of Technology Woods Hole Oceanographic Institution Joint Program.

Jackson, J. M., Carmack, E. C., McLaughlin, F. A., Allen, S. E., and Ingram, R. G. (2010). Identification, characterization, and change of the near-surface temperature maximum in the Canada Basin, 1993–2008. *Journal of Geophysical Research*, 115, C05021. doi:10.1029/2009JC005265

Kwok, R. (2018). Arctic sea ice thickness, volume, and multiyear ice coverage: Losses and coupled variability (1958–2018). *Environmental Research Letters*, 13 (10), 105005. doi:10.1088/1748-9326/aae3ec

Kwok, R., Spreen, G., and Pang, S. (2013). Arctic sea ice circulation and drift speed: Decadal trends and ocean currents. *Journal of Geophysical Research: Oceans*, 118 (5), 2408–2425. doi:10.1002/jgrc.20191

Kunze, E. (2017). Internal-wave-driven mixing: Global geography and budgets. *Journal of Physical Oceanography*, 47, 1325–1345. doi: 10.1175/JPO-D-16-0141.1

Lee, C. M., et al. (2016). *Stratified Ocean Dynamics of the Arctic: Science and Experiment Plan* (Technical Report APL-UW-1601). Applied Physics Laboratory, University of Washington, Seattle, WA.

Leppäranta, M. (2011). *The drift of sea ice*. Springer Praxis Books, Springer, Berlin, Heidelberg. doi:10.1007/978-3-642-04683-4

Liu, Z., Risi, C., Codron, F., and others. (2021). Acceleration of western Arctic sea ice loss linked to the Pacific North American pattern. *Nature Communications*, 12, 1519. doi:10.1038/s41467-021-21830-1

Manucharyan, G. E., and Spall, M. A. (2016). Wind-driven freshwater buildup and release in the Beaufort Gyre constrained by mesoscale eddies. *Geophysical Research Letters*, 43, 273–282. doi:10.1002/2015GL065957

Manucharyan, G. E., Spall, M. A., and Thompson, A. F. (2016). A theory of the wind-driven Beaufort Gyre variability. *Journal of Physical Oceanography*, 46 (11), 3263–3278. doi:10.1175/JPO-D-16-0091.1

Martin, T., Steele, M., and Zhang, J. (2014). Seasonality and long-term trend of Arctic Ocean surface stress in a model. *Journal of Geophysical Research: Oceans, 119*, 1723–1738. doi:10.1002/2013JC009425

Martini, K. I., Simmons, H. L., Stoudt, C. A., and Hutchings, J. K. (2014). Near-inertial internal waves and sea ice in the Beaufort Sea. *Journal of Physical Oceanography, 44*(8), 2212–2234. doi:10.1175/JPO-D-13-0160.1

McLaughlin, F., Carmack, E., Proshutinsky, A., Krishfield, R. A., Guay, C., Yamamoto-Kawai, M., Jackson, J. M., and Williams, B. (2011). The rapid response of the Canada Basin to climate forcing: From bellwether to alarm bells. *Oceanography*, 24 (3), 146–159. doi:10.5670/oceanog.2011.66

Meneghello, G., Marshall, J. C., Campin, J.-M., Doddridge, E., and Timmermans, M.-

L. (2018). The ice-ocean governor: Ice-ocean stress feedback limits Beaufort Gyre spin-up. *Geophysical Research Letters*, 45, 11293–11299. doi:10.1029/2018GL080171

Meneghello, G., Doddridge, E., Marshall, J., Scott, J., and Campin, J. (2020). Exploring the role of the "ice–ocean governor" and mesoscale eddies in the equilibration of the Beaufort Gyre: Lessons from observations. *Journal of Physical Oceanography*, 50, 269–277. doi:10.1175/JPO-D-18-0223.1

Munk, W., and Wunsch, C. (1998). Abyssal recipes II: Energetics of tidal and wind mixing. *Deep Sea Research Part I: Oceanographic Research Papers*, 45, 1977–2010. doi:10.1016/S0967-0637(98)00070-3

Nikurashin, M., and Ferrari, R. (2011). Global energy conversion rate from geostrophic flows into internal lee waves in the deep ocean. *Geophysical Research Letters*, 38, L08610. doi:10.1029/2011GL046576

Onarheim, I. H., Eldevik, T., Smedsrud, L. H., and Stroeve, J. C. (2018). Seasonal and regional manifestation of Arctic sea ice loss. *Journal of Climate*, 31 (12), 4917–4932. doi:10.1175/JCLI-D-17-0427.1

Perovich, D. K., Light, B., Eicken, H., Jones, K. F., Runciman, K., and Nghiem, S. V. (2007). Increasing solar heating of the Arctic Ocean and adjacent seas, 1979–2005: Attribution and role in the ice-albedo feedback. *Geophysical Research Letters*, 34, L19505. doi:10.1029/2007GL031480

Perovich, D. K., and Richter-Menge, J. A. (2009). Loss of sea ice in the Arctic. *Annual Review of Marine Science*, 1, 417–441. doi:10.1146/annurev.marine.010908.163805

Proshutinsky, A., Krishfield, R., and Timmermans, M.-L. (2020). Introduction to special collection on Arctic Ocean modeling and observational synthesis (FAMOS) 2: Beaufort Gyre phenomenon. *Journal of Geophysical Research: Oceans*, 125, e2019JC015400. doi:10.1029/2019JC015400

Proshutinsky, A., Krishfield, R., Timmermans, M.-L., Toole, J., Carmack, E., McLaughlin, F., Williams, W. J., Zimmermann, S., Itoh, M., and Shimada, K. (2009). Beaufort Gyre freshwater reservoir: State and variability from observations. *Journal of Geophysical Research*, 114, C00A10. doi:10.1029/2008JC005104

Rampal, P., Weiss, J., and Marsan, D. (2009). Positive trend in the mean speed and deformation rate of Arctic sea ice, 1979–2007. *Journal of Geophysical Research*, 114, C05013. doi:10.1029/2008JC005066

Richter-Menge, J. A., McNutt, S. L., Overland, J. E., and Kwok, R. (2002). Relating Arctic pack ice stress and deformation under winter conditions. *Journal of Geophysical Research: Oceans*, 107. doi:10.1029/2000JC000477

Rimac, A., von Storch, J.-S., Eden, C., and Haak, H. (2013). The influence of high-resolution wind stress field on the power input to near-inertial motions in the ocean. *Geophysical Research Letters*, 40, 4882–4886. doi:10.1002/grl.50929

Rothrock, D. A., Percival, D. B., and Wensnahan, M. (2008). The decline in Arctic sea-ice thickness: Separating the spatial, annual, and interannual variability in a quarter century of submarine data. *Journal of Geophysical Research*, 113, C05003. doi:10.1029/2007JC004252

Serreze, M. C., and Barry, R. G. (2005). *The Arctic climate system*. Cambridge: Cambridge University Press. doi:10.1017/CBO9780511535888

Spreen, G., Kwok, R., and Menemenlis, D. (2011). Trends in Arctic sea ice drift and role of wind forcing: 1992–2009. *Geophysical Research Letters*, 38, L19501. doi:10.1029/2011GL048970

Steele, M., Ermold, W., and Zhang, J. (2011). Modeling the formation and fate of the near-surface temperature maximum in the Canadian Basin of the Arctic Ocean. *Journal of Geophysical Research*, 116, C11015. doi:10.1029/2010JC006803

Steele, M., Zhang, J., Rothrock, D., and Stern, H. (1997). The force balance of sea ice in a numerical model of the Arctic Ocean. *Journal of Geophysical Research: Oceans*, 102 (C9), 21061–21079. doi:10.1029/97JC01454

Stroeve, J., and Notz, D. (2018). Changing state of Arctic sea ice across all seasons. *Environmental Research Letters*, 13 (10), 103001. doi:10.1088/1748-9326/aade56

Strong, C., and Rigor, I. G. (2013). Arctic marginal ice zone trending wider in summer and narrower in winter. *Geophysical Research Letters*, 40, 4864–4868. doi:10.1002/grl.50928

Thomson, J., Fan, Y., Stammerjohn, S., Stopa, J., Rogers, W. E., and Girard-Ardhuin, F., et al. (2016). Emerging trends in the sea state of the Beaufort and Chukchi seas. *Ocean Modelling*, 105, 1–12. doi:10.1016/j.ocemod.2016.02.009

Timmermans, M.-L., and Toole, J. M. (2023). The Arctic Ocean's Beaufort Gyre. *Annual Review of Marine Science*, 15, 223–248. doi:10.1146/annurev-marine-032122-012034

Timmermans, M.-L., Toole, J., and Krishfield, R. (2018). Warming of the interior

Arctic Ocean linked to sea ice losses at the basin margins. *Science Advances*, 4 (8), eaat6773. doi:10.1126/sciadv.aat6773

Watanabe, M., and Hibiya, T. (2002). Global estimates of the wind-induced energy flux to inertial motions in the surface mixed layer. *Geophysical Research Letters*, 29 (8). doi:10.1029/2001GL014422

Weiss, J. (2013). *Drift, deformation, and fracture of sea ice*. SpringerBriefs in Earth Sciences, Springer, Dordrecht. doi:10.1007/978-94-007-6202-2

Whalen, C. B., de Lavergne, C., Naveira Garabato, A. C., et al. (2020). Internal wave-driven mixing: Governing processes and consequences for climate. *Nature Reviews Earth and Environment*, 1, 606–621. doi:10.1038/s43017-020-0097-z

Wunsch, C., and Ferrari, R. (2004). Vertical mixing, energy, and the general circulation of the oceans. *Annual Review of Fluid Mechanics*, 36, 281–314.

Zhai, X., Greatbatch, R. J., Eden, C., and Hibiya, T. (2009). On the loss of wind-induced near-inertial energy to turbulent mixing in the upper ocean. *Journal of Physical Oceanography*, 39 (11), 3040–3045. doi:10.1175/2009JPO4259.1

Chapter 2 Direct Observations of the Role of Lateral Advection of Sea Ice Meltwater in the Onset of Autumn Freeze Up

Preface

Crews, L., Lee, C. M., Rainville, L., and Thomson, J. (2022). Direct observations of the role of lateral advection of sea ice meltwater in the onset of autumn freeze up. *Journal of Geophysical Research: Oceans*, 127, e2021JC017775. doi:10.1029/2021JC017775

Abstract

In seasonally ice-free parts of the Arctic Ocean, autumn is characterized by heat loss from the upper ocean to the atmosphere and the onset of freeze up, in which first year sea ice begins to grow in open water areas. The timing of freeze up can be highly spatially variable, complicating efforts to provide accurate sea ice forecasting for marine operations. While melt season anomalies can be used to predict freeze up anomalies in some parts of the Arctic, this one-dimensional view merits further examination in light of recent work demonstrating the importance of three-dimensional flows in setting mixed layer properties in marginal ice zones. In this study we show that horizontal advection of sea ice meltwater hastens freeze up in areas distant from the ice edge. We use nearly 800 temperature and salinity profiles along with satellite imagery collected in the central Beaufort Sea in autumn 2018 to document the roughly 100 km advection of a cold and fresh surface meltwater layer over several weeks. After the meltwater arrived, the mixed layer was cooler and shallower than the mixed layer in

adjacent areas unaffected by the meltwater. The cooler and shallower meltwater-influenced mixed layer promoted earlier ice formation. Within the meltwater-affected area, advection was nearly as important as heat loss to the atmosphere for seasonally integrated mixed layer heat loss.

1 Introduction

The autumn freeze up, during which sea ice begins to expand in seasonally ice-free seas, is preceded by an autumn cooling period in which heat fluxes from the ocean to the atmosphere cool the ocean mixed layer toward the freezing temperature, a prerequisite for ice formation. Once the mixed layer has cooled to the freezing temperature, additional heat loss to the atmosphere results in the growth of ice crystals floating on the ocean surface. How freeze up proceeds from this point depends on atmospheric conditions, the sea state, and the stratification below the mixed layer. In calm conditions, the frazil crystals freeze together into a thin sheet called nilas (Wadhams, 2000). When surface waves are present, the frazil crystals instead freeze into slushy pancakes which eventually coalesce into floes (Wadhams, 2000). Ice thickens if the upward heat flux through the ice exceeds the heat flux from the underlying ocean (Wadhams, 2000). However, mixed layer deepening caused by e.g., brine rejection or storms may liberate heat from the ocean pycnocline and slow or temporarily reverse the freeze up process (Smith et al., 2018).

The autumn ice advance date is occurring later throughout the Arctic Ocean (Stroeve et al., 2014; Thomson et al., 2016), with the most pronounced shifts in phenology found in the Chukchi and Beaufort Seas (Thomson et al., 2016). Later freeze

up is due to warmer sea surface temperatures, which are caused by increased solar absorption throughout the summer (Stroeve et al., 2014). A variety of definitions for freeze up have been used in the literature, and the timing of freeze up can depend on which definition is chosen (Johnson and Eicken, 2016). Thomson et al. (2016) defined the ice advance day as the first day that sea ice concentration derived from passive microwave satellites exceeded 15% for five days. Freeze up in the Beaufort Sea in autumn 2018, visualized using this metric, was patchy on smaller spatial scales (10-100 km; Figure 2.1) than those over which the atmospheric forcing is expected to vary (100-1000 km), pointing to the importance of ocean processes in generating freeze up timing variability on these smaller scales.

The timing of freeze up is important for several reasons. First, ice inhibits heat exchange between the ocean and atmosphere once it develops sufficient thickness (e.g., Maykut, 1978), so earlier or later ice formation would be expected to limit or extend the period in which meaningful heat exchange can occur. In addition, the timing of freeze up matters because the presence of ice alters the efficiency of atmosphere-ocean momentum transfer (e.g., Brenner et al., 2021) and air-sea gas exchange (Islam et al., 2017). Furthermore, the abundance of protists incorporated into sea ice decreases with later freeze up, which in turn decreases ice protist abundance at the beginning of the spring bloom (Niemi et al., 2011). Finally, accurate freeze up forecasting at operational timescales is essential for vessels to safely navigate these waters.

The mixed layer of the Beaufort Sea at the end of summer is shallow, fresh and stratified primarily due to ice melt, and warm due to solar heating (Jackson et al., 2010;

Toole et al., 2010). The continuous effect of cooling and freshening associated with summer ice melt competes with the solar heating, which can result in a temperature maximum below the mixed layer (near surface temperature maximum or "NSTM", Jackson et al., 2010; Steele et al., 2011). Beneath the NSTM is a temperature minimum marking the remainder of the previous winter's mixed layer (Jackson et al., 2010). Below this minimum are the warm Pacific Summer Water layer, the cold Pacific Winter Water layer, and the warm Atlantic Water layer, all of which were advected from Arctic Ocean boundaries. These boundary-derived layers do not typically influence the surface in the Beaufort Sea on seasonal timescales because of the strong near-surface stratification (Toole et al., 2010).

Studies of upper ocean processes in the Arctic often emphasize one-dimensional mixed layer evolution forced by momentum and buoyancy exchanges with the overlying sea ice or atmosphere (e.g., Dewey et al., 2017; Toole et al., 2010). However, mixed layer instabilities at submesoscale fronts have been shown to play a significant role in setting ocean mixed layer properties (e.g., Boccaletti et al., 2007; Thomas et al., 2008). In the Beaufort Sea, restratification under sea ice was not replicated by a one-dimensional model (Toole et al., 2010), and Timmermans et al. (2012) argue that this restratification was likely caused by submesoscale processes on the basis of frontal structure observations and order 1 balanced Richardson number estimates.

Subsequent observations and modeling studies have shown that submesoscale fronts are found in marginal ice zones (MIZs) where surface freshening due to ice melt causes strong horizontal surface buoyancy gradients over length scales of 1–10 km

(e.g., Brenner et al., 2020; Horvat et al., 2016; Lu et al., 2015; Manucharyan and Thompson, 2017). Fronts in the Arctic are also found at the confluence of different watermasses, for example in Fram Strait (von Appen et al., 2018), or river plumes (Alkire et al., 2019; Macdonald et al., 1995). Observations demonstrate an active submesoscale field in the Beaufort Sea (Mensa et al., 2018), in the neighboring Chukchi Sea (Timmermans and Windsor, 2013), as well as in Fram Strait (von Appen et al., 2018).

Basin-scale observations in the Beaufort Sea indicate that month-to-month changes in mixed layer temperature and salinity are largely due to one-dimensional processes (Dewey et al., 2017). Here we expand on this regionally one-dimensional view using mesoscale-resolving observations of ocean temperature and salinity in the weeks preceding freeze up. We find that the horizontal advection of a shallow meltwater front cooled and restratified the mixed layer. These lateral effects allowed freeze up to occur earlier in the meltwater than in adjacent waters, highlighting an important consequence of mixed layer heterogeneity and three-dimensional processes.

This Chapter is organized as follows. Chapter 2.2 outlines the ocean observations and remote sensing products used in this study and quantifies differences between in situ and remote sensing observations. Chapter 2.3 describes the meltwater and its advection. Chapter 2.4 develops a mixed layer heat budget to quantify the importance of meltwater advection to mixed layer heat loss. Chapter 2.5 describes an additional instance of freshwater advection and its effect on freeze up. Chapter 2.6 summarizes and discusses the results.

2 Methods

2.1 Overview

This study uses observations collected in the Beaufort Sea in September to October 2018, as part of the Stratified Ocean Dynamics of the Arctic (SODA) experiment, to investigate mechanisms that drive freeze up heterogeneity. The SODA experiment, sponsored by the U.S. Office of Naval Research, aims at understanding stratification changes in the Arctic Ocean and includes many other components (Lee et al., 2016; Rainville et al., 2020). The upper ocean's evolution was documented by mesoscale-resolving upper ocean temperature and salinity profiles from four autonomous Seagliders. The persistent Seaglider sampling was supplemented by episodic sampling from four Wave Gliders and a ship-based profiler (Underway CTD). The locations of these measurements are shown in Figure 2.2. Conservative temperature and absolute salinity were calculated using the Gibbs SeaWater (GSW) Oceanographic Toolbox Version 3.0.11. All data collected as part of the field campaign (i.e., not by satellites) and discussed in this paper are reported as conservative temperature and absolute salinity unless otherwise noted. Potential density was calculated for a reference sea pressure of 0 dbar. Additional context was provided by remote sensing products and a one-dimensional mixed layer model.

2.2 Upper ocean temperature and salinity observations

2.2.1 Seagliders

Seaglider autonomous vehicles sampled ocean temperature and salinity between

the surface and 1000 m. The Seagliders employed a saw-tooth dive pattern with approximately 5 km horizontal spacing between profiles at the surface. Temperature and salinity data were averaged into 1-m depth bins and profiles lacking data above 15 m were not used. If the remaining temperature or salinity profiles did not extend to the surface, the shallowest measured temperature or salinity was extrapolated as a constant value to the surface because we assume that these depths were well mixed.

Five Seagliders were deployed in open water on 21 September 2018; two of these were recovered after a few days due to technical issues. The three remaining Seagliders sampled two quasi-parallel lines spanning roughly 145.3°W to 147.4°W, 73.6°N to 74.9°N (Figure 2.2). Each line was sampled by Seagliders operating in tandem, with one or two Seagliders traversing half a line. This sampling strategy provided complete occupation of the line at a timescale of a few days. Data used in this study span 21 September to 15 October, with the end of the study period characterized by active freeze up (Figure 2.1). Two Seagliders continued sampling intermittently after freeze up and were lost in the ice while trying to overwinter, returning data from as late as February 2019. During the study period, one of the Seagliders made a one-time excursion north of the sampling line to assess conditions near the MIZ. Sampling by an additional Seaglider away from the main Seaglider line occurred on 26 September.

2.2.2 Wave Gliders

Four Liquid Robotics SV-2 Wave Gliders sampled near 73°N 147°W from 19-23 September as part of the SODA Alaska North Slope process study (MacKinnon et al., 2021). The Wave Gliders sampled temperature, conductivity, and pressure using

Sea-Bird “Glider Payload” CTDs. The low autumn sun angle at this latitude limited solar recharging so sampling was performed at 30-minute intervals to increase vehicle endurance, resulting in approximately 1-km horizontal sampling resolution. The nominal measurement depths varied by vehicle; the most common configuration was temperature sampling at 0.2 m and 9 m as well as conductivity sampling at 9 m. One vehicle also measured conductivity at 0.2 m, using an Aanderraa 4319B sensor. The exact depth varied slightly for each measurement as the vehicle moved.

2.2.3 Ship-based measurements

Temperature and salinity profiles were collected by an underway CTD (uCTD) at approximately 1 km horizontal spacing on 13 October. The uCTD recovery line was routed through the extended arm of USCGC *Healy*’s starboard crane to minimize sampling in the ship’s wake. The uCTD was deployed in “tow-yo mode”, meaning it was not recovered between casts, and data above 1 m were excluded to eliminate errors associated with identifying the start of the cast. Data from the down cast were used and sampling depths were determined by the probe’s freefall time and the ship’s speed; casts were typically to 130–160 m with maximum cast depths of about 180 m.

Near-surface ocean temperature and salinity were also collected by *Healy* while underway. The seawater intake was 2.7 m below the ship’s waterline. Underway salinity data are known to drift over time due to biofouling of the conductivity cell (Alory et al., 2015) and temperature data are biased because seawater warms while traveling through the ship system before its temperature is measured (Alory et al., 2015). To correct the underway data, we computed the difference between uCTD

conservative temperature and absolute salinity profiles averaged in the upper five meters and concurrent underway data. The underway data used in the comparison was the median value in one-hour windows centered on the times of the uCTD profiles. To correct underway absolute salinity, a linear fit of the differences between the uCTD absolute salinity and co-located underway absolute salinity was used to compute a continuous correction time series that was added to the underway absolute salinity (Alory et al., 2015). To correct underway conservative temperature, the median difference between the uCTD conservative temperature and co-located underway conservative temperature (−1.3°C) was added to the underway conservative temperature.

2.3 Mixing layer and mixed layer definitions

Using data collected from Ice-Tethered Profilers, Timmermans et al. (2012) distinguished between the Beaufort Sea surface layer, defined as a density change of 0.25 kg m^{-3} relative to the shallowest measurement, and the actively mixing layer, defined as a density change of 0.01 kg m^{-3} relative to the shallowest measurement. They found that mixing layers were common and attributed them to lateral restratification. Inspection of the density profiles in this study showed that mixing layers were common in open water as well, so we defined the mixing layer using a density change of 0.01 kg m^{-3} and the mixed layer using a density change of 0.25 kg m^{-3} (a scheme also used in Cole et al., 2014). We note that using a density difference criterion to define the mixing layer will not necessarily indicate active turbulence and may bias results by including mixing that has already occurred.

2.4 Ocean heat content

Ocean heat loss in an Eulerian framework was quantified by calculating the change with time in ocean heat content. The ocean heat content was calculated from each conservative temperature profile as

$$HC = \int_h^0 c_p \rho \, (T(z) - T_{fr}(z)) \, dz \qquad 2.1$$

where ρ is the measured potential density, c_p is the heat capacity, and T_{fr} is the freezing temperature calculated from the observed absolute salinity and pressure. Chapter 2.2.2.1 stated that missing surface data in the measured temperature profile *T(z)* were filled with a constant value, but this interpolation is not expected to impact the results related to ocean heat content as it only affected two profiles used in the heat content analysis (Chapter 2.4; the shallowest available measurements were at 2 m and 3 m). Heat was integrated using the trapezoidal method from the surface to the depth *h.* In this paper we will discuss the mixed layer heat content, for which *h* is the depth at which density increased by 0.25 kg m^{-3} relative to the surface, as well as the upper ocean heat content including the mixed layer and top of the pycnocline for which *h* is a specified constant depth.

2.5 Remote sensing and reanalysis

MODIS-Terra Nighttime sea surface temperature (SST) 8-day composite images were used to supplement in situ ocean temperature observations. Only data with quality flag values of 0 or 1 were used.

Dynamic ocean topography (DOT) collected by CryoSat-2 from early

September to early October was used to calculate surface geostrophic velocity (Scharroo et al., 2013).

Daily sea-ice concentrations from AMSR2 (a passive microwave instrument) were used to map sea ice extent and assess the timing of freeze up (Spreen et al., 2008). Synthetic Aperture Radar (SAR) satellite imagery provided occasional high resolution (~50 m) representation of the ice conditions. Backscatter characteristics can be used to clearly distinguish open water, sea ice floes, sea ice ridges, leads, and ice type with a much higher level of detail than passive microwave sea ice products (e.g., Kwok et al., 1999).

In situ salinity observations were compared to the weekly SMOS ARCTIC sea surface salinity product (Supply et al., 2020a, 2020b) which attempts to correct for biases caused by cold water (Köhler et al., 2015) and the presence of sea ice (Tang et al., 2018).

To force the mixed layer model (Chapter 2.2.7), hourly mean net longwave, net shortwave, sensible, and latent heat fluxes, eastward and northward turbulent surface stresses, and evaporation and precipitation were downloaded from ERA5 reanalysis at 0.25° resolution (Hersbach et al., 2018), at this latitude equal to roughly 8 km resolution in the zonal direction and 28 km resolution in the meridional direction. ERA5 combines observations and model output, and in the data-sparse Arctic the number of independent observations is limited. Uncertainty in ERA5 is estimated from the ensemble spread, which depends in part on the availability of observations (Hersbach et al., 2018). This ERA5 ensemble spread accounts for random uncertainties

in the observations, sea surface temperature, and model physical parameterizations, but not for systemic errors in the model. The ERA5 ensemble spread is not meant to estimate error at a specific point in space and time, but rather to show where the reanalysis is more or less reliable (https://confluence.ecmwf.int/display/CKB/ERA5%3A+uncertainty+estimation). Examining the ERA5 ensemble spread from 21 September to 21 October 2018 in the Beaufort Sea, the Bering Sea, and Gulf of Alaska for all the ERA5 parameters (heat fluxes, surface stresses, evaporation, and precipitation) used to force the mixed layer model showed transiently heightened uncertainty coinciding with passing storms. There were some regions of persistently high uncertainty as well, such as for latent heat flux near the Alaskan coast south of Bering Strait. Overall, it does not appear that our study area suffers from particularly large ERA5 ensemble spread compared to other regions, except for somewhat elevated ensemble spread for sensible heat flux.

Graham et al. (2019) compared January-May meteorological observations collected north of Svalbard to six atmospheric reanalyses, including ERA5. They found that the reanalyses were highly correlated with the observations for wintertime surface meteorological parameters and downwelling longwave radiation, but that all the reanalyses showed poor skill in simulating turbulent heat fluxes over sea ice (Graham et al., 2019). As our study relies on data from Seagliders which do not collect meteorological data, we proceed using the reanalysis, acknowledging ERA5 is an imperfect product that may not accurately capture local conditions, especially in the vicinity of the ice edge.

2.5.1 Comparing observed and remotely sensed temperature and salinity

The observations presented in this paper provide an opportunity for comparison with concurrent remote sensing. Each conservative temperature observation was compared to MODIS-Terra nighttime sea surface temperature averaged within a 15 km box centered on that observation (Figure 2.3a). The closest daily MODIS image in time with any data in the spatial averaging box was used, with candidate MODIS images occurring up to three days before or three days after the observation. Salinity observations were compared to weekly SMOS ARCTIC sea surface salinity (Supply et al., 2020a). The observed salinity on the Practical Salinity Scale PSS-78, rather than the observed absolute salinity, was used to match the units used by the satellite product. Observations from the Seagliders (averaged in the upper 3 m), Wave Gliders (at 0.2 m), uCTD (averaged in the upper 3 m), and *Healy* underway system (at 2.7 m) were distributed unevenly in time, space, and by platform (i.e., all Wave Glider measurements were from a short period of time in a limited area and the *Healy* underway system's rapid sampling meant there were far more underway samples). To account for this, the *Healy* underway and Wave Glider datasets were subsampled at 15 minute and 150 minute intervals, respectively, to create a comparison dataset more representative of the entire region and time period. Plots of in situ data from individual platforms vs. satellite data showed the same general patterns as the multi-platform comparison.

The MODIS SSTs tended to be warmer than observations, with this difference exacerbated at temperatures of less than 0°C (i.e., as the ocean approached freeze up,

Figure 2.3a). MODIS measures the skin sea surface temperature, which is generally lower than the underlying ocean temperature due to the temperature gradient resulting from heat flow from the ocean to the atmosphere (Minnett et al., 2019). The temperature change across the thermal skin averages 0.17°C, with larger differences expected for low wind conditions (Minnett et al., 2019). The thermal skin effect undoubtedly contributed to the temperature difference between the observed and MODIS SST, but as the MODIS SSTs were generally *warmer* than the observed SSTs, with differences of ~1°C at lower temperatures (Figure 2.3a), we do not expect the thermal skin effect to be the primary reason for disagreement between the MODIS and observed SSTs.

The standard deviation of the differences between in situ sea surface salinity (SSS) and concurrent SMOS SSS was 1.66 psu, with larger differences common at in situ salinities typical of the meltwater (Figure 2.3b). The L-band radiometer used to derive satellite SSS only measures the top centimeter of the ocean, so near surface stratification contributes to differences between observed and SMOS SSS, with saltier observations expected when the stratification is stronger or the salinity data are collected deeper in the water column (Supply et al., 2020b). However, the observed salinities in the meltwater were *fresher* than the satellite SSS, (Figure 2.3b) meaning stratification cannot explain the disagreement. Previous comparisons between satellite SSS and in situ Arctic Ocean data show relatively large discrepancies in regions with cold water and sea ice contamination (Fournier et al., 2019), in line with our finding of larger discrepancies in meltwater conditions.

These comparisons demonstrate the importance of in situ observations, particularly for smaller scale features or conditions typical of cold and stratified meltwater. As a further consideration, this study will demonstrate the importance of mixed layer depth variability to freeze up timing variability (Chapter 2.4), the characterization of which requires in situ observations. Despite these shortcomings, the MODIS data in particular provided useful regional-scale context in visualizing the extent of the meltwater (Figure 2.2).

2.6 Surface velocities

To calculate geostrophic velocity, DOT data were linearly interpolated to a regularly spaced latitude/longitude grid with approximately 15-km spacing and smoothed with a 2-D Gaussian kernel using the MATLAB imgaussfilt function with a standard deviation of 0.5. Geostrophic velocities were calculated from the smoothed DOT = η as

$$u_g = -\frac{g}{f}\frac{\partial \eta}{\partial y}, v_g = \frac{g}{f}\frac{\partial \eta}{\partial x} \quad (2.2)$$

The average velocity in the Ekman layer was calculated from ERA5 horizontal turbulent surface stresses τ^x and τ^y as

$$u_{Ek} = \frac{\tau^y}{f\ \rho_0\ D_{Ek}}, v_{Ek} = -\frac{\tau^x}{f\ \rho_0\ D_{Ek}} \quad (2.3)$$

with the reference density $\rho_0 = 1026$ kg m^{-3} and the Coriolis parameter $f = 2\Omega\ sin(latitude)$. Ekman theory describes steady flow that develops over timescales

longer than an inertial period, so the time series of each component of surface stress at each ERA5 grid point was low-pass filtered with a fifth order Butterworth filter to retain stresses with periods of at least 16 hours, slightly longer than the 12.5-hour inertial period at this latitude, before applying Equation 2.3.

2.7 Mixed layer modeling

The atmospheric influence on the ocean mixed layer was examined using the one-dimensional upper ocean mixing model of Price et al. (1986), hereafter called the Price–Weller–Pinkel (PWP) model. In each PWP timestep, heat and freshwater are added to (for ocean heating/precipitation) or subtracted from (for ocean cooling/evaporation) the water column. The water column overturns if these subtractions make the density structure unstable, entraining successively deeper depth bins until the stratification is stable. Momentum imparted by surface stress is then added to the mixed layer and additional depth bins are entrained into the mixed layer until the bulk Richardson number R_b and gradient Richardson number R_g exceed critical values:

$$R_b = \frac{g\Delta\rho h}{\rho_0(\Delta \boldsymbol{V})^2} \geq 0.65 \qquad 2.4$$

$$R_g = \frac{g\frac{\partial\rho}{\partial z}}{\rho_0\left(\frac{\partial \boldsymbol{V}}{\partial z}\right)^2} \geq 0.3 \qquad 2.5$$

Where h is the mixed layer depth and Δ denotes the difference between the (homogenized) mixed layer and the depth bin just below the mixed layer. The bulk

Richardson number requirement simulates entrainment at the base of the mixed layer; if R_b falls below the critical value, pycnocline depth bins are entrained and their properties distributed throughout the mixed layer until the R_b criterion is satisfied. The gradient Richardson number requirement simulates shear flow instabilities in the stratified transition layer below the mixed layer; if R_g falls below the critical value at any point in the stratified part of the profile, adjacent depth bins are mixed until the R_g criterion is satisfied throughout the profile. The theoretical requirement for shear instability is $R_g < 0.25$, but here we follow Price et al. (1986) and mix for $R_g < 0.3$.

We forced the PWP model with surface heat fluxes, surface stresses, and evaporation and precipitation from ERA5 reanalysis (Chapter 2.2.5). For each observed profile, ERA5 atmospheric forcing was averaged in a 30-km box centered at the profile's location; most model runs used data from four ERA5 grid cells though some used data from as many as eight ERA5 grid cells, depending on how the observation's location aligned with the ERA5 grid. The net shortwave heat flux was distributed throughout the water column according to an extinction coefficient of 0.38 (Price et al., 1986), an appropriate value for clear, mid-ocean Type 1A water (Paulson and Simpson, 1977). Phytoplankton and CDOM absorption are neglected as their effects on ocean optical properties in the deep Beaufort basin are small (Antoine et al., 2013). The sum of the net longwave, sensible, and latent heat fluxes was added to the shallowest depth bin. The PWP model was used to explore the ocean's evolution as it cooled to freezing, so we assumed that the ocean was ice-free and did not include freshwater/salt additions due to ice melt/growth. The PWP depth bin size was 1 m and the deepest bin was 50 m.

Surface forcing was interpolated to 10-minute temporal resolution to run the PWP model with a 10-minute timestep. Use of a short timestep was necessary because when ocean heat loss integrated over a longer timestep was extracted from the uppermost model cell, the water in that cell could momentarily fall below the freezing point. Distributing cooling over a larger number of short timesteps caused static overturn without the surface cell falling below freezing.

The momentum and scalar diffusivities were set to 10^{-6} m^2 s^{-1} following Dewey et al. (2017). The mixing layer depth in the PWP experiments was the depth at which density was at least 0.01 kg m^{-3} greater than the surface density, consistent with the Beaufort Sea PWP experiments of Toole et al. (2010).

3 Observations

3.1 Overview

The following sections show how horizontal advection of sea ice meltwater hastened freeze up. Melting sea ice that lingered in the southern Beaufort Sea created a cold, fresh, and shallow mixed layer (Chapter 2.3.2). In situ Seaglider and ship-based observations documented the northward advection of this feature during the three weeks preceding freeze up (Chapter 2.3.3, Figure 2.2). The meltwater advection can be explained by the combination of Ekman and geostrophic velocities (Chapter 2.3.4).

3.2 Ice and ocean conditions before meltwater advection

Ice retreated from the central Beaufort Sea in late July and early August 2018 (Figure 2.1). The study area was roughly delineated by four subsurface moorings installed as part of the SODA program; while data from those moorings are not used in

this study, mooring locations are marked by star symbols on maps as "landmarks" to orient the reader. The primary ice edge was northeast of the study area, and an additional area of ice separate from the main ice pack persisted in the southern Beaufort Sea. This remnant ice became a distinct patch in the fourth week of August 2018 (Figure 2.1). At that time, its extent was about $5x10^4$ km^2, with an average sea ice concentration of about 50% (not shown). Ice extent and concentration then declined to about $1x10^4$ km^2 and 15%, respectively, by mid-September (not shown). The remnant ice then moved northwestward and continued to shrink, leaving the study region ice-free after 28 September. The local decrease in the remnant ice extent (Figure 2.1) and concentration indicates most of it melted locally in the southern Beaufort Sea.

Initially, the upper ocean was relatively cold only near the ice edges. MODIS SST data from 14–21 September showed a band of cold water extending roughly 100 km from the northeastern MIZ as well as a localized cold patch surrounding the melting remnant ice (Figure 2.2a,e). In situ observations agreed with this MODIS SST pattern. Seagliders observed cooler mixed layer temperatures at the northward limit of their transect, aligning with the SST gradient seen in the satellite imagery adjacent to the northern MIZ (Figure 2.2a). Wave Gliders observed a near-surface (9 m) horizontal conservative temperature gradient that roughly aligned with that in the satellite imagery near the remnant ice (Figure 2.2a, Figure 2.4a). Some differences between the MODIS and observed conservative temperatures in Figure 2.2a could be because the observations were from later than the MODIS period (Wave Gliders 19–23 September, Seagliders 22–26 September; the concurrent MODIS data were too limited by clouds to

discern SST gradients). However, a careful comparison of observed near-surface conservative temperature and concurrent MODIS SST showed that MODIS temperatures were warmer than the observations (Figure 2.3a, additional discussion in Chapter 2.2.5.1).

Away from the ice edges, the late summer mixed layer had relatively uniform properties. In the central part of a 22–26 September Seaglider transect the mixed layer was about 25 m deep with conservative temperature of approximately 0°C and absolute salinity of approximately 26.5 g kg^{-1} (Figure 2.5b,c). Below the mixed layer, isopycnals sloped downward with increasing latitude (Figure 2.5b,c). The northern MIZ's influence was apparent at the northern end of the transect, where the mixed layer was somewhat colder, saltier, and deeper (depth about 30 m, conservative temperature of approximately –0.5°C, absolute salinity of approximately 26.9 g kg^{-1}, not shown).

Seaglider conservative temperature-absolute salinity profiles collected on 26 September in the cold footprint of the remnant ice show surface conditions qualitatively consistent with modification by local ice melt (Figure 2.4e,f). Ice melt would be expected to cool, freshen, and stratify near-surface waters, and in the Seaglider observations the mixed layer was near-freezing (Figure 2.4e), relatively fresh and stratified (Figure 2.4a,f), and was about 10 m deep (Figure 2.4e,f). Absolute salinity increased by about 1 g kg^{-1} between the surface and 20 m where a near surface temperature maximum was approximately 1–1.5°C warmer than the relatively cold sea surface.

Sea ice melt releases very low salinity water which can mix downward,

increasing stratification in the upper ocean and creating a seasonal pycnocline referred to by Randelhoff et al. (2017) as a meltwater layer, which is distinct from the isolated lenses of pure sea ice melt that can accumulate in quiescent areas under sea ice. Such a stratified surface layer is not pure ice melt and might more accurately be described as "modified meltwater", but we follow Randelhoff et al. (2017) and call this phenomenon meltwater. We now discuss whether the observed layer of cold, fresh surface water in the remnant ice area (Figure 2.4e,f) could have been caused by local ice melt mixing with ambient water.

Gade (1979) developed an equation to estimate the product properties of ice melt in ocean water which accounts for the latent heat necessary for the change of state and assumes a turbulent boundary between the ocean and the ice. The Gade Line slope $\frac{d\theta}{dS}$, reformulated by Herraiz-Borreguero et al. (2013), is given by

$$\frac{d\theta}{dS} = \frac{L}{S_0 c_w} + \frac{(\theta_f - T_i)c_i}{S_0 c_w} + \frac{(\theta_0 - \theta_f)}{S_0} \qquad 2.6$$

Where L is the latent heat of fusion for ice, θ_0 and S_0 are the potential temperature and salinity of the ambient water, θ_f is the ocean freezing temperature, T_i is the ice temperature, and c_w and c_i are the specific heat capacities of water and ice, respectively. As the remnant ice in our study was melting during summer, we assume it was already close to its melting temperature and use T_i = –2°C. The first term on the right hand side dominates so this assumption has little impact on the results.

Gade Lines show that ice melt by the ambient water observed outside the

meltwater would generate product water with salinities between approximately 25.8 g kg^{-1} and 26 g kg^{-1} (Figure 2.6). The temperature and salinity profiles in the meltwater (black and purple points on Figure 2.6) approximately follow the Gade Lines from the ambient water conditions (blue points in Figure 2.6) until around 10 m depth, at which point they freshen further. This suggests an additional source of liquid fresh water was necessary to produce the observed salinities in the upper 10 m.

To estimate the volume of ice melt necessary to generate the observed salinity profiles, we calculate the upper ocean salt deficit. The salt deficit quantifies the thickness of ice growth required to increase the mixed layer salinity to match the salinity at a reference depth (Wilson et al., 2019) but can also be thought of as the ice melt necessary to freshen the surface layer relative to the salinity at a reference depth. For the average Seaglider salinity profile in the remnant ice area (Figure 2.4f), we can infer that 20 m is roughly the base of the pycnocline formed by the ice melt based on the presence of a near surface temperature maximum below this depth (Figure 2.4e). The salt deficit *SD**, which has units of ice thickness, is defined as (Wilson et al., 2019):

$$SD^* = \frac{1}{\Delta S_i}\int_0^{z_c}[S(z_c) - S(z)]dz \qquad 2.7$$

Where z_c is the reference depth and ΔS_i is the salinity difference between the ocean surface and the sea ice. Assuming an ice salinity of 6 g kg^{-1}, *SD** = 0.7 m for z_c = 20 m. However, the value of *SD** for our salinity profile is quite sensitive to the choice of z_c as the water column remains strongly stratified below 20 m (Figure 2.4f). Increasing z_c

to 30 m to include all of the water column above the temperature minimum associated with the previous winter's mixed layer increases *SD** to nearly 3 m, an unreasonably large amount of local ice melt. However, it seems unlikely that ice melt could have mixed to 30 m while the subsurface temperature maximum between 20 m and 30 m persisted. Above 10 m, the depth at which the observed profiles departed from the Gade Line estimates, *SD** = 0.1 m. These calculations assume 100% ice concentration; attaining the necessary ice melt volume from patchy ice cover requires thicker ice than the SD* values reported above.

In summary, the salt deficit calculation suggests that the freshwater equivalent of roughly 1-1.5 m of patchy ice melt could result in the fresher surface layer observed in the remnant ice area while the departure of the observed temperature-salinity profiles from the Gade Lines in the upper 10 m suggests that an additional source of liquid freshwater was necessary to fully explain the temperature-salinity properties observed in the meltwater. Precipitation is unlikely as the freshwater front was sharp, requiring highly localized rainfall, and a plume of river water is unlikely at this distance from the coast. Ekman pumping could have accumulated fresher surface water in this area, increasing the apparent freshening beyond that attributable to one-dimensional ice melt. The previous water in this area could have been anomalously fresh before ice melt occurred; as we lack earlier ocean observations, we cannot determine the role of the initial conditions. We proceed with the assumption that local ice melt was primarily responsible for the formation of the cold, fresh, and shallow surface layer, which will be called the meltwater, acknowledging that the temperature and salinity profiles

suggest a minor contribution from an additional liquid freshwater source. The lateral transition from fresher to saltier surface salinities will be called the meltwater front.

Wave Gliders observed a strong salinity gradient at the edge of the meltwater front (Figure 2.4a) near where satellite-derived synthetic aperture radar imagery showed wave-like and filamentous structures at the ice edge that evolved substantially over several days (Figure 2.4a,d). Density measured at 0.25 m and 9 m by a Wave Glider that crossed the meltwater front increased by about 0.5 kg m^{-3} over the 10-km transect (Figure 2.4b). The horizontal buoyancy gradient $M^2 = \frac{\partial b}{\partial x'}$ reached 10^{-6} s^{-2} (Figure 2.4c) where the buoyancy $b = -\frac{g\rho}{\rho_0}$ was calculated using the gravitational acceleration g and the reference density $\rho_0 = 1026$ kg m^{-3}. M^2 was calculated in the along-track direction x' between pairs of successive Wave Glider density measurements so does not include contributions from cross-track gradients. The distance between Wave Glider measurements along this transect averaged 750 m and ranged between 590 m and 890 m. The roughly six-hour cross front transit (Figure 2.4b,c) was fast enough, compared to the local inertial period, that the observations can be viewed as a snapshot of the front.

3.3 Meltwater advects northward over several weeks

In the 30 September to 7 October MODIS SST image a cold filament-like structure extended northward from the meltwater around the remnant ice (Figure 2.2b). Consistent with the SST imagery, Seagliders observed a colder and fresher surface layer spreading northward along their transect from 3–10 October (Figure 2.2b,c,f,g).

Because of this layer, mixed layer depth decreased to about 15 m (Figure 2.5e,f). Mixed layer conservative temperature and absolute salinity (conservative temperature around –1°C, absolute salinity around 25.7 g kg^{-1}) were similar to those observed earlier in the area of the remnant ice (Figure 2.6). Similarity in upper ocean conservative temperature and absolute salinity properties along with the apparent coherence of the cold filament in the SST imagery strongly suggest northward advection of the meltwater. The 3–10 October Seaglider data show that the meltwater front had weakened, with M^2 reduced to 20% of that measured earlier by the Wave Glider (roughly 80 km to the south).

Satellite SST imagery was too limited by cloud cover to fully visualize the meltwater after 7 October, but the in situ observations suggest it moved northward and westward in subsequent days. The meltwater occupied the entirety of the next Seaglider transect, sampled from 6–11 October, indicating continued northward meltwater advection (Figure 2.2c,g). Observations by Seagliders, uCTD, and *Healy*'s underway system from 11–14 October show that warmer and saltier waters replaced those found in the meltwater's former location, but that cold and fresh surface conditions were present further west (Figure 2.2d,h). These observations suggest westward advection of the meltwater along with a westward shift of meltwater-adjacent waters. An isolated ice patch formed on 12 October coincident with the meltwater location (Figure 2.2d,h). Heterogeneity in surface temperature and salinity persisted until the onset of freeze up, and freeze up occurred earliest in the meltwater. The mechanisms by which the meltwater hastened freeze up are discussed in Chapter 2.4.

3.4 Simulated advection by geostrophic and Ekman velocities

The observed northward advection of the meltwater can be explained by a combination of geostrophic and Ekman advection. Simulated trajectories were created using geostrophic velocity (Equation 2.2), the average velocity in the Ekman layer (Equation 2.3), and the combination of the two. For each trajectory, "tracking" was initialized on 21 September near where the Wave Gliders showed the edge of the meltwater (Figure 2.7), then the location was updated at hourly time steps (corresponding to the times at which ERA5 surface stress was available) using the appropriate velocity. Average velocities in the Ekman layer were calculated using the ERA5 surface stress that was closest in space at the given timestep and geostrophic velocity was taken as the spatially closest DOT geostrophic velocity. To explore the advection attributable to each of these processes, separate trajectories were advanced with the average Ekman layer velocity only, the geostrophic velocity only, or the sum of the two.

Ekman depth was estimated as D_{Ek} = 10 m to match the average mixed layer depth in the remnant ice area Seaglider profiles (Figure 2.4e,f). The theoretical Ekman depth is $D_{ek} = \sqrt{\frac{2A}{f}}$ where A is the eddy viscosity. A typical value of A = 0.1 m^2 s^{-1} (e.g., Vallis, 2017, pg. 204) at the latitude of our study area suggests an Ekman depth of about 37 m, considerably larger than the value that we use. However, Ekman layer theory assumes the ocean has a constant density, and observations indicate that stratification tends to inhibit vertical momentum flux and shallow the Ekman depth

(e.g., Price et al., 1987). It is therefore reasonable to expect the Ekman depth to be less than the theoretical value in the strongly stratified meltwater we discuss.

Previous observations under sea ice in the Beaufort Sea from October to March indicate a median Ekman depth of 11 m, with most Ekman depths shallower than mixing depths (Cole et al., 2014). While our study is in ice-free waters so these results might not apply directly, they do demonstrate the shoaling effect of stratification on the Ekman depth and indicate that the mixed layer depth is not an unreasonably shallow estimate for the Ekman depth. The sensitivity of the simulated trajectories to the choice of Ekman depth is discussed shortly.

Meltwater advection can be tracked in the observations using the 26 g kg^{-1} isohaline outcrop as a proxy for the meltwater edge (triangle symbols on Figure 2.2 and Figure 2.7). Ongoing upper ocean cooling altered surface density slightly, motivating the use of an isohaline rather than an isopycnal. The simulated trajectories are evaluated by their ability to reproduce the observed advection.

The ocean geostrophic velocity calculated from DOT showed cyclonic circulation with a length scale of approximately 100 km located north of the remnant ice area (Figure 2.7). This geostrophic circulation agrees with the sloping isopycnals below the mixed layer seen in the southern half of the first Seaglider transect (Figure 2.5b,c), which crossed the northern part of the cyclonic circulation seen in the DOT. This observed isopycnal slope also agrees qualitatively with the large-scale *anticyclonic* circulation of the Beaufort Gyre, but the substantial weakening of this subsurface meridional density gradient between Seaglider transects (compare Figure 2.5b,c and

Figure 2.5e,f) suggests that it was attributable in part to transient circulation like the cyclonic circulation derived from the DOT.

Trajectories calculated from the geostrophic velocity alone followed the cyclonic circulation northward but fell short of the observed extent of northward advection (not shown). Although the full DOT survey of the study area took more than a month and consisted of a series of parallel, roughly meridional satellite tracks, the orientation of these tracks meant that the zonal DOT gradients were captured on timescales of only a few days, with the region north of the meltwater surveyed from 16–22 September. The shorter timescale needed to resolve the zonal gradients than the meridional gradients along with the fact that the meltwater area was surveyed shortly before the observed northward advection of the meltwater began give us relatively more confidence in the northward geostrophic circulation responsible for northward meltwater advection than in other aspects of the calculated geostrophic velocity field.

Ekman transport advected the meltwater northward, but Ekman-only advection was also insufficient to match the observed northward advection (not shown). For a 10 m Ekman depth, simulated Ekman trajectories from 21 September to 3 October went southwestward and then northeastward back to near their original locations. From 3–11 October, Ekman trajectories extended 50 km to the northeast (regionally averaged Ekman velocity shown in Figure 2.7).

Neither Ekman-only nor geostrophic-only advection was sufficient to explain the filament's northward advection, but the simulated trajectories driven by the combined velocities did transport surface water far enough to be in coarse agreement

with the observations (Figure 2.7). Additionally, the more western simulated trajectories, initiated in the core of the meltwater, aligned well with the early ice formation patch.

The average mixing layer depth in the remnant ice area Seaglider profiles was 6 m (whereas the average *mixed* layer depth used as the Ekman depth previously was 10 m). When tracking was initiated in the same start positions as before and advected using the combined velocities calculated with a 6 m Ekman depth, most trajectory endpoints clustered in the same region as in the 10 m Ekman depth simulation though the easternmost trajectories terminated somewhat further north (not shown). Even with a thin, 6 m Ekman layer, the trajectories advected by Ekman velocity only did not travel far enough north to match the observations, affirming that the geostrophic component of the circulation was necessary to explain the observed meltwater advection (not shown). The average mixed layer depth increased to 14 m on a later Seaglider transect through the meltwater (Figure 2.8k), indicating that the Ekman depth within the meltwater could also have increased with time. When tracking was initiated in the same start positions as before and advected using the combined velocities calculated with a 15 m Ekman depth, some trajectories terminated between 146°W to 148°W and 74°N to 75°N, in qualitative agreement with the observations and with the 10 m Ekman depth results (not shown). The main difference from the 10 m Ekman depth results was that some of the western trajectories were more strongly affected by the geostrophic circulation and were advected southward after 3 October.

These simple surface current advection simulations are not meant to stand in for

a fully coupled three-dimensional ocean model, which could be used to better understand the evolution of the meltwater. For example, our use of the vertically-averaged velocity in the Ekman layer neglects the expected Ekman velocity spiral which could shear meltwater over ambient water at the edges of the meltwater patch. The simulations do however demonstrate that, within a range of reasonable Ekman depths, the surface currents can explain the observed northward advection of the meltwater.

4 Mixed layer heat budget

4.1 Overview

Ocean observations described in the previous section show a co-occurrence of meltwater presence and early sea ice advance seen by passive microwave satellites. This co-occurrence suggests meltwater advection influenced the timing of freeze up. This section quantifies that link, demonstrating that decreases in mixed layer temperature and mixed layer depth due to meltwater advection hastened freeze up by several days. Additionally, a mixed layer heat budget shows that, in the area affected by the meltwater, advection was a leading cause of mixed layer heat loss.

The mixed layer heat budget was developed for a subset of the study area, along a transect that was affected by meltwater and was repeatedly sampled by Seagliders (see pink highlighting in Figure 2.2e–h). Focusing on a repeatedly sampled transect eliminates differences attributable to pre-existing heterogeneity in upper ocean structure. We name the four Seaglider occupations Transects 1–4, described next. Transect 1, sampled from 26–29 September, was completed before the meltwater

entered the study area; the mixed layer conditions observed on this first transect are the initial conditions against which subsequent observations are compared (Figure 2.8a–d). Transect 2, sampled from 30 September to 5 October, crossed into the meltwater, with meltwater present at the southern end of the transect but absent from the northern end (Figure 2.8e–h). Meltwater filled Transect 3, sampled from 6–10 October (Figure 2.8i–l). Transect 4, sampled from 11–14 October, did not contain meltwater (Figure 2.8m-p).

Changes in mixed layer heat content are due to horizontal and vertical processes. Prior to freezing, vertical (or one-dimensional) processes include net surface heat exchanges with the atmosphere as well as heat exchanges with the underlying pycnocline. Horizontal processes include horizontal advection of colder (or warmer) waters, directly bringing the mixed layer closer to (or further from) its freezing temperature, as well as horizontal advection of waters with different salinity, which impacts the mixed layer depth and stratification.

The definition of mixed layer heat content (Equation 2.1) means the mixed layer heat content goes to zero as the mixed layer temperature approaches the freezing temperature. Once the mixed layer has lost its heat, frazil ice begins forming if further heat is lost to the atmosphere. Thus, the freeze up process initiates when the mixed layer reaches the freezing temperature, which will be referred to as the onset of freeze up. If atmospheric and oceanic conditions remain favorable for ice growth, sea ice will mature to a stage at which it is visible in remote sensing. This growth period requires time, so the onset of freeze up defined by freezing temperature mixed layers is not the same as the freeze up timing inferred from satellite products (i.e., in Figure 2.1).

Our goal is therefore to create mixed layer heat budgets in the presence and absence of meltwater to quantify the importance of meltwater advection to mixed layer heat loss integrated throughout the autumn season.

4.2 Heat budget development and results

As described in Chapter 2.4.1, the mixed layer heat budget contains three terms: net surface heat flux, which we infer from ERA5, heat exchange with the pycnocline, which we estimate using the PWP model, and advection. Heat exchange between the pycnocline and the mixed layer driven by entrainment due to mixed layer deepening, and by turbulent diffusion, are combined into a bulk pycnocline heat exchange. The differences between observed changes in mixed layer heat content, calculated in an Eulerian reference frame using the repeat transects, and changes simulated by the one-dimensional PWP model, which excludes advection, are taken as an estimate of horizontal advection.

For the Transect 1 heat budget, the PWP model was initialized with observed conservative temperature and absolute salinity profiles collected on the transect. Separate model runs for each profile were forced with ERA5 heat flux, surface stress, and surface freshwater flux, and run until the modeled mixed layer reached the freezing temperature, interpreted as the modeled onset of freeze up. Mixed layer properties observed on the meltwater-free Transect 4, which was sampled after ambient water replaced meltwater on the transect (Figure 2.2d,h), agreed with properties predicted by the PWP model runs initiated on the meltwater-free Transect 1 (Figure 2.8m–p). Agreement between observations and concurrent model predictions demonstrates that

one-dimensional processes adequately described mixed layer evolution outside of the meltwater and indicates that advection was not an important component of the mixed layer heat budget for Transect 1. The modeled onset of freeze up for Transect 1 on average occurred on 21 October (Figure 2.9a). This modeled freeze up onset is comparable to the satellite-observed 18 October ice advance southwest of the meltwater (Figure 2.1). Differences in the definition of freeze up would be expected to drive differences in timing between these estimates, but their rough agreement supports the validity of the modeled mixed layer dynamics.

The PWP model results for Transect 1 profiles were used to create a heat budget representative of mixed layer evolution without meltwater advection. Net surface heat loss for each profile was estimated by integrating the ERA5 heat flux from the time of the initial observation to the time of the modeled onset of freeze up. Time integrated mixed layer heat exchange with the pycnocline was calculated as the change in pycnocline heat content over the same time period. The pycnocline heat content was the depth integrated heat content between the base of the mixed layer and 50 m, the deepest depth simulated in the PWP model. As PWP does not account for advection, the *change* in modeled pycnocline heat content was due almost entirely to heat exchange with the mixed layer. Diffusion altered the temperature profile within the pycnocline somewhat, meaning the choice of lower integration bound could influence the modeled pycnocline heat content if heat diffused into or out of the integration volume from below, but as diffusion was intentionally small in our model runs and we integrated the heat content of the entire modeled pycnocline, this effect is not important to the calculated change in

pycnocline heat content.

Average surface heat fluxes throughout the PWP model runs were between −45 W m^{-2} and −65 W m^{-2}, with positive fluxes directed downward and higher values for later-freezing profiles. This pattern makes sense because atmospheric heat loss accelerated as autumn progressed, so later-freezing profiles were exposed to larger, late-season heat fluxes for longer periods of time. The largest surface heat flux during our study period was around −150 W m^{-2} and occurred on 7 October.

Mixed layer heat content changes on Transect 1 were almost entirely due to heat loss to the atmosphere, which, on average, totaled 128 MJ m^{-2} between the initial observations and modeled freeze up (Figure 2.9b). Heat gained by the mixed layer from the pycnocline averaged 1.4 MJ m^{-2} (Figure 2.9b), small compared to heat loss to the atmosphere. Agreement between model predictions and later observations outside of the meltwater indicates that advection was negligible for Transect 1 profiles. Transect 1 results can be thought of as simulating mixed layer evolution to the onset of freeze up in the absence of meltwater advection, and therefore approximating the mixed layer heat budget for waters adjacent to the meltwater, which were not sampled directly. Mixed layer properties observed on the meltwater-containing Transects 2 and 3 deviated substantially from those predicted by PWP simulations initiated on the meltwater-free Transect 1. Transect 2 crossed into the meltwater and thus included a mix of profiles with and without meltwater; we focus on profiles that contained meltwater as we assume that the previously-discussed Transect 1 results are representative of meltwater-absent conditions. The observed meltwater mixed layer

(defined to include observed profiles with surface absolute salinity below 26 g kg^{-1}) was about 0.55°C colder and 13 m shallower than the model predictions (Figure 2.8e–l).

These differences indicate a strong role for advection in setting the mixed layer properties observed on Transects 2 and 3. For model runs initiated with meltwater-containing Transect 2 and 3 observations, the modeled onset of freeze up on average occurred on 11 October (Figure 2.9c,e). This timing agrees with the satellite-observed ice patch that formed on 12 October adjacent to the previously observed meltwater (Figure 2.2d,h). The agreement in satellite-observed and modeled freeze up timing in the meltwater implies that while the meltwater's presence was due to advection, the evolution within the meltwater was one-dimensional.

Developing a meltwater-influenced heat budget using observations on Transects 2 and 3 requires two additional steps beyond those followed when meltwater was absent. The first problem is that Transects 2 and 3 were sampled later than Transect 1. It is the time-integrated loss of heat from the mixed layer throughout the autumn cooling season, rather than instantaneous heat fluxes into or out of the mixed layer, that controls the onset of freeze up. Thus, it is important that the integrals of mixed layer heat fluxes for meltwater-present and meltwater-absent heat budgets begin at roughly the same time.

To extend the Transect 2 and 3 heat budgets, we used Transect 1 model results to estimate the vertical heat budget terms integrated from the time Transect 1 was sampled to the times when Transects 2 and 3 were sampled. In other words, Transect 1

model results, run until the time when observations were collected on Transect 2 and 3, were added to the vertical heat budget terms derived from model runs initiated on those transects and run until the modeled onset of freeze up. The vertical heat budget terms for Transects 2 and 3 are thus the sum of two sets of model runs spanning two different time periods: Transect 1 model results prior to the Transect 2 or 3 observations, and additional model runs initiated with the Transect 2 or 3 observations and run until the modeled onset of freeze up. Heat budget terms were combined by averaging Transect 1 model results in latitude bins and then adding them to Transect 2 and 3 model results binned in the same manner.

The second difference between the meltwater-absent Transect 1 heat budget and the heat budgets for Transects 2 and 3 is that meltwater advection played a major role in mixed layer heat loss for the later observations. We assume that differences between observed mixed layer properties and concurrent modeled mixed layer properties can be attributed to horizontal advection. Therefore, the advective component of the mixed layer heat budget for Transects 2 and 3 was estimated as the difference between the observed mixed layer heat content and the concurrently-predicted mixed layer heat content from PWP model runs initiated on Transect 1 (see Figure 2.8h,l,p).

Heat loss to the atmosphere for meltwater-containing profiles on Transects 2 and 3 was about 50 MJ m^{-2} (Figure 2.9d,f). Heat gained from the pycnocline was variable, with maximum values of up to 44 MJ m^{-2} (Figure 2.9d). The larger pycnocline heat exchange within the meltwater relative to outside the meltwater was likely due to increased mixing caused by shear instabilities at the base of the meltwater mixed layer,

whose shallower depth resulted in larger acceleration for a given surface stress. The differences between observed and concurrent modeled mixed layer heat content indicated an advective mixed layer heat loss of about 90 MJ m^{-2} (Figure 2.9d,f).

Our observations do not span the entire autumn cooling period. Net surface heat flux in ERA5 became net negative around 10 September, and about 50 MJ m^{-2} of ocean heat was lost to the atmosphere before Seaglider sampling began (not shown). Lacking ocean observations, we cannot estimate pycnocline and advective heat budget components during this intervening period. However, accounting for this earlier ocean cooling implies seasonally integrated heat loss to the atmosphere (50 MJ m^{-2} prior to the earliest observations + 50 MJ m^{-2} between observations and freeze up in the meltwater) was comparable to the mixed layer heat loss associated with meltwater advection (90 MJ m^{-2}). This demonstrates that meltwater advection played a leading role in mixed layer heat loss integrated throughout the autumn. It also shows that, despite relatively higher values within the meltwater, heat exchanges with the pycnocline were of secondary importance to the mixed layer heat budget compared to heat loss to the atmosphere and advection.

5 Restratification hastens freeze up in northern study area

This section shifts focus to the northern part of the study area and briefly discusses a freshwater advection event separate from the meltwater advection described previously. Freeze up swept across the northern study area on 14 October (Figure 2.1), which was several days earlier than predicted by PWP model runs initiated by observations in the area on or before 7 October. Though not recreated in PWP model

runs, shoaling mixing depth, which would confine heat loss to a smaller portion of the water column, offers a possible explanation. Consistent with this mechanism, Seaglider observations from 12–15 October show that the upper 15 m of the water column freshened, decreasing the average surface density by 0.1 kg m^{-3} compared to the earlier profiles (see the example profiles in Figure 2.10). PWP runs initiated with these later profiles had shallower cooling and an average onset of freeze up of 15 October, agreeing with the satellite-derived freeze up timing.

The observed restratification was likely due to lateral processes as it was not simulated by the one-dimensional PWP model forced by ERA5 surface heat and freshwater fluxes. The area was ice-free when restratification was observed (Figure 2.10), so local ice melt also cannot explain the surface freshening. Lateral processes could act to spread buoyant meltwater and thus create shallow stratification. The model results suggest that this restratification accelerated freeze up.

6 Summary and discussion

This study demonstrates how freshwater advection alters upper ocean stratification and leads to spatial variability in freeze up timing. Nearly 800 ocean conservative temperature and absolute salinity profiles characterize the open water region in the central Beaufort Sea, immediately prior to freeze up in 2018, at high spatial and temporal resolution. Few previous studies capture ice-free Arctic Ocean conditions at these small scales during this critical time of year due to the risks to instrumentation when freeze up is imminent or in progress. The observed oceanic modulation of freeze up means forecasting efforts should consider the three-

dimensional evolution of the mixed layer and its impacts on sea ice development.

In one case of freshwater advection, a cold and fresh surface meltwater layer caused by melting remnant ice in the southern Beaufort Sea advected roughly 100 km in several weeks. Meltwater hastened the onset of freeze up by cooling and shoaling the mixed layer, with the result that ice advanced in meltwater-affected areas several days earlier than in surrounding areas where meltwater was absent. Mixed layer shoaling limited the volume of surface water that had to cool to the freezing temperature before ice could form. Outside of the meltwater the weaker stratification distributed cooling over a deeper mixed layer and delayed ice formation.

The mixed layer heat budget for the autumn cooling period showed that, outside of the meltwater, regional-scale heat loss to the atmosphere was the dominant means of mixed layer cooling. Within the area affected by meltwater, advection was nearly as important as heat loss to the atmosphere for seasonally integrated mixed layer heat loss. Heat gained by the mixed layer from the pycnocline was of secondary importance.

While previous research concluded that advection plays a minor role in Beaufort Sea upper ocean freshening on seasonal timescales (Dewey et al., 2017), we note that the meltwater front documented in our study would be indiscernible in the SIZRS dataset used in Dewey et al. (2017) which has temporal resolution of one month and spatial resolution of 1° of latitude. While determining the frequency of such advective events is outside the scope of this work, we note that a second filament of cold surface water emanating from the remnant ice area, unsampled in our study, was visible in the satellite sea surface temperature imagery (Figure 2.2b). To the extent that anomalously

cold surface temperatures were a tracer for meltwater, this sea surface temperature pattern suggests that meltwater advection on order 100 km scales may be an important source of upper ocean heterogeneity.

A separate freshwater advection event occurred near the MIZ when the mixing layer freshened by 0.1 g kg^{-1} in the days preceding freeze up. Our observations do not capture the origin of this freshwater or the exact timing of the restratification; however, the mixed layer model's inability to replicate the surface freshening suggests it was not due to one-dimensional surface forcing, and satellite imagery shows that it was not due to local ice melt. We thus attribute the restratification to a lateral flow of freshwater. Our measurements do not resolve the ocean structure associated with the northern MIZ well enough to determine the dynamics contributing to the observed restratification; advection by Ekman, geostrophic, or submesoscale flows are all candidates.

Mixed layer instability associated with the nearby ice edge is one possible explanation for the restratification observed near the northern MIZ, as modeling studies of submesoscale meltwater fronts show that mixed layer eddies can spread meltwater laterally (Horvat et al., 2016; Manucharyan and Timmermans, 2013; Manucharyan and Thompson, 2017). However, the available potential energy is lower in fronts with shallower meltwater layers, and shallow meltwater layers take longer to develop eddies so their dynamics are more likely to be influenced by wind and surface buoyancy forcing (Manucharyan and Thompson, 2017). Timmermans et al. (2012) found that lateral restratification was common in profiles beneath sea ice and noted that the slight density increase below actively mixing layers isolated the rest of the underlying mixed

layer and prevented pycnocline entrainment (Timmermans et al., 2012). We add to their results by showing that diverging mixing and mixed layers precondition freeze up, demonstrating a mechanism by which three-dimensional ocean circulation allows freeze up to advance more quickly than one-dimensional ocean cooling would predict.

While this study has focused on the mixed layer, the Seaglider profiles also captured the northward advection of Pacific Summer Water (PSW, defined by MacKinnon at al. (2021) as water bounded by the 1023.2 kg m^{-3} and 1025.2 kg m^{-3} isopycnals and warmer than 0°C) that was nearly 2°C (Figure 2.6). These PSW warm features were present in some Seaglider profiles collected in the remnant ice area on 26 September (Figure 2.4e, Figure 2.6) and then similarly warm PSW was observed in ~20 km boluses on the Seaglider transect north of the remnant ice area beginning on 5 October (not shown), arriving roughly in tandem with the meltwater (Figure 2.6). The top of the PSW was found at similar salinities at both locations but isopycnals deepened with latitude resulting in a roughly 20 m downward displacement of the PSW as it advected northward (not shown). The later northern profiles showed exceptionally warm PSW at deeper salinities as well (down to S_A=31 g kg^{-1}, Figure 2.6) suggesting downward mixing had occurred. MacKinnon et al. (2021) described a very warm (up to 6°C) PSW jet impinging from the south on remnant sea ice (the same remnant sea ice discussed in this study) and breaking into intrathermocline eddies when observed from 14–17 September 2018. Our observations likely represent the continued subduction and advection of this PSW jet.

The stratification below the meltwater stored a relatively large amount of heat in

a near surface temperature maximum (NSTM) when ice formed. The modeled upper ocean heat content from 0 to 40 m at freeze up for profiles in the meltwater was 100 MJ m^{-2} on average while the modeled upper ocean heat content at freeze up for profiles outside the meltwater was 67 MJ m^{-2} on average. The 40 m heat content integration bound was chosen to represent a typical winter mixed layer depth in this region as Peralta-Ferriz and Woodgate (2015) found Canada Basin winter mixed layer depths averaged 33 m using a more restrictive density change threshold ($\Delta\rho = 0.1$ kg m^{-3} relative to the surface) than used here ($\Delta\rho = 0.25$ kg m^{-3}). The fate of heat entrained from the NSTM by convection or wind-driven mixing depends on the maturity of the overlying ice. Most heat reaching the base of thick, insulating ice is expected to slow the growth of that ice (Timmermans, 2015), whereas Smith et al. (2018) show that a substantial fraction of the heat released by a storm early in the freeze up process escaped directly to the atmosphere with only 30-40% going toward melting the thin pancake ice. In addition, downwelling due to Ekman pumping can cause the NSTM to deepen throughout the autumn and winter (Jackson et al., 2010). If surface mixing is relatively weak, this downwelling may be strong enough to sequester the NSTM below the mixed layer such that it persists through the winter (Steele et al., 2011).

While it is not possible with our dataset to differentiate among these outcomes for the additional heat stored in the meltwater-present NSTM relative to the meltwater-absent NSTM, the larger NSTM heat content at freeze up below the meltwater is nonetheless an important result. At first glance, earlier ice formation in the meltwater

might be expected to result in thicker ice at the end of winter due to a longer ice growth season. However, entrainment of the stronger (warmer and shallower) NSTM below the meltwater could counteract the "head-start" of earlier ice formation and inhibit seasonally integrated ice growth. Ice that thins during winter due to NSTM entrainment retreats earlier the following year, allowing the ocean to absorb more solar radiation the following summer (Jackson et al., 2012). The onset of the spring ice algal bloom is light limited (Leu et al., 2015), so earlier ice retreat also impacts the ice-based ecosystem.

Arctic sea ice forecasting is an area of substantial ongoing research (e.g., Guemas et al., 2016 and references therein), and the importance to stakeholders of predicting freeze up on regional spatial scales has recently been highlighted (Bushuk et al., 2017; Day et al., 2014; Stroeve et al., 2016). Positive sea ice area anomalies during the melt season result in cold sea surface temperature anomalies which can persist throughout the summer, meaning the ocean retains a "memory" of previous ice conditions which preconditions the re-emergence of positive ice area anomalies during freeze up (Blanchard-Wrigglesworth et al., 2011; Day et al., 2014). This re-emergence mechanism means that the timing of ice retreat can be used to statistically predict the timing of ice advance in some parts of the Arctic, with moderate predictive skill in the Beaufort Sea (Stroeve et al., 2016). Modeling studies also show that the inclusion of sea surface temperature information contributes to skillful freeze up forecasting at socioeconomically relevant spatial scales (Bushuk et al., 2019; Sigmond et al., 2016). Our results advance this forecasting paradigm by demonstrating that 1) sea surface

temperature anomalies associated with late ice retreat advect and precondition freeze up in neighboring areas that did not themselves experience anomalously late ice melt and 2) late ice melt can create persistent, anomalously shallow mixed layer depths that also promote early freeze up.

7 Acknowledgments

The authors thank the crews of the USGCG *Healy* and the RV *Sikuliaq* for their expert support in deploying the Seagliders, Wave Gliders, and uCTD. Discussions with members of the SODA team helped develop the ideas presented here. We thank Jody Deming, reviewer Isabelle Giddy, and reviewer Wilken-Jon von Appen for their insightful and constructive comments which improved the paper.

This work contributes to the Stratified Ocean Dynamics of the Arctic (SODA) research program, funded by the Office of Naval Research under grant numbers N000141612377 (LC, CML, LR) and N000141612349 (JT). This material is based upon work supported by the National Science Foundation Graduate Research Fellowship Program under Grant No. DGE-1762114 (LC). Any opinions, findings, and conclusions or recommendations expressed in this material are those of the author(s) and do not necessarily reflect the views of the National Science Foundation.

The authors declare no conflicts of interest.

8 Data availability statement

The ocean observations presented in this paper are available on the University of Washington ResearchWorks archive at http://hdl.handle.net/1773/47135

ERA5 hourly data on single levels were downloaded from the C3S climate data store (https://cds.climate.copernicus.eu/#!/home). The link to the reanalysis on surface/single levels is https://cds.climate.copernicus.eu/cdsapp#!/dataset/reanalysis-era5-single-levels?tab=overview

Sea ice concentration from AMSR2 was downloaded from the University of Bremen data archive at https://seaice.uni-bremen.de/data/amsr2/asi_daygrid_swath/n3125/2018/

Level 3 Daily and 8-Day average MODIS-Terra sea surface temperature data were downloaded from the Physical Oceanography Distributed Active Archive Center at NASA/JPL from https://podaac-tools.jpl.nasa.gov/drive/files/allData/modis/L3/terra/11um/v2019.0/4km

Dynamic ocean topography (DOT) from CryoSat-2 was downloaded from http://rads.tudelft.nl/rads/data/authentication.cgi

Level 3 v1.1 weekly SMOS ARCTIC sea surface salinity data were downloaded from SEANOE at https://www.seanoe.org/data/00607/71909/

Satellite SAR ice images and analysis were provided via special support from the U.S National Ice Center. RADARSAT-2 Data and Products are under a copyright of MDA Geospatial Services Inc. 2018 – All Rights Reserved, obtained via the U.S. National Ice Center. RADARSAT is an official mark of the Canadian Space Agency. Sentinel-1 data were obtained from the Copernicus Data Hub, supported by the European Space Agency.

9 References

Alkire, M.B., Jacobson, A., Macdonald, R.W., and Lehn, G. (2019). Assessing the contributions of atmospheric/meteoric water and sea ice meltwater and their influences on geochemical properties in estuaries of the Canadian Arctic Archipelago. *Estuaries and Coasts*, 42, 1226–1248. doi:10.1007/s12237-019-00562-w

Alory, G., Delcroix, T., Téchiné, P., Diverrès, D., Varillon, D., Cravatte, S., et al. (2015). The French contribution to the voluntary observing ships network of sea surface salinity. *Deep Sea Research I*, 105, 1–18. doi: 10.1016/j.dsr.2015.08.005

Antoine, D., Hooker, S. B., Bélanger, S., Matsuoka, A., and Babin, M. (2013). Apparent optical properties of the Canadian Beaufort Sea - Part 1: Observational overview and water column relationships. *Biogeosciences*, 10, 4493–4509, doi:10.5194/bg-10-4493-2013

Blanchard-Wrigglesworth, E., Armour K. C., Bitz C. M., and DeWeaver, E. (2011). Persistence and inherent predictability of Arctic sea ice in a GCM ensemble and observations. *Journal of Climate*, 24(1), 231–250. doi:10.1175/2010JCLI3775.1

Boccaletti, G., Ferrari, R., and Fox-Kemper, B. (2007). Mixed layer instabilities and restratification. *Journal of Physical Oceanography*, 37-9, 2228–2250. doi:10.1175/JPO3101.1

Brenner, S., Rainville, L., Thomson, J., Cole, S., and Lee, C. (2021). Comparing observations and parameterizations of ice-ocean drag through an annual cycle across the Beaufort Sea. *Journal of Geophysical Research: Oceans*, 126, e2020JC016977. doi:10.1029/2020JC016977

Brenner, S., Rainville, L., Thomson, J., and Lee, C. (2020). The evolution of a shallow front in the Arctic marginal ice zone. *Elementa: Science of the Anthropocene*, 8–17. doi:10.1525/elementa.413

Bushuk, M., Msadek, R., Winton, M., Vecchi, G., Yang, X., Rosati, A., and Gudgel, R. (2017). Regional Arctic sea-ice prediction: Potential versus operational seasonal forecast skill. *Climate Dynamics*, 1– 23. doi:10.1007/s00382-018-4288-y

Bushuk, M., Yang, X., Winton, M., Msadek, R., Harrison, M., Rosati, A., and Gudgel, R. (2019). The value of sustained ocean observations for sea ice predictions in the Barents Sea. *Journal of Climate*, 32(20), 7017–7035. doi:10.1175/JCLI-D-19-0179.1

Cole, S. T., Timmermans, M.-L., Toole, J. M., Krishfield, R. A., and Thwaites, F. T. (2014). Ekman veering, internal waves, and turbulence observed under arctic sea ice. *Journal of Physical Oceanography*, 44-5, 1306–1328. doi:10.1175/JPO-D-12-0191.1.t

Day, J. J., Tietsche, S., and Hawkins, E. (2014). Pan-Arctic and regional sea ice prediction: Initialisation month dependence. *Journal of Climate*, 27, 4371–4390. doi:10.1175/JCLI-D-13-00614.1

Dewey, S. R., Morison, J. H., and Zhang, J. (2017). An edge-referenced surface fresh layer in the Beaufort Sea seasonal ice zone. *Journal of Physical Oceanography*, 47-5, 1125–1144, doi:10.1175/JPO-D-16-0158.1

Fournier S., Lee T., Tang W., Steele M., and Olmedo E (2019). Evaluation and Intercomparison of SMOS, Aquarius, and SMAP Sea Surface Salinity Products in the Arctic Ocean. *Remote Sensing*. 11(24)–3043. doi:10.3390/rs11243043

Gade, H. G. (1979), Melting of ice in sea water: A primitive model with application to the Antarctic ice shelf and icebergs, *Journal of Physical Oceanography*, 9–1, 189–198. doi: 10.1175/1520-0485(1979)009<0189:MOIISW>2.0.CO;2

Graham, R. M., Cohen, L., Ritzhaupt, N., Segger, B., Graversen, R. G., Rinke, A., et al. (2019). Evaluation of six atmospheric reanalyses over Arctic sea ice from winter to early summer. *Journal of Climate*, 32(14), 4121–4143. doi:10.1175/JCLI-D-18-0643.1

Guemas, V., Blanchard-Wrigglesworth, E., Chevallier, M., Day, J.J., Déqué, M., Doblas-Reyes, et al. (2016). A review on Arctic sea-ice predictability and prediction on seasonal to decadal time-scales. *Quarterly Journal of the Royal Meteorological Society*, 142: 546-561. doi:10.1002/qj.2401

Hersbach, H., Bell, B., Berrisford, P., Biavati, G., Horányi, A., Muñoz Sabater, J., Nicolas, J., Peubey, C., Radu, R., Rozum, I., Schepers, D., Simmons, A., Soci, C., Dee, D., and Thépaut, J-N. (2018). ERA5 hourly data on single levels from 1979 to present [Dataset]. Copernicus Climate Change Service (C3S) Climate Data Store (CDS). (Accessed on 13 Jan 2021), doi:10.24381/cds.adbb2d47

Herraiz-Borreguero, L., I. Allison, M. Craven, K. W. Nicholls, and M. A. Rosenberg (2013). Ice shelf/ocean interactions under the Amery Ice Shelf: Seasonal variability and its effect on marine ice formation, *Journal of Geophysical Research–Oceans*, 118, 7117–7131, doi:10.1002/2013JC009158

Horvat, C., Tziperman, E., and Campin, J.-M. (2016). Interaction of sea ice floe size, ocean eddies, and sea ice melting. *Geophysical Research Letters*, 43, 8083–8090. doi:10.1002/2016GL069742

Islam, F., DeGrandpre, M. D., Beatty, C. M., Timmermans, M.-L., Krishfield, R. A., Toole, J. M., and Laney, S. R. (2017). Sea surface pCO_2 and O_2 dynamics in the partially ice-covered Arctic Ocean. *Journal of Geophysical Research: Oceans*, 122, 1425–1438. doi:10.1002/2016JC012162

Jackson, J. M., Carmack, E. C., McLaughlin, F. A., Allen, S. E., and Ingram, R. G. (2010). Identification, characterization, and change of the near-surface temperature maximum in the Canada Basin, 1993–2008. *Journal of Geophysical Research*, 115, C05021. doi:10.1029/2009JC005265

Jackson, J. M., Williams, W. J., and Carmack, E. C. (2012). Winter sea-ice melt in the Canada Basin, Arctic Ocean. *Geophysical Research Letters*, 39, L03603. doi:10.1029/2011GL050219

Johnson, M., and Eicken, H. (2016). Estimating Arctic sea-ice freeze-up and break-up from the satellite record: A comparison of different approaches in the Chukchi and Beaufort Seas. *Elementa: Science of the Anthropocene*, 4-000124. doi: 10.12952/journal.elementa.000124

Köhler, J., Sena Martins, M., Serra, N., and Stammer, D. (2015). Quality assessment of spaceborne sea surface salinity observations over the northern North Atlantic, *Journal of Geophysical Research: Oceans*, 120, 94– 112. doi:10.1002/2014JC010067

Kwok, R., Cunningham, G. F., LaBelle-Hamer, N. M., Holt, B., and Rothrock, D. (1999). Ice thickness derived from high-resolution radar imagery, *Eos Transactions American Geophysical Union* 80(42), 495–497. doi:10.1029/EO080i042p00495-01

Lee, C. M., Sylvia, C., Martin, D., James, M., Ruth, M., and Tom, P. (2016). Stratified Ocean Dynamics in the Arctic: Science and Experiment Plan. Technical Report APL-UW TR 1601. Seattle, WC: Applied Physical Laboratory, University of Washington, 46.

Leu, E., Mundy, C. J., Assmy, P., Campbell, K., Gabrielsen, T. M., Gosselin, M., Juul-Pedersen, T., and Gradinger, R. (2015). Arctic spring awakening—Steering principles behind the phenology of vernal ice algal blooms. *Progress in Oceanography*, 139, 151– 170. doi:10.1016/j.pocean.2015.07.012

Lu, K., Weingartner, T., Danielson, S., Winsor, P., Dobbins, E., Martini, K., and Statscewich, H. (2015). Lateral mixing across ice meltwater fronts of the Chukchi Sea shelf. *Geophysical Research Letters*, 42, 6754–6761. doi:10.1002/2015GL064967

Macdonald, R. W., Paton, D. W., Carmack, E. C., and Omstedt, A. (1995). The

freshwater budget and under-ice spreading of Mackenzie River water in the Canadian Beaufort Sea based on salinity and 18O/16O measurements in water and ice. *Journal of Geophysical Research*, 100(C1), 895–919, doi:10.1029/94JC02700

MacKinnon, J.A., Simmons, H.L., Hargrove, J., Thomson, J., Peacock, T., Alford, et al. (2021). A warm jet in a cold ocean. *Nature Communications* 12, 2418. doi:10.1038/s41467-021-22505-5

Manucharyan, G. E, and Thompson, A. F. (2017). Submesoscale sea ice-ocean interactions in marginal ice zones. *Journal of Geophysical Research: Oceans*, 122, 9455–9475. doi:10.1002/2017JC012895

Manucharyan, G. E., and Timmermans, M. L. (2013). Generation and separation of mesoscale eddies from surface ocean fronts. *Journal of Physical Oceanography*, 43–12, 2545–2562. doi:10.1175/JPO-D-13-094.1

Maykut, G. A. (1978). Energy exchange over young sea ice in the central Arctic. *Journal of Geophysical Research*, 83(C7), 3646– 3658, doi:10.1029/JC083iC07p03646

Mensa, J. A., Timmermans, M.-L., Kozlov, I. E., Williams, W. J., and Özgökmen, T. M. (2018). Surface drifter observations from the Arctic Ocean's Beaufort Sea: Evidence for submesoscale dynamics. *Journal of Geophysical Research: Oceans*, 123, 2635–2645. doi:10.1002/2017JC013728

Minnett, P. J., Alvera-Azcárate, A., Chin, T. M., Corlett, G. K., Gentemann, C. L., Karagali, I., et al. (2019). Half a century of satellite remote sensing of sea-surface temperature. *Remote Sensing of Environment*, 233, 111366. doi:10.1016/j.rse.2019.111366

Niemi, A., Michel, C., Hille, K., and Poulin, M. (2011). Protist assemblages in winter sea ice: setting the stage for the spring ice algal bloom. *Polar Biology*, 34, 1803–1817. doi:10.1007/s00300-011-1059-1

Peralta-Ferriz, C. and Woodgate, R. (2015). Seasonal and interannual variability of pan-Arctic surface mixed layer properties from 1979 to 2012 from hydrographic data, and the dominance of stratification for multiyear mixed layer depth shoaling. *Progress in Oceanography*, 134, 19–53. doi: 10.1016/j.pocean.2014.12.005

Paulson, C. A., and Simpson J. J. (1977). Irradiance measurements in the upper ocean. *Journal of Physical Oceanography*, 7, 952–956. doi:10.1175/1520-0485(1977)007<0952:IMITUO>2.0.CO;2

Price, J., Weller, R., and Pinkel, R. (1986). Diurnal cycling: Observations and models of the upper ocean response to diurnal heating, cooling and wind mixing. *Journal of Geophysical Research*, 91(C7), 8411–8427, doi:10.1029/JC091iC07p08411

Price, J., Weller, R., and Schudlich, R. (1987). Wind-Driven Ocean currents and Ekman transport. *Science*, 238-4833, 1534–1538. doi:10.1126/science.238.4833.1534

Rainville, L., Wilkinson, J., Durley, M. E., Harper, S., DiLeo, J., Doble, M., et al. (2020). Improving Situational Awareness in the Arctic Ocean. *Frontiers of Marine Sciences*. doi:10.3389/fmars.2020.581139

Randelhoff, A., Fer, I., and Sundfjord, A. (2017). Turbulent upper-ocean mixing affected by meltwater layers during Arctic summer. *Journal of Physical Oceanography*, 47–4, 835–853. doi:10.1175/JPO-D-16-0200.1

Scharroo, R., Leuliette, E. W., Lillibridge, J. L., Byrne, D., Naeije, M. C., and Mitchum, G. T. (2013). RADS: Consistent multi-mission products, in *Proceedings of the Symposium on 20 Years of Progress in Radar Altimetry*, Venice, 20-28 September 2012, European Space Agency Special Publication, ESA SP-710, p. 4 pp.

Sigmond, M., Reader, M. C., Flato, G. M., Merryfield, W. J, and Tivy, A. (2016). Skillful seasonal forecasts of Arctic sea ice retreat and advance dates in a dynamical forecast system. *Geophysical Research Letters*, 43, 12,457–12,465. doi:10.1002/2016GL071396

Smith, M., Stammerjohn, S., Persson, O., Rainville, L., Liu, G., Perrie, W., et al (2018). Episodic reversal of autumn ice advance caused by release of ocean heat in the Beaufort Sea. *Journal of Geophysical Research: Oceans*, 123, 3164– 3185. doi:10.1002/2018JC013764

Spreen, G., Kaleschke, L., and Heygster, G. (2008). Sea ice remote sensing using AMSR-E 89 GHz channels. *Journal of Geophysical Research*, 113, C02S03. doi:10.1029/2005JC003384

Steele, M., Ermold, W., and Zhang, J. (2011). Modeling the formation and fate of the near-surface temperature maximum in the Canadian Basin of the Arctic Ocean. *Journal of Geophysical Research*, 116, C11015, doi:10.1029/2010JC006803

Stroeve, J. C., Crawford, A. D., and Stammerjohn, S. (2016). Using timing of ice retreat to predict timing of fall freeze-up in the Arctic. *Geophysical Research Letters*, 43, 6332–6340. doi:10.1002/2016GL069314

Stroeve, J. C., Markus, T., Boisvert, L., Miller, J., and Barrett, A. (2014). Changes in

Arctic melt season and implications for sea ice loss. *Geophysical Research Letters*, 41,1216–1225. doi:10.1002/2013GL058951

Supply, A., Boutin, J., Vergely, J.-L., Kolodziejczyk, N., Reverdin, G., Reul, N., and Tarasenko, A. (2020a). SMOS ARCTIC SSS L3 maps produced by CATDS CEC LOCEAN. SEANOE. doi:10.17882/71909

Supply, A., Boutin, J., Vergely, J.-L., Kolodziejczyk, N., Reverdin, G., Reul, N., and Tarasenko, A. (2020b). New insights into SMOS sea surface salinity retrievals in the Arctic Ocean. *Remote Sensing of Environment*, 249, 112027 (24p.). doi:10.1016/j.rse.2020.112027

Tang, W., Yueh, S., Yang, D., Fore, A., Hayashi, A., Lee, T., et al. (2018). The Potential and Challenges of Using Soil Moisture Active Passive (SMAP) Sea Surface Salinity to Monitor Arctic Ocean Freshwater Changes. *Remote Sensing*.; 10(6):869. doi:10.3390/rs10060869

Thomson, J., Fan, Y., Stammerjohn, S., Stopa, J., Rogers, W. E., Girard-Ardhuin, F., et al. (2016), Emerging trends in the sea state of the Beaufort and Chukchi seas, *Ocean Modelling*, 105, 1–12. doi:10.1016/j.ocemod.2016.02.009

Thomas, L. N., Tandon, A., and Mahadevan, M. (2008). Submesoscale processes and dynamics. *Geophysical Monograph Series*, 177, 17–38. doi:10.1029/177GM04

Timmermans, M.-L. (2015). The impact of stored solar heat on Arctic sea ice growth. *Geophysical Research Letters*, 42, 6399–6406. doi:10.1002/2015GL064541

Timmermans, M.-L., Cole, S., and Toole, J. (2012). Horizontal density structure and restratification of the Arctic Ocean surface layer. *Journal of Physical Oceanography*, 42-4, 659–668. doi:10.1175/JPO-D-11-0125.1

Timmermans, M.-L., and Windsor, P. (2013). Scales of horizontal density structure in the Chukchi Sea surface layer. *Continental Shelf Research*, 52, 39–45. doi:10.1016/j.csr.2012.10.015

Toole, J. M., Timmermans, M.-L., Perovich, D. K., Krishfield, R. A., Proshutinsky, A., and Richter-Menge, J. A. (2010). Influences of the ocean surface mixed layer and thermohaline stratification on Arctic Sea ice in the central Canada Basin. *Journal of Geophysical Research*, 115, C10018. doi:10.1029/2009JC005660

Vallis, G. K. (2017). *Atmospheric and Oceanic Fluid Dynamics: Fundamentals and Large-Scale Circulation.* Second edition. Cambridge University Press.

von Appen W.-J., Wekerle, C., Hehemann, L., Schourup-Kristensen, V., Konrad, C., and Iversen, M. H. (2018). Observations of a submesoscale cyclonic filament in

the marginal ice zone. *Geophysical Research Letters*, 45, 6141–6149. doi:10.1029/2018GL077897

Wadhams, P. (2000). *Ice in the Ocean.* Overseas Publishers Association.

Wilson, E. A., Riser, S. C., Campbell, E. C., and Wong, A. P. S. (2019). Winter upper-ocean stability and ice-ocean feedbacks in the sea ice-covered Southern Ocean. *Journal of Physical Oceanography,* 49–4, 1099–1117. doi:10.1175/JPO-D-18-0184.1

10 Figures

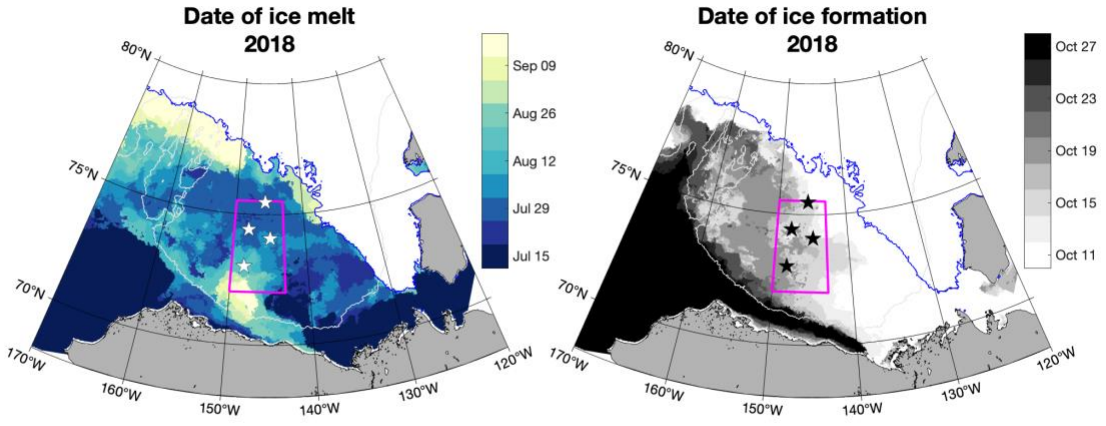

Figure 2.1 Spatial variability of (left) melt out and (right) freeze up dates in the Beaufort Sea in 2018. Ice retreat was defined as the first day AMSR2 ice concentration fell below 0.15 for five consecutive days and freeze up was defined as the first day AMSR2 ice concentration exceeded 0.15 for five consecutive days. Ice never retreated in the area bounded by the blue contour. Solid gray regions delineate landmasses, light gray contours mark the 1000-m isobath, and white stars indicate mooring locations. The pink box marks the region depicted in Figure 2.2.

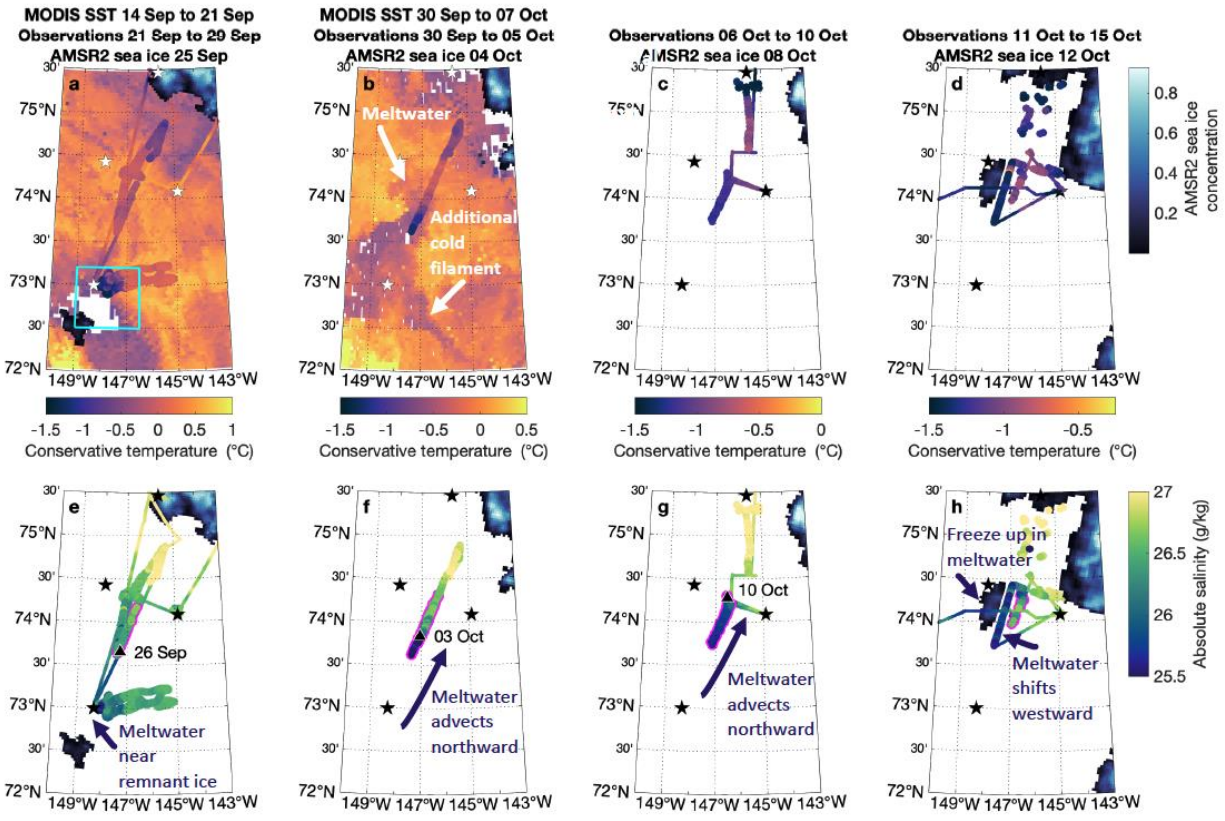

Figure 2.2 Upper ocean observations and remote sensing show the meltwater's advection in the weeks preceding freeze up. (a–d) Conservative temperature and (e–h) absolute salinity observations, including Seaglider and uCTD data averaged in the upper 5 m as well as Wave Glider data at 5 m or 9 m (large scatter points) and Healy underway data at 2.7 m (thin line), at the time periods specified in the column titles. MODIS-Terra SST is included in the first two panels and the AMSR2 ice concentration is shown where it exceeded zero. The black triangles are the locations of the 26 g/kg isohaline outcrop, a proxy for the edge of the meltwater. Seaglider profiles outlined in pink were used in the mixed layer heat budget developed in Chapter 2.4. Stars indicate mooring locations.

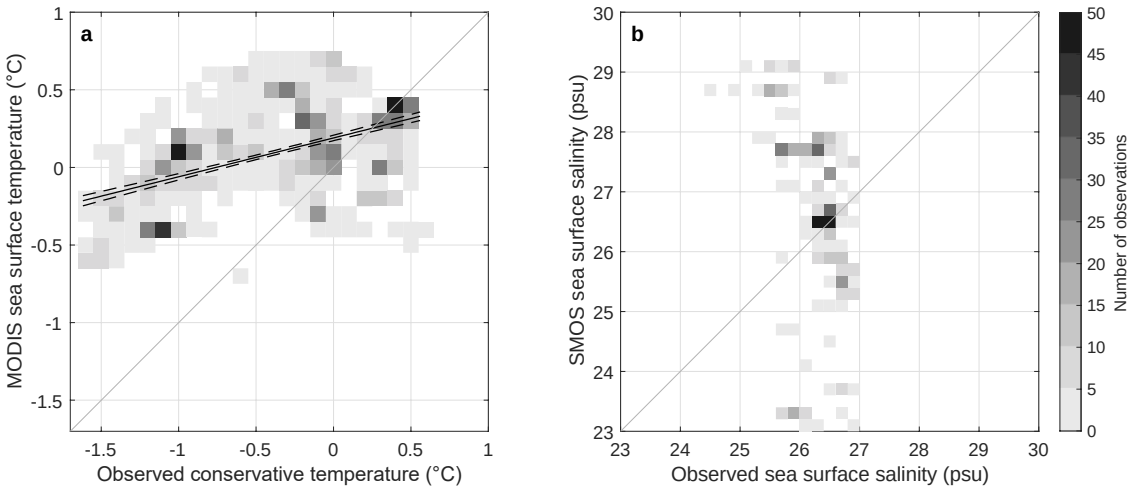

Figure 2.3 Two-dimensional histograms comparing (a) conservative temperature and (b) practical salinity from Seagliders, Wave Gliders, uCTD, and the Healy underway system ("observed") to concurrent satellite data. Satellite data was from (a) daily MODIS-Terra and (b) weekly SMOS ARCTIC (Supply et al., 2020a). The solid line in (a) is the linear regression and the dashed lines are the 95% confidence bounds.

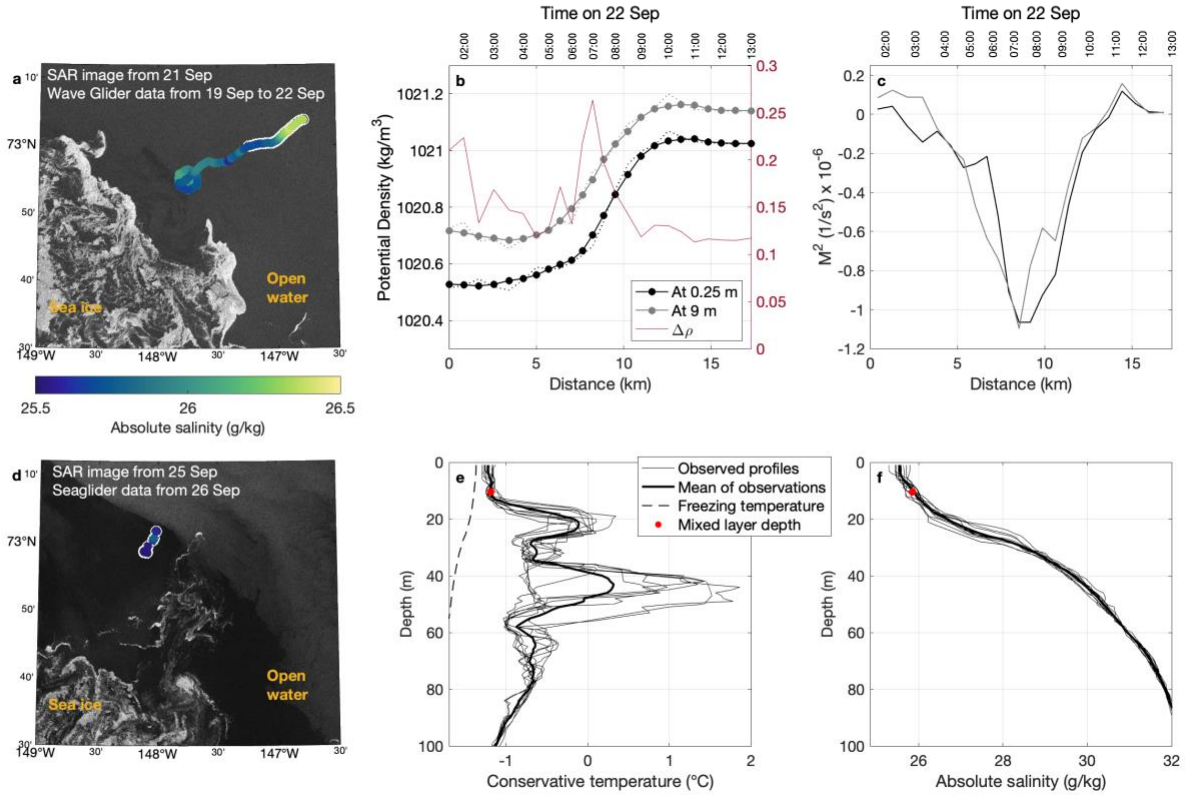

Figure 2.4 Meltwater conditions near the remnant sea ice. (a) Wave Glider salinity at 0.25 m and sea ice from SAR on 21 September in the cyan box in Figure 2.2, with data from the white-outlined track shown in (b) and (c). (b) Wave Glider potential density at 0.25 m (black lines) and 9 m (gray lines) including the raw data (dotted lines) and data smoothed with a moving mean with a window width of approximately 4 km (solid lines). The density difference between the shallow and deep measurements is shown in red. (c) Along-track horizontal buoyancy gradient M^2 calculated from the smoothed density. (d) Seaglider absolute salinity averaged in the upper 5 m and sea ice from SAR on 25 September. (e-f) Seaglider profiles, including the average profiles (bold lines) of (e) conservative temperature and (f) absolute salinity. The red dots show the mixed layer depth, defined as a density change of 0.25 kg m^{-3} relative to the surface.

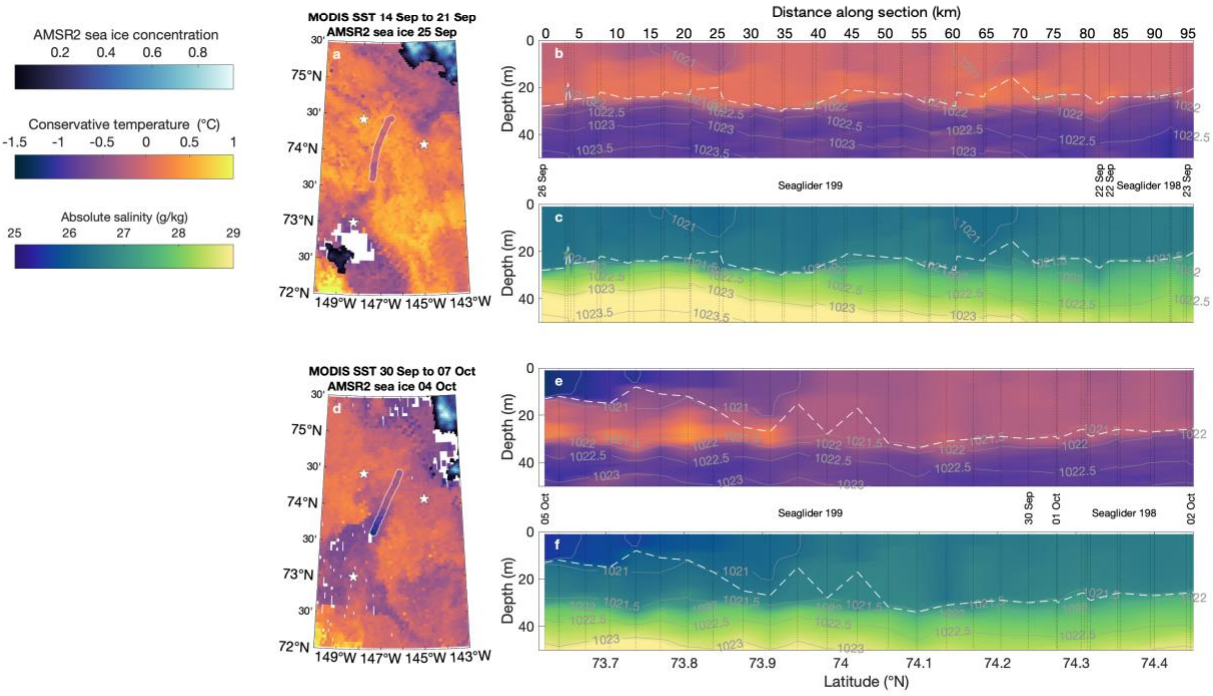

Figure 2.5 Conservative temperature and absolute salinity in latitude-depth sections measured by two Seagliders from (a–c) 22–26 September and (d–f) 30 September to 5 October. Panels a and d show profile locations as white outlined dots, with dot color indicating observed conservative temperature averaged in the upper 5 m. Stars indicate mooring locations. Sampling began partway through the transect with one Seaglider sampling outward in each direction, indicated by the dates. The gray lines on the section plots mark potential density contours at 0.25 kg m^{-3} intervals and the dashed white lines mark mixed layer depth defined as a density difference of 0.25 kg m^{-3} relative to the surface. Sections show only the upper 50 m of the 1000-m profiles, with vertical lines indicating individual profiles.

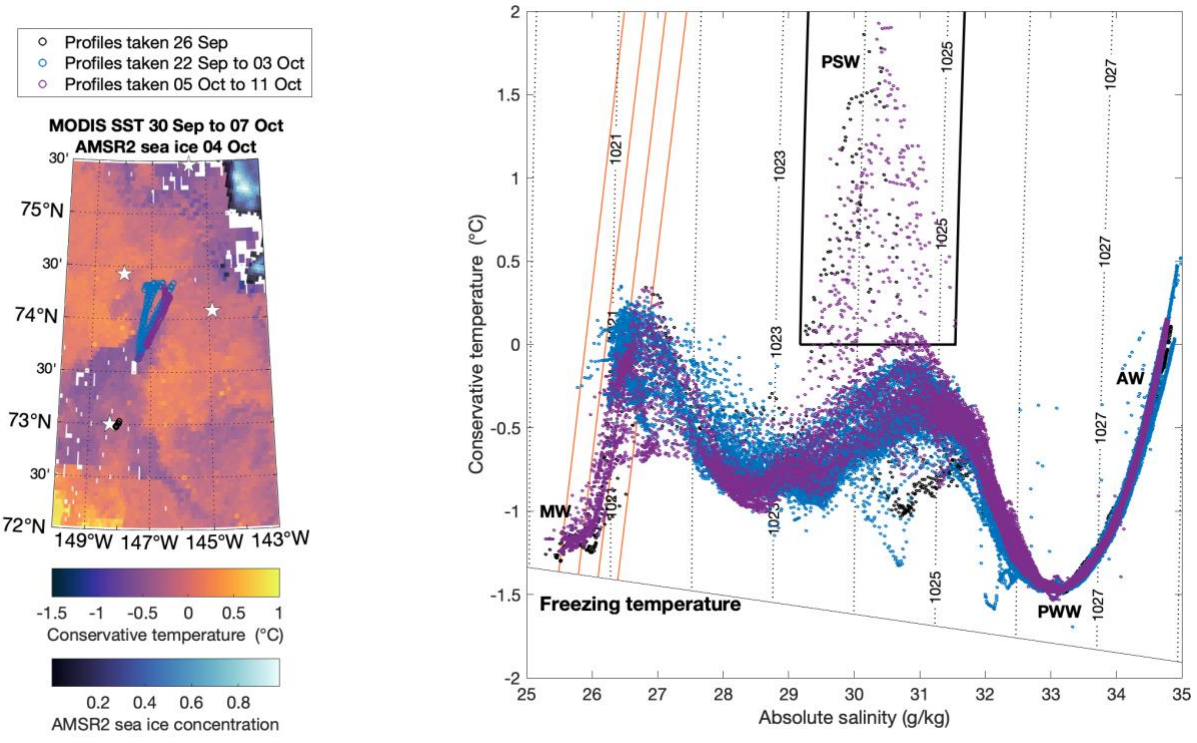

Figure 2.6 Conservative temperature and absolute salinity in the remnant ice area (black) and farther north before (blue) and after (purple) the meltwater arrived. (left) Colored dots show profile locations and white stars show mooring locations. (right) Seaglider profiles from 0–1000 m along with potential density contours (black dotted lines) and Gade Lines (orange solid lines). The freezing temperature at the surface is indicated. MW = meltwater, PSW = Pacific Summer Water, PWW = Pacific Winter Water, AW = Atlantic Water. The black box defines PSW.

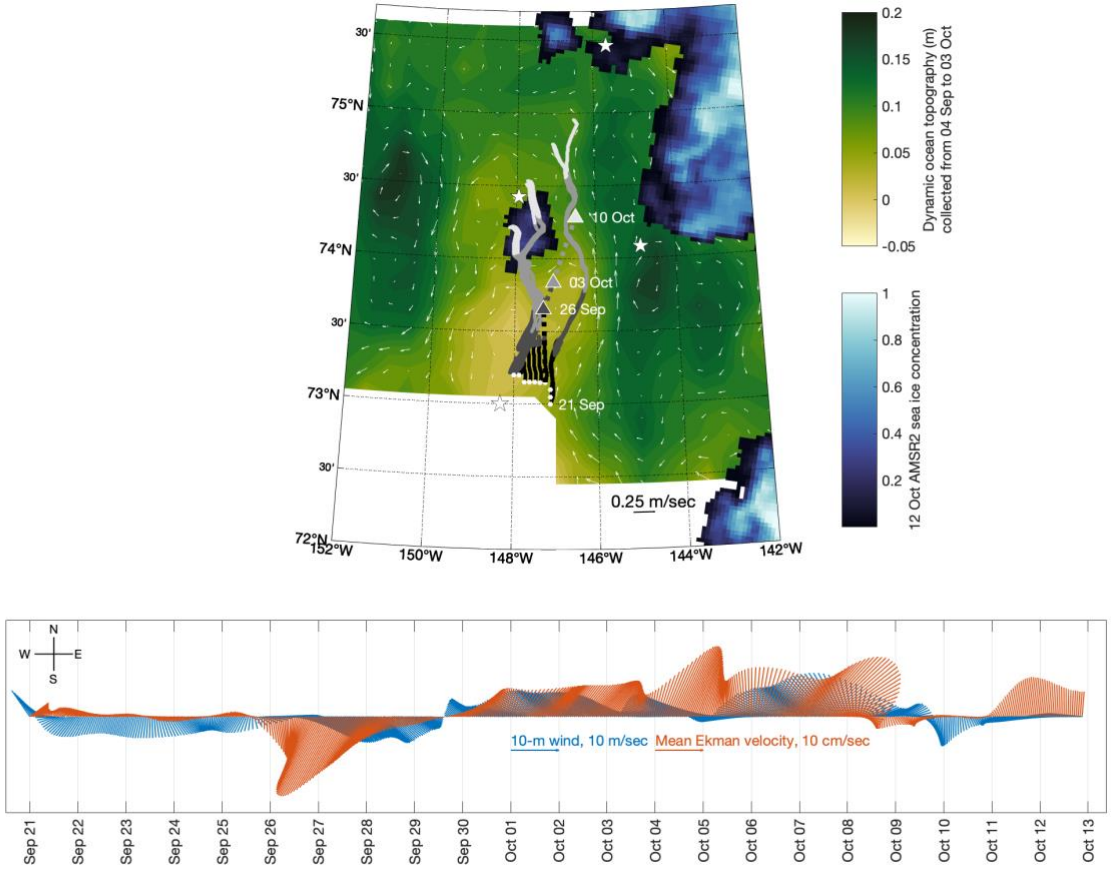

Figure 2.7 Simulated advection trajectories driven by geostrophic and Ekman velocities compared to the observed meltwater advection. (top) Dynamic ocean topography (background colors) and surface geostrophic velocity (white arrows) along with the simulated trajectories advected by the combined geostrophic and Ekman velocities from 21 September (white dots) to 15 October (ends of solid tracks). The locations of the advected tracks at key times (track color changes) correspond to the times of the observed locations of the 26 g/kg isohaline outcrop (colored triangles), which are connected to illustrate the inferred advection path (dotted line). Stars indicate mooring locations. (bottom) ERA5 10-m wind and associated Ekman velocities averaged in the region bounded by 145°W to 149°W, 73°N to 74.5°N. The length of the lines show the speed, with scaling lines shown below the time series. The direction of the lines show the cardinal direction of the velocity, with a compass rose provided for reference.

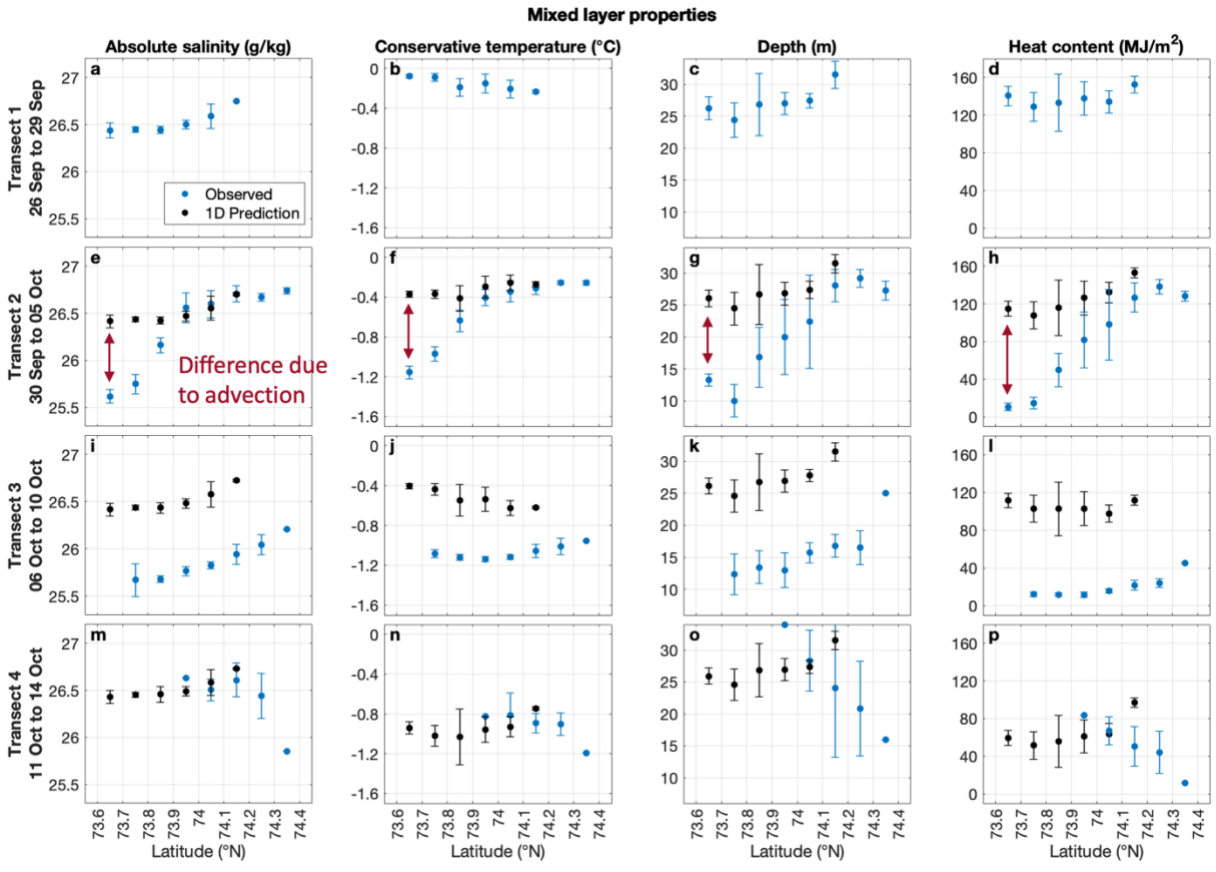

Figure 2.8 Differences between observations and model predictions demonstrate that advection altered mixed layer properties. Observed (blue) and concurrent PWP model-predicted (black) mixed layer properties binned by latitude and averaged. Observation locations are shown in Figure 2.2e–h. Each row shows mixed layer properties on the transect labeled to the left while each column shows the property labeled at the top. Meltwater presence can be inferred from observed absolute salinities below 26 g/kg. There are no model predictions for Transect 1 as these profiles were used to initiate the model. The error bars show one standard deviation.

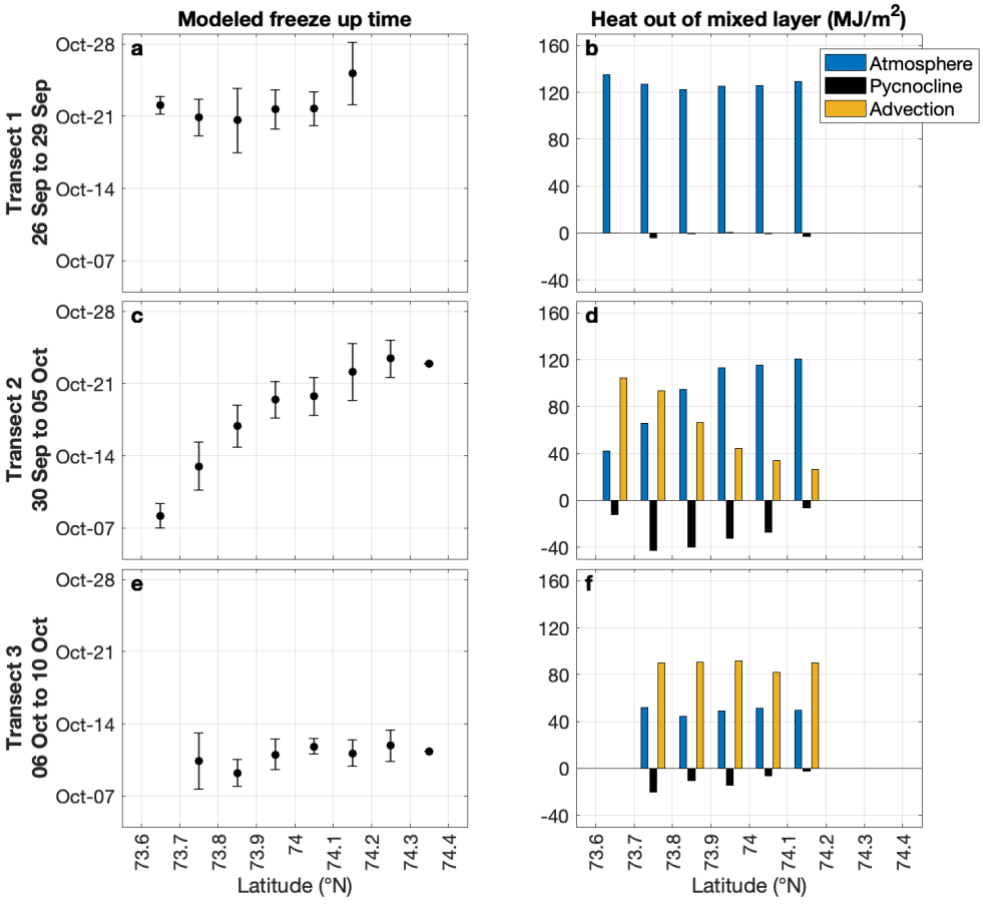

Figure 2.9 Freeze up times and mixed layer heat budgets varied with the presence or absence of meltwater. Observation locations are shown in Figure 2.2e–h. (Panels a,c,e) PWP model predicted freeze up binned and averaged by latitude. The error bars are one standard deviation. (Panels b,d,f) Heat budget components for each latitude bin on each transect.

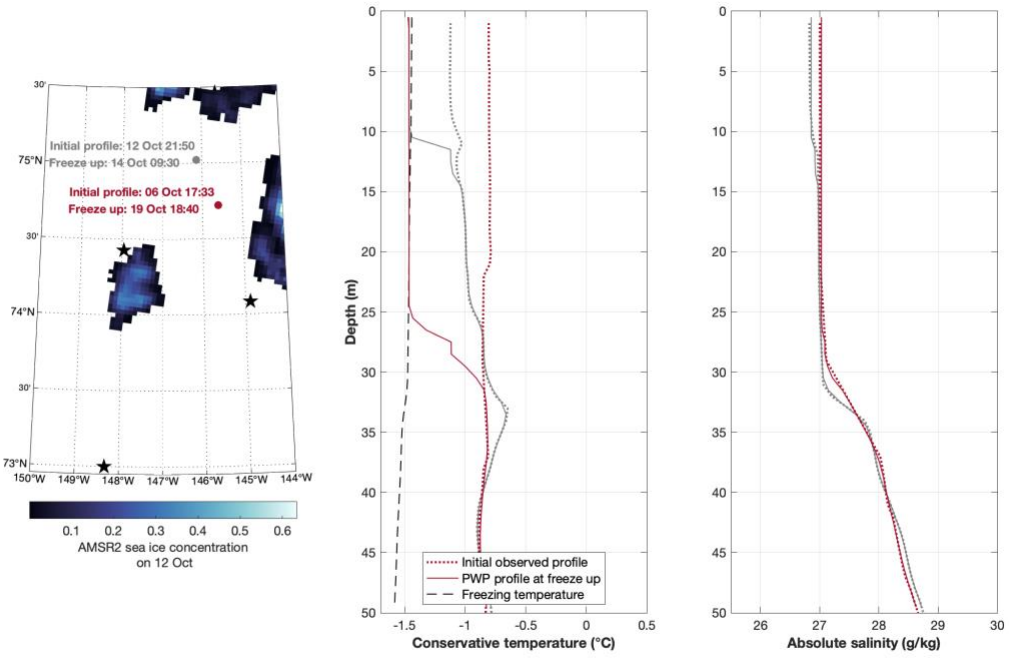

Figure 2.10 Surface freshening near the northern MIZ restricted cooling to a shallower layer and resulted in earlier modeled freeze up. (left) Locations of example observed profiles used to initiate the PWP model along with AMSR2 ice concentration where it exceeded zero. Stars indicate mooring locations. (right) Observed conservative temperature and absolute salinity profiles (dotted lines) and modeled profiles at freeze up (solid lines). The profile colors correspond to the colored observation locations and times shown on the map.

Chapter 3 Stronger ice and ocean inertial oscillations follow a winter lead opening event

Abstract

Ocean mixed layer inertial oscillations are energetic currents that link energy input by the wind to ocean mixing and dissipation. Sea ice properties and dynamics play a central role in atmosphere-ocean momentum transfer in polar regions, and sea ice changes are altering many aspects of the Arctic system, including ocean near-inertial currents. This study uses moored velocity observations and remote sensing collected during a February 2019 storm in the Beaufort Sea to demonstrate how sea ice and mixed layer inertial oscillations developed following a lead opening event, whereas an unfractured ice pack selectively filtered out near-inertial motions. At the northern mooring site, which experienced minimal lead opening, internal ice stresses reduced inertial oscillation strength by 82% relative to a slab model driven by the surface forcing. At the southern mooring site, in contrast, a lead opening event proceeded the development of inertial oscillations that were minimally damped by ice. Our results suggest that near-inertial motion predictions in consolidated ice packs should account for the lateral scales of ice fracturing and cannot rely on free-drift proxies like ice concentration and wind factor. While inertial oscillations in the ice-free ocean are locally driven, this study connects the local inertial response to regional ice dynamics, including the ice pack's interaction with the distant coast.

1 Introduction

In polar regions, sea ice is fundamental to momentum transfer between the

atmosphere and the ocean (e.g., McPhee 2012). The mechanical ice-ice interactions that comprise internal ice stresses, such as crushing during floe collisions, can interrupt this momentum transfer. Local internal stresses are not simply due to local ice deformation; instead, consolidated ice can transfer internal stresses from ice-coast interactions hundreds of kilometers into the ice pack (Richter-Menge et al., 2002) decreasing ice mobility and generating long and narrow cracks known as leads (e.g., Lewis and Hutchings 2019; Jewell et al., 2023).

Fluctuating wind stresses excite energetic currents in the ocean surface layer that oscillate at frequencies near the local inertial frequency f (Pollard and Millard 1970). These inertial oscillations can be strong enough to initiate shear-driven mixing and pycnocline entrainment at the mixed layer base (Plueddemann and Farrar 2006), and may propagate into the pycnocline as near-inertial internal waves (D'Asaro 1989). Accurately predicting or modeling near-inertial energy input to the ocean mixed layer is an essential step toward understanding mixed layer dynamics as well as deep ocean circulation, stratification, and mixing (e.g., Alford 2001; Wunsch and Ferrari 2004).

While simple models adequately describe the ice-free ocean's response to surface wind stress (Pollard and Millard 1970; D'Asaro 1985), sea ice complicates this response. The sea ice and the ocean mixed layer can undergo tightly coupled inertial oscillations (Brenner et al., 2023a; McPhee 1978), but these oscillations are generally weaker during ice-covered periods than during open-water periods. This seasonality has often been attributed to damping by a strong and consolidated ice pack in which internal stresses are important (Kawaguchi et al., 2019; Martini et al., 2014; Rainville

and Woodgate 2009; Gimbert et al., 2012b) but seasonal changes in mixed layer depth also may contribute (Brenner et al., 2023a).

Deviations from this ice-influenced inertial oscillation seasonality represent opportunities to explore how changes in ice dynamics or characteristics impact near-inertial motions. For example, despite high ice concentrations, the most energetic ocean inertial oscillation event observed throughout a year-long mooring deployment on the Beaufort slope occurred in December (Martini et al., 2014). This event was "preconditioned" by another wind event several days earlier that "loosen[ed]" the ice pack (Martini et al., 2014), demonstrating that strong and episodic near-inertial motions can be generated in winter if conditions are favorable. This intriguing observation suggests that a more mechanistic understanding of how sea ice dynamics and characteristics impact ocean near-inertial energy will be needed to predict how this energy will respond to future conditions.

The Arctic has undergone considerable changes in sea ice extent, thickness, and drift speed in recent decades (Comiso et al., 2008; Kwok and Rothrock 2009; Rampal et al., 2009; Rothrock et al., 2008) with concomitant changes in broadband momentum transfer across the air-ice-ocean interface (Brenner et al., 2021) and faster sea ice inertial oscillations (Gimbert et al., 2012b). It has been hypothesized that Arctic sea ice loss could increase near-inertial internal wave energy and mixing by enhancing atmosphere-ocean momentum transfer through a weaker and more mobile ice pack (e.g., Fine and Cole 2022). Thus far, however, the impact of sea ice on ocean near-inertial energy remains equivocal.

In the mixed layer, thinning and weakening ice could upend the historical paradigm of inertial oscillation damping. Idealized slab model experiments suggest that relative to open-ocean conditions, sea ice can actually *increase* inertial oscillation amplitude when internal ice stresses are weak (Brenner et al., 2023a). This intensification arises because the rough topside of the ice relative to open water increases the efficiency of momentum transfer from the atmosphere (Brenner et al., 2023a; Martin et al., 2014). These conflicting effects of sea ice on the ocean mixed layer's inertial response (observed inhibition by internal ice stresses, modeled amplification by air-ice drag) indicate that improved physical understanding is needed of the role sea ice plays in modifying inertial oscillation generation.

In the pycnocline, early studies found that near-inertial internal wave energy was far below midlatitude levels (D'Asaro and Morehead 1991; Levine et al., 1987). More recent studies have not found an interannual trend in internal wave energy or parameterized mixing in observational data collected over the last several decades (Dosser et al., 2021; Guthrie et al., 2013), and internal wave-driven dissipation in winter has declined in the Canada Basin (Dosser et al., 2021). This wintertime decline, which contradicts the prediction that weaker ice would enhance internal wave-driven mixing, may be due to decreases in rough multiyear ice floes (Dosser et al., 2021) as rougher ice increased observed internal wave generation at high ice concentrations (Cole et al., 2018). Again, these varying results suggest that our physical understanding of near-inertial motions in ice-covered waters remains incomplete.

Recent observations showed that ice dynamics strongly decreased the ocean's

inertial response in the northern Beaufort Sea but had a modest impact in the southern Beaufort Sea (Brenner et al., 2023a). In this paper we leverage the presence of this gradient to examine how sea ice mobility and dynamics impacted inertial oscillation development during an Arctic storm in February 2019. Focusing our study on an individual storm allows a detailed analysis of ice and ocean observations from a moored array that spanned nearly 600 km of the Beaufort Sea and provided measurements of contrasting sea ice conditions. Our results demonstrate how air-ice-ocean interactions across a wide range of interacting spatial and temporal scales, including the ice pack's interaction with the distant coast, impacted near-inertial energy input to the mixed layer.

This Chapter is structured as follows. Chapter 3.2 describes the mooring observations and an ice-ocean slab model used to interpret the observations. Chapter 3.3 describes the evolution of the coupled atmosphere-ice-ocean system during a winter storm with a particular focus on near-inertial frequency motions of the ice and ocean mixed layer. Chapter 3.4 and Chapter 3.5 discuss and summarize these results.

2 Methods

2.1 Overview

This paper uses data collected by an array of three moorings deployed in the Beaufort Sea's deep Canada Basin from autumn 2018 to autumn 2019 as part of the Stratified Ocean Dynamics of the Arctic (SODA) experiment (Lee et al., 2016; Rainville et al., 2020). These moorings were oriented roughly south to north and are referred to as SODA–A, SODA–B, and SODA–C (Figure 3.1a). The array spanned a

wide range of sea ice conditions, from weak and seasonal ice at the southern site to strong, year-round ice cover at the northern site (Brenner et al., 2023a). Each mooring was equipped with three acoustic Doppler current profilers (ADCPs) and numerous temperature and salinity sensors in the mixed layer and upper pycnocline. Some of these data were previously presented in a series of papers that developed higher-level products, including observations of sea ice geometry and the ice-ocean drag coefficient (Brenner et al., 2021), time series of mixed layer depth (Brenner et al., 2023b), and an idealized ice-ocean slab model that can be used to explore near-inertial motions generated by surface forcing (Brenner et al., 2023a).

In addition to contrasting observed inertial motions across the mooring array, we also compare observed velocities to those predicted by a slab model with no internal ice stresses. The slab model is useful in this context because it simulates the storm's *potential* to generate inertial oscillations at each mooring in the absence of internal ice stresses. Thus, the model helps elucidate the impact of regional differences in ice dynamics on the observed response by controlling for regional differences in wind forcing and mixed layer depth, which also impact the observed response.

2.2 Moored ADCP measurements

Data from two ADCPs at each mooring are used in this paper. First, each mooring had an upward-looking 5-beam Nortek Signature-500 ADCP surveying ice and ocean velocities along with sea ice draft (using the instrument's fifth beam as an altimeter). These ADCPs were located at 45 m for SODA–A, 42 m for SODA–B, and 27 m for SODA–C. See Brenner et al. (2021) for a description of Signature-500 ADCP

processing. Second, upward-looking Teledyne Workhorse-300 ADCPs were located approximately 45 m below the Signature-500 ADCPs. There was some overlap in the vertical range measured by both ADCPs. This overlap was used to calibrate the Workhorse-300 compasses from the Signature-500 stored magnetometer data (see Brenner 2022, Chapter 2.3.1). Data from both ADCPs were then combined to create ocean velocity profiles spanning the upper ~80 m of the water column in 2-m vertical bins at hourly temporal resolution (see Brenner 2022, Chapter 2.3.2). Data from the uppermost 6 m of the water column were discarded due to sidelobe reflections.

2.3 WKB scaling

Propagating internal waves are refracted by varying stratification, altering wave amplitude and wavenumber. If changes in stratification are small compared to the vertical scale of the waves, Wentzel-Kramers-Brillouin (WKB) scaling, a technique used to account for this refraction, can be used to compare data at different depths as if stratification were constant (Leaman and Sanford 1975). Though this paper primarily considers mixed layer near-inertial motions, wave propagation in the pycnocline is also of interest. WKB-scaled complex velocities U_n were calculated from observed pycnocline velocities U_n using:

$$U_n = \frac{U}{\sqrt{N(z)/N_0}} \tag{3.1}$$

Stretched depth coordinates z' were calculated by integrating the stratification scaling factor from the deepest mixed layer depth observed at each mooring during the study period:

$$z' = \int_{MLD_{max}}^{z} N(z)/N_0 \; dz \qquad 3.2$$

Stratification *N* was from CTD casts collected when moorings were deployed in the autumn. As stratification below the winter mixed layer varies at interannual timescales, we assume these observed stratification values are representative of pycnocline stratification throughout the mooring deployments. N_0 was the average stratification between the deepest mixed layer depth and 100 m. Stretched and unstretched depths were equal above the deepest observed mixed layer depth, but velocity scaling (Equation 3.2) was applied below the time-varying observed mixed layer depth.

2.4 Remote sensing and reanalysis

Several remote sensing and reanalysis products provided context about regional atmospheric and sea ice conditions to aid in interpretation of the mooring observations. Because of the overlying ice, the moorings did not observe meteorological variables, so surface air pressure and 10-m wind from ERA5 (Hersbach et al., 2023) were used to understand the storm's structure and to force the slab model. ERA5 data were downloaded at 0.25° horizontal resolution and hourly temporal resolution. NSIDC's Polar Pathfinder product (Tschudi et al., 2019) provided regional sea ice motion at 25-km horizontal resolution and daily temporal resolution. Moderate Resolution Imaging Spectroradiometer (MODIS) Level-1B brightness temperature at 1-km horizontal resolution (MODIS Characterization Support Team 2017) was used to visualize sea ice lead formation and evolution. Multiple MODIS images per day were available in our study region though clouds limited the usefulness of some images.

Daily maps of sea ice leads at 1-km horizontal resolution (Willmes and Heinemann 2016; Reiser et al., 2020) were used to calculate the lead fraction (the lead area divided by the total ice and lead area in a given region; Willmes et al., 2023) in the vicinity of the moorings. Daily passive microwave sea ice concentration from AMSR2 at 3.125-km horizontal resolution (Spreen et al., 2008) was assessed as a potential proxy for the importance of ice dynamics in inertial oscillation damping.

2.5 Coupled ice-ocean slab model

2.5.1 Model Overview

The ocean's response to wind forcing, including Ekman transport and inertial oscillations, can be modeled as a "slab" in which the wind stress is distributed uniformly throughout the mixed layer as a body force (Pollard and Millard 1970). These slab model formulations typically include a linear damping term to simulate inertial oscillation decay due to internal wave radiation, mixing, or turbulent dissipation (e.g., D'Asaro 1985; Pollard and Millard 1970). We use a one-dimensional coupled ice-ocean slab model to explore the ice and ocean response to wind forcing. This model formulation was developed by Brenner et al. (2023a) and is similar to the model developed by Gimbert et al. (2012a). We adopt D'Asaro (1985)'s notation for the complex velocities $Z = u + iv$ and stresses $T = (\tau_x + i\tau_y)/\rho_o$. Briefly, the ice and ocean momentum equations are coupled by the ice-ocean stress and modeled as:

$$\frac{dZ_i}{dt} + ifZ_i = \frac{T_{ai} - T_{io}}{d} - r_i Z_i \text{ , and} \quad 3.3$$

$$\frac{dZ_o}{dt} + ifZ_o = \frac{T_S}{H-d} - r_o Z_o, \quad 3.4$$

where d is the sea ice draft, H is the mixed layer depth, and r_i and r_o are damping coefficients approximating internal ice stresses and stress at the mixed layer base, respectively. The subscripts $(\,)_i$ and $(\,)_o$ indicate ice or ocean. The ocean velocity Z_o is vertically averaged in the mixed layer. The air-ocean, air-ice, and ice-ocean stresses were calculated using quadratic drag laws as

$$T_{ao} = \left(\frac{\rho_a}{\rho_o}\right) C_{ao} Z_a |Z_a|, \quad 3.5$$

$$T_{ai} = \left(\frac{\rho_a}{\rho_o}\right) C_{ai} Z_a |Z_a|, \text{ and} \quad 3.6$$

$$T_{io} = C_{io}(Z_i - Z_o)|Z_i - Z_o|, \quad 3.7$$

with ρ_a the density of air, C_{ao} the atmosphere-ocean drag coefficient, C_{ai} the atmosphere-ice drag coefficient, and C_{io} the ice-ocean drag coefficient. As the wind speed is typically much larger than the ice or ocean speed, the velocity of the underlying (ice or ocean) surface was neglected in Equations 3.5 and 3.6, but the ice-ocean relative velocity was used to calculate the ice-ocean stress (Equation 3.7). The total ocean surface stress T_S in mixed sea ice and open water conditions was calculated by scaling T_{ao} and T_{io} by ice fraction A

$$T_S = AT_{io} + (1 - A)T_{ao}. \quad 3.8$$

2.5.2 Model implementation

Equations 3.3 and 3.4 were solved using ode15s, MATLAB's variable order

initial value problem solver for stiff ODEs, which uses adaptive time stepping for computational efficiency. The ice and ocean were initially at rest, and the model was spun up for several days before the period of interest. The observed hourly ice draft was from ADCP measurements (Brenner et al., 2021) and the observed daily mixed layer depth was derived from ADCP backscatter and near-inertial shear (Brenner et al., 2023b). Following Brenner et al. (2023a), a minimum sea ice draft of 0.10 m was imposed to stabilize Equation 3.3. Time-varying wind forcing $Z_a = u_{10\,m} + i\,v_{10\,m}$ and sea ice concentration A from ERA5 at hourly temporal resolution and 0.25° horizontal resolution were averaged in a 30 km radius of each mooring, consistent with Brenner et al. (2021) and Brenner et al. (2023a). The time-varying drag coefficients were calculated as follows: C_{ao} varied with wind speed following Large and Yeager (2004), C_{ai} varied with ice concentration following Hersbach et al. (2023) with maximum values at intermediate ice concentrations, and C_{io} was calculated weekly using a force-balance approach and observed ice and ocean velocities (Brenner et al., 2021).

The tunable ice and ocean decay constants r_i and r_o approximate damping by internal ice stresses and internal wave radiation, respectively. Brenner et al. (2023a) chose r_i and r_o to maximize model fit to observed ice and ocean velocities, allowing r_i to vary with ice thickness and concentration. Our use of the slab model is motivated by a somewhat different experimental philosophy. Here, we compare observed velocities, which are influenced by internal stresses, to modeled velocities for a stress-free ice pack, assuming that differences between observed and modeled velocities can be attributed primarily to the unmodeled internal stresses. Thus, we use $r_i = 0$ to simulate

an ice pack in free drift (i.e., with negligible internal ice stress divergence). The time invariant ocean damping coefficient r_o was determined for each mooring by minimizing the RMSE between the observed and modeled mixed layer near-inertial velocities when $A<0.85$ (i.e., periods of the year-long mooring deployments when internal ice stresses were likely small, so using $r_i = 0$ in the fit was realistic). The calculated r_o values were $0.03f$ at SODA–A, $0.015f$ at SODA–B, and $0.025f$ at SODA–C, comparable to the Beaufort Sea value of $0.05f$ found by Fine et al. (2021) but significantly smaller than the commonly-used mid-latitude value of $0.15f$ (Alford 2001).

2.6 Near-inertial filtering and frequency determination

The near-inertial frequency band was defined as horizontal velocities with frequency magnitude between 0.9-1.1f. At the latitudes of our study, this frequency band also includes semidiurnal tides, so barotropic tidal velocities from the Arc5km2018 tidal model (Erofeeva and Egbert 2020) were subtracted from the observed ice and ocean velocities prior to near-inertial filtering. Tides are weak in this region; SODA–C had the strongest tides with maximum speeds of 0.005 m s^{-1}. Following de-tiding, near-inertial velocities were extracted from mooring observations and slab model results by bandpass filtering with a fourth-order low-pass Butterworth filter that permitted frequencies from 0.9-1.1f.

The frequency ω of the observed or slab modeled near-inertial response was determined by minimizing the difference between the observed or slab modeled velocity and a fitted sine wave with a prescribed test frequency and optimized amplitude and phase. This approach was preferred to identifying a spectral peak because the time

periods of interest were relatively short so spectra computed from the hourly velocity data were not well resolved. The test ω values were fit to velocity data in a four-day window beginning on 25 February as this time period captures the near-inertial response to the storm considered in this study. The eastward and northward components of velocity were fit separately. The best-fit ω values are reported as frequency ranges for which R^2 between the observed or slab modeled velocity and fitted velocity exceeded 0.95 for both the eastward and northward components of velocity. While the frequency yielding the best fit depended somewhat on the temporal window of observed or slab modelled velocity used for fitting, the conclusions are not sensitive to shrinking, expanding, or shifting the temporal window as long as the focus remains on the storm response period.

3 Results

3.1 Results overview

This paper examines the evolution of the atmosphere, sea ice, and ocean before, during, and after a storm in the central Beaufort Sea in February 2019. This series of events can be divided into three phases: sea ice lead formation (Chapter 3.3.2), storm passage (Chapter 3.3.3), and the observed inertial response (Chapter 3.3.4). Prior to the storm, from 22–23 February, winds pushed the ice pack against the Canadian Arctic Archipelago and the Canadian and Alaskan mainland east of Point Barrow (Figure 3.1a), opening a network of leads that traversed some of the study area (Figure 3.1c-d). Following lead formation, from 24–26 February, a low pressure system brought strong (up to 16 m s^{-1}), clockwise-rotating winds to the region (Figure 3.1b, Figure 3.2a). This

storm excited sea ice and ocean mixed layer inertial oscillations whose magnitudes peaked between 26–28 February (Figure 3.3e, Figure 3.4e, Figure 3.5e). The observed ice and ocean near-inertial velocities varied in accord with the history of lead activity, with stronger inertial oscillations found at the fractured sites. In contrast to the differing near-inertial responses, the storm caused comparable low-frequency ice motion at the southern (SODA–A) and northern (SODA–C) moorings.

3.2 22–23 February: Sea ice lead formation

High atmospheric pressure moved eastward along the northern Alaskan coast on 22 February 2019. Anticyclonic winds compacted ice against the coastline (Figure 3.1a) and leads opened in the ice pack. One lead system extended from Point Barrow northward toward SODA–A and a second lead system extended westward from Banks Island toward SODA–B (Figure 3.1c). These topographic points are known hotspots for lead initiation (Reiser et al., 2020, their Figure 10), with similar wind conditions favoring lead formation across the Beaufort Sea (Jewell and Hutchings 2023; Jewell et al., 2023). On 22 February the lead fraction increased to 35% in 200 km × 200 km regions around SODA–A and SODA–B but remained below 5% in a 200 km × 200 km region around SODA–C (Figure 3.1d, Figure 3.2b). AMSR2 ice concentration (Spreen et al., 2008) averaged in the same 200 km × 200 km regions remained above 90% at all mooring sites throughout the study period.

Subsequent MODIS imagery revealed anticyclonic ice motion and additional ice fracturing from coastal promontories between these bounding leads. This behavior suggests the ice pack may have lost contact with the coast (Jewell et al., 2023) relieving

internal ice stresses at SODA–A and SODA–B. The ice pack at SODA–C, in contrast, was isolated from this breakout by the northernmost lead, suggesting sustained internal ice stresses at the northern mooring. In situ and satellite ice velocities confirm differences in ice mobility across the mooring array following lead formation. The wind factor (the ratio of ice speed to wind speed) calculated from ice speeds observed by mooring ADCPs from 22–23 February was elevated at SODA–A and SODA–B relative to SODA–C (Figure 3.2c), which experienced near-stationary ice on 23 February (Figure 3.2a). On 23 February, Polar Pathfinder ice speeds (Tschudi et al., 2019) were higher around the southern moorings with a distinct decrease between SODA–B and SODA–C (not shown).

3.3 24–26 February: Storm passage

From 24–26 February 2019, a low-pressure system moved from the Bering Sea to the Chukchi and Beaufort Seas on the west side of the SODA mooring array. The storm originated in the Pacific Ocean and its track into the Beaufort Sea agrees with the unusual northward jet stream orientation that developed in this region in February–March 2019 (Overland 2020). On 25 February, the 975 mb low pressure center was located approximately 1000 km west of the center of the array (Figure 3.1b), then continued northward and dissipated over the following 24 hours. Wind speeds at the mooring sites peaked late on 25 February, reaching 14 m s^{-1} at SODA–A (Figure 3.3b), 16 m s^{-1} at SODA–B (Figure 4b), and 13 m s^{-1} at SODA–C (Figure 3.5b). Broadband ice speeds were fastest near the center of the mooring array (Figure 3.1b), reaching about 0.5 m s^{-1} at SODA–B and 0.3 m s^{-1} at SODA–A and SODA–C (Figure 3.2a).

Lead fraction decreased to below 7% near SODA–A and SODA–B on 24–25 February but increased to 14% on 26 February (Figure 3.2b). Though leads can be sites of rapid ice growth, they remain local weaknesses in the ice cover (Feltham 2008). These trends in ice fraction near the southern moorings likely reflect refreezing in leads followed by lead reopening along these preexisting weaknesses by the storm. Lead fraction near SODA–C remained below 5% during and after the storm (Figure 3.2b).

3.4 26–28 February: Observed inertial response

Following the low pressure system's passage, high pressure developed over the SODA mooring array (not shown). Over the course of these two weather systems the clockwise turning of the wind (Figure 3.3b, Figure 3.4b, Figure 3.5b) excited inertial oscillations in the sea ice and ocean mixed layer. Observed inertial oscillation strength varied across the mooring array, with stronger oscillations at the fractured southern sites. The maximum observed near-inertial mixed layer speed was 0.049 m s^{-1} on 28 February at SODA–A (Figure 3e), 0.042 m s^{-1} on 26 February at SODA–B (Figure 3.4e), and 0.018 m s^{-1} on 25 February at SODA–C (Figure 3.5e). The regional pattern in modeled inertial oscillation strength differed from the regional pattern in observed inertial oscillation strength. Modeled inertial oscillations were fastest at SODA–C and slowest at SODA–A, indicating the storm's inertial oscillation generation *potential* was strongest at the northern mooring site. Regional differences in modeled inertial oscillation strength reflect regional variation in the resonance of the wind forcing and differences in mixed layer depth but do not account for impacts of ice dynamics, which are not included in the model. The mixed layer was shallowest at SODA–C (average

mixed layer depth was 44 m at SODA–A, 41 m at SODA–B, 36 m at SODA–C; Figure 3.3d, Figure 3.4d, Figure 3.5d), contributing to stronger modeled velocities (Equation 3.4).

Comparing the predicted and observed near-inertial response at each mooring indicates varying degrees of inertial oscillation modification by unmodeled processes (i.e., ice dynamics). The maximum modeled near-inertial mixed layer speed at SODA–A was 0.050 m s^{-1} on 28 February (Figure 3.3e), comparable to the maximum near-inertial speed observed at that site. This similarity between observations and model results shows that inertial oscillation damping was modest at SODA–A despite high ice concentrations. At SODA–C, conversely, the model predicted a much stronger inertial response than developed in the observations. Mixed layer oscillations at SODA–C were predicted to reach about 0.10 m s^{-1} on 27 February (Figure 3.5e), making the modeled SODA–C response to this storm the strongest potential mixed layer inertial oscillation event under pack ice ($A > 0.85$) at any of the moorings throughout the year-long record. The 82% reduction in observed near-inertial velocity at SODA–C relative to the model implies significant damping by unmodeled processes, likely ice dynamics.

Importantly, these unmodeled processes at SODA–C impacted ice mobility differently at different frequencies. Despite the weaker near-inertial currents at SODA–C relative to SODA–A, observed broadband ice speeds and wind factor at SODA–C were comparable to those at SODA–A on 25 February (Figure 3.2a,c). At SODA–C, however, the angle between the wind and the SODA–C observed ice velocity remained relatively unchanging over the course of an inertial period (Figure 3.5c solid line),

reflecting the weak inertial frequency ice velocities. The modeled ice velocity, on the other hand, varied by 45° or more relative to the wind as the modeled ice underwent strong inertial oscillations (Figure 3.5c dotted line). At SODA–A, both the observed and modeled ice velocities experienced comparable deviations from the wind direction over the course of an inertial period (Figure 3.3c) as the ice swiftly changed direction and oscillated independently of the wind direction.

The SODA–B observed near-inertial response was weaker and lower frequency than the model's predicted response (Figure 3.4e). The maximum modeled near-inertial mixed layer speed was 0.074 m s^{-1} on 26 February, or 43% greater than the maximum observed speed, indicating an intermediate amount of damping by unmodeled processes at this central mooring. The frequency of the observed near-inertial mixed layer response was 0.99-1.01f while the modeled response was 1.02-1.04f. This slight frequency mismatch may be due to the reanalysis failing to exactly reproduce the winds at SODA–B. Indeed, winds from another reanalysis product (NCEP) have been shown to have lower energy than observations in this region at frequencies near and above the inertial frequency (Fine et al., 2021).

4 Discussion

This paper's results support Brenner et al. (2023a)'s suggestion that internal ice stresses filter out high-frequency ocean velocities while transmitting momentum at sub-inertial frequencies. McPhee (1978) came to a similar conclusion while examining data from AIDJEX: "Even though a whole region of ice moves with little apparent resistance, internal forces at smaller scales in the compact winter pack rapidly quell the

inertial component." He attributed the inhibition of high-frequency oscillations to a relatively unbroken ice pack, stating "Apparently as freeze-up progresses, the ice becomes rigid on a large enough scale to inhibit the short-period motion almost entirely" (McPhee 1978). By contrasting the inertial oscillation response at sites with differing histories of lead formation, our observations support McPhee (1978)'s longstanding hypothesis that floe scales determine if inertial motions are damped. However, our wintertime study demonstrates that a correspondence between increased ice fracturing and increased inertial oscillation strength is not strictly a seasonal phenomenon.

While this paper has focused on the magnitude of the sea ice and mixed layer near-inertial response, ice may also impact other aspects of this response. Hodographs of ice and mixed layer near-inertial velocity showed sometimes-elliptical orbits, with differences in near-inertial current structure across mooring sites as well as differences between the ice and ocean near-inertial velocity at each mooring (Figure 3.6). The theoretical ratio of the major to minor axes lengths is ω / f for free waves, so elliptical orbits can result from super-inertial frequencies. However, the elliptical axis ratios in Figure 3.6 are too large to be explained by the observed frequencies. The observed frequencies for the ice and mixed layer near-inertial velocities were 0.97-0.99f and 0.99-1.01f, respectively, at SODA–A, and 0.99-1.01f for both the ice and mixed layer at SODA–B. At SODA–C, the mixed layer frequency was 1.06-1.07f. No fitted frequency exceeded the $R^2 = 0.95$ goodness of fit threshold for ice velocity at SODA–C; the best fit frequency was 1.05-1.06f ($R^2 > 0.85$).

As the observed frequencies were close to the inertial frequency, the elliptical orbits suggest these inertial oscillations were not free waves. It is possible that the ice fracture orientation mechanically restricted the inertial current orientation; at SODA–B, in particular, the ice inertial oscillation ellipses align with the dominant axis of lead formation (Figure 3.6d-f). The major axes of the mixed layer inertial oscillation ellipses at SODA–A and SODA–B were rotated to the right of the sea ice ellipses, implying rotational shear in the near-inertial band. We suggest that the ways in which ice characteristics, including lead orientation, imprint on near-inertial currents is an important topic for future research.

Observations capable of simultaneously observing inertial oscillations and mixed layer depth, such as the ADCP data presented in this paper, are rare in the Arctic (but see Chapter 5.2.2 for a discussion of how this study's results could be extended using the Ice Tethered Profiler dataset). By comparing observed and slab-modeled inertial oscillations at two mooring locations, this study demonstrated substantial regional variation in the amount of inertial oscillation damping that occurred following the same storm. We next ask how these impacts could be parameterized. Ice concentrations above 0.85 and wind factor values below 2% have been used as "rule-of-thumb" thresholds to identify times when low-frequency ice motion is damped by internal ice stresses (e.g., Brenner et al., 2021), but we find that these proxies are inadequate for predicting inertial motion damping in our data.

Ice concentration from AMSR2 was high at all mooring sites throughout the storm (>0.97 at SODA–A, >0.92 at SODA–B, >0.89 at SODA–C; Figure 3.3a, Figure

3.4a, Figure 3.5a), which might suggest region-wide damping by internal stresses. However, observed differences in inertial oscillation damping between the fractured and unfractured sites demonstrate some amount of independence of inertial motions and ice concentration (i.e., inertial motion was less damped at SODA–A despite its higher ice concentration). This independence likely arose because leads can even be found in areas where ice concentrations derived from passive microwave data are near 100% (Willmes and Heinemann 2016). Remotely sensed sea ice concentrations depend on instrument resolution, ice thickness, and, for thermal infrared measurements, accurate cloud masking (Ludwig et al., 2020). Ice concentrations dropped below 85% at SODA–A and SODA–B (Figure 3.3a, Figure 3.4a) when calculated from ADCP altimeter data as the ratio of ice-covered distance to total (ice and open water) distance (Brenner et al., 2021), supporting the idea that the southern moorings experienced localized lead openings that were not captured by the passive microwave product.

We next tested if inertial oscillation damping could be inferred from wind factor values computed using a readily available satellite-derived daily ice drift product, Polar Pathfinder (Tschudi et al., 2019). The wind factor can be thought of as measuring ice mobility, or how readily the ice responds to forcing. When calculated using hourly ice velocity from the ADCP, the wind factor at SODA–C was around 2% on 26 and 28 February but decreased to near zero on 27 February in conjunction with very low ice speed (Figure 3.2b-c). This behavior is consistent with internal ice stresses decreasing ice motion. However, Polar Pathfinder did not capture this observed decline in wind factor. Instead, Polar Pathfinder wind factor near the northern mooring increased on 27

February (Figure 3.2d) due to unrealistically large Polar Pathfinder ice speed (around 0.1 m s^{-1}). Overall, we find no consistent differences in Polar Pathfinder wind factor across mooring locations between 25 February and 1 March (Figure 3.2d). In summary, our results do not show a relationship between inertial oscillation damping and either passive microwave ice concentration or low frequency ice mobility during this event.

Though our focus on a single storm limits our confidence in the universality of these results, we suggest that a metric like floe size distribution (FSD), which describes the horizontal scales of an assortment of floes (Rothrock and Thorndike 1984), might better predict near-inertial damping. While distinct floes are more easily identified in marginal ice zones, in winter the lengths of line segments on floes, or chord lengths, can be used to characterize FSD (Rothrock and Thorndike 1984). FSD has been shown to influence many aspects of the atmosphere-ice-ocean system including ice melt rate and surface wave propagation into the ice pack (Steele 1992; Collins et al., 2015). Algorithms have been developed to extract FSD statistics from satellite imagery (Denton and Timmermans 2022; Stern et al., 2018) and satellite altimeter data (Horvat et al., 2019). While existing FSD data sets do not cover the time and location of our study and applying these algorithms is outside the scope of the current work, we suggest that FSD records could be compared to existing high frequency Arctic mixed layer velocity records (such as the Ice-Tethered Profiler with Velocity data set; Williams et al., 2010) to refine the relationship between FSD and near-inertial motions.

Understanding the conditions that favor lead formation is an area of active research (e.g., Jewell and Hutchings 2023; Jewell et al., 2023; Lewis and Hutchings

2019; Rheinlænder et al., 2022). Ice strength increases with ice thickness so, in general, stronger mechanical forcing (i.e., faster winds) will more easily break up thinner ice (Weiss 2013; Graham et al., 2019). However, most leads form under tension rather than compression or shear (Lewis and Hutchings 2019) and ice has a much lower tensile strength than compressive or shear strength. This tensile failure mode may explain why observed lead formation is independent of ice age, thickness, and compressive strength (Lewis and Hutchings 2019), and why there has been no observed trend in lead formation in the Beaufort Sea over the last two decades (Lewis and Hutchings 2019; Willmes et al., 2023). Despite ongoing ice thinning and multiyear ice loss, future wintertime lead activity may depend primarily on future atmospheric patterns and their characteristic alignments of wind and coastal geometry (Lewis and Hutchings 2019). Thus, basin geometry, by way of its influence on lead formation, may be an unappreciated contributor to regional differences in Beaufort Sea inertial motions when midwinter pack ice conditions are present.

5 Summary and conclusion

This paper presented high temporal resolution observations of the sea ice and ocean near-inertial velocity response to a storm in February 2019 in the Beaufort Sea. These observations were interpreted alongside results from a coupled ice-ocean slab model that controlled for the effects of regional variation in wind forcing and mixed layer depth on inertial oscillation strength. Contrasting the observed and modeled responses across a region of varying sea ice lead activity showed that unmodelled processes, presumably ice dynamics, strongly damped the near-inertial response at the

northern mooring (77.7°N) but minimally impacted in the near-inertial response at the southern mooring (73°N). Our primary findings can be summarized as follows:

- Stronger, less damped inertial oscillations developed in the sea ice and ocean mixed layer following a mid-winter storm at the mooring site where a lead formation event had produced a more fractured ice pack
- Passive microwave ice concentration and low frequency ice mobility did not predict the strength of inertial oscillation damping during this event. Floe size distribution may be a useful metric for predicting inertial oscillation damping in consolidated ice.
- Unlike the near-inertial response, the broadband ice velocity did not vary in accord with the history of lead activity. Ice dynamics selectively filtered out high frequency motions.

Many past studies have demonstrated increased inertial oscillation damping in dense, mid-winter sea ice relative to marginal ice conditions. By comparing ice conditions before, during, and after a mid-winter storm in which inertial oscillations were strongly damped at one study site and not at another, our results shed light on the wintertime ice conditions that may give rise to this damping. Specifically, our results showed that stronger inertial oscillations were found at the study site with a recent history of lead activity. While this is not a causal link, a slab model eliminated many other potential explanatory variables including the strength and resonance of the wind, the ice-ocean drag coefficient, the mixed layer depth, and the nearby sea ice concentration as measured by passive microwave satellites. We hypothesize that a

mechanistic link between the presence of leads and the strength of inertial oscillations may relate to gaps between ice floes permitting impulsive acceleration of the ice and underlying mixed layer, more effectively transferring the inertial part of the wind forcing to the ice and ocean. We cannot test this hypothesis with the data at hand and suggest that experiments using idealized three-dimensional coupled ice-ocean models initialized with varying floe configurations would be better suited to the task. Additionally, Chapter 5.2.2 suggests an approach using the Ice Tethered Profiler dataset to statistically bolster the link between inertial oscillation damping and lead activity.

Leads, which can extend hundreds of kilometers from coastal promontories into the ice pack, may link ocean near-inertial velocities to distant coastal boundaries. Future trends in winter inertial oscillation strength may depend more on trends in lead activity and floe size than on commonly modeled parameters like ice thickness. Consequently, efforts to predict wintertime inertial motions in the Arctic will benefit from ongoing efforts to accurately represent floe size distribution in models (Zhang et al., 2016, 2015; Roach et al., 2018) and to develop ice rheologies that realistically model cracks and leads in the ice pack (Ólason et al., 2022).

6 Acknowledgments

This research was funded through the Office of Naval Research (Laura Crews, Craig M. Lee, Luc Rainville, and Samuel Brenner), the National Science Foundation (LC), and Schmidt Futures (SB). The SODA project, including the collection and analysis of the data presented here, was funded by ONR grant N00014-14-1-2377 (CL, LR, SB). Data analysis and synthesis were also supported by ONR grants N00014-18-1-2689 (SB) and N00014-18-1-2694 (LC). This material is based upon work supported by

the National Science Foundation Graduate Research Fellowship Program under Grant DGE-1762114 (LC). Any opinions, findings, and conclusions or recommendations expressed in this material are those of the author(s) and do not necessarily reflect the views of the National Science Foundation. SB was supported through the Scale Aware Sea Ice Project (SASIP). SASIP is supported by Schmidt Futures, a philanthropic initiative that seeks to improve societal outcomes through the development of emerging science and technologies.

We thank the captain and crew of USCGC Healy for their expert work during the mooring deployment and recovery cruises in 2018 and 2019. We also appreciate engineering and operational support by Jason Gobat, Eric Boget, and Ben Jokinen (University of Washington, Applied Physics Laboratory). Discussion with Arthur Nowell improved the quality of the writing.

7 Data availability statement

The mooring measurements and model results described in this paper are available at http://hdl.handle.net/1773/50613. ADCP ocean velocity measurements and mixed layer depth for the full deployments of the SODA moorings are available at http://hdl.handle.net/1773/49495

ERA5 reanalysis (Hersbach et al., 2023) is available at https://doi.org/10.24381/cds.adbb2d47

Daily NSIDC Polar Pathfinder sea ice drift (Tschudi et al., 2019) is available at https://nsidc.org/data/nsidc-0116/versions/4

AMSR2 sea ice concentration (Spreen et al., 2008) is available at https://seaice.uni-bremen.de/sea-ice-concentration/amsre-amsr2/

Sea ice lead classification (Reiser et al., 2020; Willmes and Heinemann 2016) is available at https://meteo.uni-trier.de/v2/arcleads.php.

MODIS imagery (MODIS Characterization Support Team 2017) is available at https://ladsweb.modaps.eosdis.nasa.gov/missions-and-

measurements/products/MOD021KM and https://ladsweb.modaps.eosdis.nasa.gov/missions-and-measurements/products/MYD021KM

Tidal velocities from the Arc5km2018 model (Erofeeva and Egbert 2020) are available at https://arcticdata.io/catalog/view/doi:10.18739/A21R6N14K

8 References

Alford, M. H. (2001). Internal swell generation: The spatial distribution of energy flux from the wind to mixed layer near-inertial motions. *Journal of Physical Oceanography,* 31 (8), 2359 – 2368. doi:10.1175/1520-0485(2001)031⟨2359:ISGTSD⟩2.0.CO;2

Brenner, S. (2022). The role of sea ice in mediating atmosphere-ice-ocean momentum transfer [Doctoral dissertation, University of Washington]. http://hdl.handle.net/1773/49108

Brenner, S., Rainville, L., Thomson, J., Cole, S., and Lee, C. (2021). Comparing observations and parameterizations of ice-ocean drag through an annual cycle across the Beaufort Sea. *Journal of Geophysical Research: Oceans, 126*(3), e2020JC016977. doi:10.1029/2020JC016977

Brenner, S., Thomson, J., Rainville, L., Crews, L., and Lee, C. (2023a). Wind-driven motions of the ocean surface mixed layer in the western Arctic. *Journal of Physical Oceanography, 53*(7), 1787–1804. doi:10.1175/JPO-D-22-0112.1

Brenner, S., Thomson, J., Rainville, L., Torres, D., Doble, M., Wilkinson, J., & Lee, C. (2023b). Acoustic sensing of ocean mixed layer depth and temperature from uplooking ADCPs. *Journal of Atmospheric and Oceanic Technology, 40*(1), 53–64. doi:10.1175/JTECH-D-22-0055.1

Cole, S. T., Toole, J. M., Rainville, L., & Lee, C. M. (2018). Internal waves in the Arctic: Influence of ice concentration, ice roughness, and surface layer stratification. *Journal of Geophysical Research: Oceans, 123*(8), 5571–5586. doi:10.1029/2018JC014096

Collins III, C. O., Rogers, W. E., Marchenko, A., & Babanin, A. V. (2015). In situ measurements of an energetic wave event in the Arctic marginal ice zone. *Geophysical Research Letters, 42*(6), 1863–1870. doi:10.1002/2015GL063063

Comiso, J. C., Parkinson, C. L., Gersten, R., & Stock, L. (2008). Accelerated decline in the Arctic sea ice cover. *Geophysical Research Letters, 35*, L01703. doi:10.1029/2007GL031972

D'Asaro, E. A. (1985). The energy flux from the wind to near-inertial motions in the surface mixed layer. *Journal of Physical Oceanography, 15*(8), 1043–1059. doi:10.1175/ 1520-0485(1985)015⟨1043:TEFFTW⟩2.0.CO

D'Asaro, E. A. (1989). The decay of wind-forced mixed layer inertial oscillations due to the β effect. *Journal of Geophysical Research, 94*(C2), 2045–2056.

doi:10.1029/ JC094iC02p02045

D'Asaro, E. A., and Morehead, M. D. (1991). Internal waves and velocity fine structure in the Arctic Ocean. *Journal of Geophysical Research: Oceans*, 96(C7), 12725–12738. doi:10.1029/91JC01071

Denton, A. A., and Timmermans, M.-L. (2022). Characterizing the sea-ice floe size distribution in the Canada Basin from high-resolution optical satellite imagery. *The Cryosphere*, 16(5), 1563–1578. doi:10.5194/tc-16-1563-2022

Dosser, H. V., Chanona, M., Waterman, S., Shibley, N. C., and Timmermans, M.-L. (2021). Changes in internal wave-driven mixing across the Arctic Ocean: Finescale estimates from an 18-year pan-arctic record. *Geophysical Research Letters*, 48(8), e2020GL091747. doi:10.1029/2020GL091747

Erofeeva, S., and Egbert, G. (2020). Arc5km2018: Arctic Ocean Inverse Tide Model on a 5 kilometer grid, 2018. *Arctic Data Center*. doi:10.18739/A21R6N14K

Feltham, D. L. (2008). Sea ice rheology. *Annual Review of Fluid Mechanics*, 40(1), 91–112. doi:10.1146/annurev.fluid.40.111406.102151

Fine, E. C., Alford, M. H., MacKinnon, J. A., and Mickett, J. B. (2021). Microstructure mixing observations and finescale parameterizations in the Beaufort Sea. *Journal of Physical Oceanography*, 51(1), 19–35. doi:10.1175/JPO-D-19-0233.1

Fine, E. C., and Cole, S. T. (2022). Decadal observations of internal wave energy, shear, and mixing in the western Arctic Ocean. *Journal of Geophysical Research: Oceans*, 127(5). doi:10.1029/2021JC018056

Gimbert, F., Jourdain, N. C., Marsan, D., Weiss, J., and Barnier, B. (2012a). Recent mechanical weakening of the Arctic sea ice cover as revealed from larger inertial oscillations. *Journal of Geophysical Research: Oceans*, 117(C11). doi:10.1029/2011JC007633

Gimbert, F., Marsan, D., Weiss, J., Jourdain, N. C., and Barnier, B. (2012b). Sea ice inertial oscillations in the Arctic basin. *The Cryosphere*, 6(5), 1187–1201. doi:10.5194/tc-6-1187-2012

Graham, R. M., et al. (2019). Winter storms accelerate the demise of sea ice in the Atlantic sector of the Arctic Ocean. *Scientific Reports*, 9(1), 9222. doi:10.1038/s41598-019-45574-5

Guthrie, J. D., Morison, J. H., and Fer, I. (2013). Revisiting internal waves and mixing in the Arctic Ocean. *Journal of Geophysical Research: Oceans*, 118(8), 3966–

3977. doi:10.1002/jgrc.20294

Hersbach, H., et al. (2023). ERA5 hourly data on single levels from 1940 to present. *Copernicus Climate Change Service (C3S) Climate Data Store (CDS)* [Dataset]. doi:10.24381/cds.adbb2d47

Horvat, C., et al. (2019). Estimating the sea ice floe size distribution using satellite altimetry: Theory, climatology, and model comparison. *The Cryosphere, 13*(11), 2869–2885. doi:10.5194/tc-13-2869-2019

Jewell, M. E., and Hutchings, J. K. (2023). Observational perspectives on Beaufort Sea ice breakouts. *Geophysical Research Letters, 50*, e2022GL101408. doi:10.1029/2022GL101408

Jewell, M. E., Hutchings, J. K., and Geiger, C. A. (2023). Atmospheric highs drive asymmetric sea ice drift during lead opening from Point Barrow. *The Cryosphere, 17*, 3229–3250. doi:10.5194/tc-17-3229-2023

Kawaguchi, Y., Itoh, M., Fukamachi, Y., Moriya, E., Onodera, J., Kikuchi, T., and Harada, N. (2019). Year-round observations of sea-ice drift and near-inertial internal waves in the Northwind Abyssal Plain, Arctic Ocean. *Polar Science, 21*, 212–223. doi:10.1016/j.polar.2019.01.004

Kwok, R., and Rothrock, D. (2009). Decline in Arctic sea ice thickness from submarine and ICESat records: 1958–2008. *Geophysical Research Letters, 36*(15), L15501. doi:10.1029/2009GL039035

Large, W. G., and Yeager, S. G. (2004). Diurnal to decadal global forcing for ocean and sea-ice models: The data sets and flux climatologies. *Technical Note NCAR/TN-460+STR, National Center for Atmospheric Research,* Boulder, Colorado.

Leaman, K. D., and Sanford, T. B. (1975). Vertical energy propagation of inertial waves: A vector spectral analysis of velocity profiles. *Journal of Geophysical Research, 80*(15), 1975–1978. doi:10.1029/JC080i015p01975

Lee, C. M., Cole, S., Doble, M., Guthrie, J., Harper, S., et al. (2016). Stratified Ocean Dynamics in the Arctic: Science and experiment plan. *Technical Report APL-UW TR 1601, Applied Physical Laboratory, University of Washington,* Seattle, WA, 46 pp.

Levine, M. D., Paulson, C. A., and Morison, J. H. (1987). Observations of internal gravity waves under the Arctic pack ice. *Journal of Geophysical Research: Oceans, 92*(C1), 779–782. doi:10.1029/JC092iC01p00779

Lewis, B. J., and Hutchings, J. K. (2019). Leads and associated sea ice drift in the

Beaufort Sea in winter. *Journal of Geophysical Research: Oceans, 124*, 3411–3427. doi:10.1029/2018JC014898

Ludwig, V., Spreen, G., and Pedersen, L. T. (2020). Evaluation of a new merged sea-ice concentration dataset at 1 km resolution from thermal infrared and passive microwave satellite data in the Arctic. *Remote Sensing, 12*(19). doi:10.3390/rs12193183

Martin, T., Steele, M., and Zhang, J. (2014). Seasonality and long-term trend of Arctic Ocean surface stress in a model. *Journal of Geophysical Research: Oceans, 119*(3), 1723–1738. doi:10.1002/2013JC009425

Martini, K. I., Simmons, H. L., Stoudt, C. A., and Hutchings, J. K. (2014). Near-inertial internal waves and sea ice in the Beaufort Sea. *Journal of Physical Oceanography, 44*(8), 2212–2234. doi:10.1175/JPO-D-13-0160.1

McPhee, M. G. (1978). A simulation of inertial oscillation in drifting pack ice. *Dynamics of Atmospheres and Oceans, 2*(2), 107–122. doi:10.1016/0377-0265(78)90005-2

McPhee, M. G. (2012). Advances in understanding ice–ocean stress during and since AIDJEX. *Cold Regions Science and Technology, 76–77*, 24–36. doi:10.1016/j.coldregions.2011.05.001

MODIS Characterization Support Team. (2017). MODIS 1km calibrated radiances product. *NASA MODIS Adaptive Processing System, Goddard Space Flight Center, USA.* doi:10.5067/MODIS/MOD021KM.061

Ólason, E., Boutin, G., Korosov, A., Rampal, P., Williams, T., Kimmritz, M., Dansereau, V., and Samaké, A. (2022). A new brittle rheology and numerical framework for large-scale sea-ice models. *Journal of Advances in Modeling Earth Systems, 14*(8), e2021MS002685. doi:10.1029/2021MS002685

Overland, J. (2020). Less climatic resilience in the Arctic. *Weather and Climate Extremes, 30*, 100275. doi:10.1016/j.wace.2020.100275

Plueddemann, A. J., and Farrar, J. T. (2006). Observations and models of the energy flux from the wind to mixed-layer inertial currents. *Deep Sea Research Part II: Topical Studies in Oceanography, 53*(1), 5–30. doi:10.1016/j.dsr2.2005.10.017

Pollard, R., and Millard, R. (1970). Comparison between observed and simulated wind generated inertial oscillations. *Deep Sea Research and Oceanographic Abstracts, 17*(4), 813–821. doi:10.1016/0011-7471(70)90043-4

Rainville, L., Wilkinson, J., Durley, M. E., Harper, S., DiLeo, J., Doble, M., et al.

(2020). Improving situational awareness in the Arctic Ocean. *Frontiers of Marine Sciences.* doi:10.3389/fmars.2020.581139

Rainville, L., and Woodgate, R. A. (2009). Observations of internal wave generation in the seasonally ice-free Arctic. *Geophysical Research Letters, 36*(23), L23604. doi:10.1029/2009GL041291

Rampal, P., Weiss, J., and Marsan, D. (2009). Positive trend in the mean speed and deformation rate of Arctic sea ice, 1979–2007. *Journal of Geophysical Research, 114,* C05013. doi:10.1029/2008JC005066

Reiser, F., Willmes, S., and Heinemann, G. (2020). A new algorithm for daily sea ice lead identification in the Arctic and Antarctic winter from thermal-infrared satellite imagery. *Remote Sensing, 12*(12), 1957. doi:10.3390/rs12121957

Rheinlænder, J. W., Davy, R., Ólason, E., Rampal, P., Spensberger, C., Williams, T. D., Korosov, A., and Spengler, T. (2022). Driving mechanisms of an extreme winter sea ice breakup event in the Beaufort Sea. *Geophysical Research Letters, 49*(12), e2022GL099024. doi:10.1029/2022GL099024

Richter-Menge, J. A., McNutt, S. L., Overland, J. E., and Kwok, R. (2002). Relating Arctic pack ice stress and deformation under winter conditions. *Journal of Geophysical Research: Oceans, 107.* doi:10.1029/2000JC000477

Roach, L. A., Horvat, C., Dean, S. M., and Bitz, C. M. (2018). An emergent sea ice floe size distribution in a global coupled ocean-sea ice model. *Journal of Geophysical Research: Oceans, 123*(6), 4322–4337. doi:10.1029/2017JC013692

Rothrock, D., Percival, D., and Wensnahan, M. (2008). The decline in Arctic sea-ice thickness: Separating the spatial, annual, and interannual variability in a quarter century of submarine data. *Journal of Geophysical Research, 113,* C05003. doi:10.1029/2007JC004252

Rothrock, D. A., and Thorndike, A. S. (1984). Measuring the sea ice floe size distribution. *Journal of Geophysical Research: Oceans, 89*(C4), 6477–6486. doi:10.1029/JC089iC04p06477

Spreen, G., Kaleschke, L., and Heygster, G. (2008). Sea ice remote sensing using AMSR-E 89 GHz channels. *Journal of Geophysical Research: Oceans, 113*(C2). doi:10.1029/2005JC003384

Steele, M. (1992). Sea ice melting and floe geometry in a simple ice-ocean model. *Journal of Geophysical Research: Oceans, 97*(C11), 17729–17738. doi:10.1029/92JC01755

Stern, H. L., Schweiger, A. J., Stark, M., Zhang, J., Steele, M., and Hwang, B. (2018). Seasonal evolution of the sea-ice floe size distribution in the Beaufort and Chukchi seas. *Elementa: Science of the Anthropocene, 6.* doi:10.1525/elementa.305

Tschudi, M., Meier, W. N., Stewart, J. S., Fowler, C., and Maslanik, J. (2019). Polar Pathfinder daily 25 km EASE-Grid sea ice motion vectors, version 4. *NASA National Snow and Ice Data Center Distributed Active Archive Center.* doi:10.5067/INAWUWO7QH7B

Weiss, J. (2013). Drift, deformation, and fracture of sea ice (1st ed.). *SpringerBriefs in Earth Sciences, Springer Dordrecht*, XVI, 83 pp. doi:10.1007/978-94-007-6202-2

Williams, A. J., Thwaites, F. T., Morrison, A. T., Toole, J. M., and Krishfield, R. (2010). Motion tracking in an acoustic point-measurement current meter. *OCEANS'10 IEEE SYDNEY, 1–8.* doi:10.1109/OCEANSSYD.2010.5603862

Willmes, S., and Heinemann, G. (2016). Sea-ice wintertime lead frequencies and regional characteristics in the Arctic, 2003–2015. *Remote Sensing, 8*(1), 4. doi:10.3390/rs8010004

Willmes, S., Heinemann, G., and Schnaase, F. (2023). Patterns of wintertime Arctic sea ice leads and their relation to winds and ocean currents. *The Cryosphere Discussions, 2023*, 1–23. doi:10.5194/tc-2023-22

Wunsch, C., and Ferrari, R. (2004). Vertical mixing, energy, and the general circulation of the oceans. *Annual Review of Fluid Mechanics, 36*(1), 281–314. doi:10.1146/annurev.fluid.36.050802.122121

Zhang, J., Schweiger, A., Steele, M., and Stern, H. (2015). Sea ice floe size distribution in the marginal ice zone: Theory and numerical experiments. *Journal of Geophysical Research: Oceans, 120*(5), 3484–3498. doi:10.1002/2015JC010770

Zhang, J., Stern, H., Hwang, B., Schweiger, A., Steele, M., Stark, M., and Graber, H. C. (2016). Modeling the seasonal evolution of the Arctic sea ice floe size distribution. *Elementa: Science of the Anthropocene, 4.* doi:10.12952/journal.elementa.000126

9 Figures

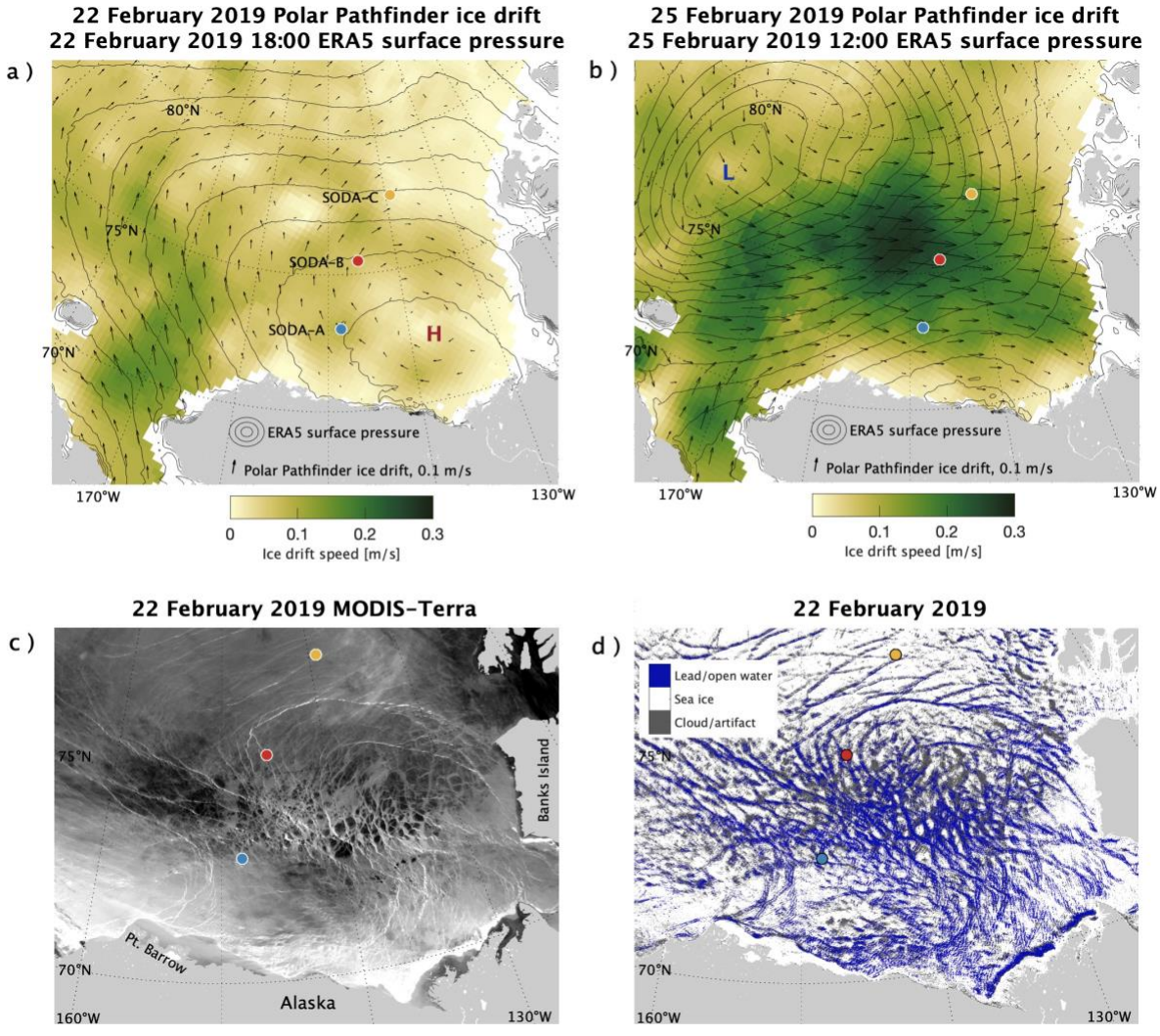

Figure 3.1 Regional atmospheric and sea ice conditions. (a-b) ERA5 surface pressure (gray contours) and Polar Pathfinder ice drift (color and black vectors; Tschudi et al., 2019) on (a) 22 February and (b) 25 February. (c-d) MODIS-Terra (c) brightness temperature (Band 31) imagery and (d) identified leads (Willmes and Heinemann 2016; Reiser et al., 2020) on 22 February. The SODA–A, SODA–B, and SODA–C mooring locations are shown in all panels.

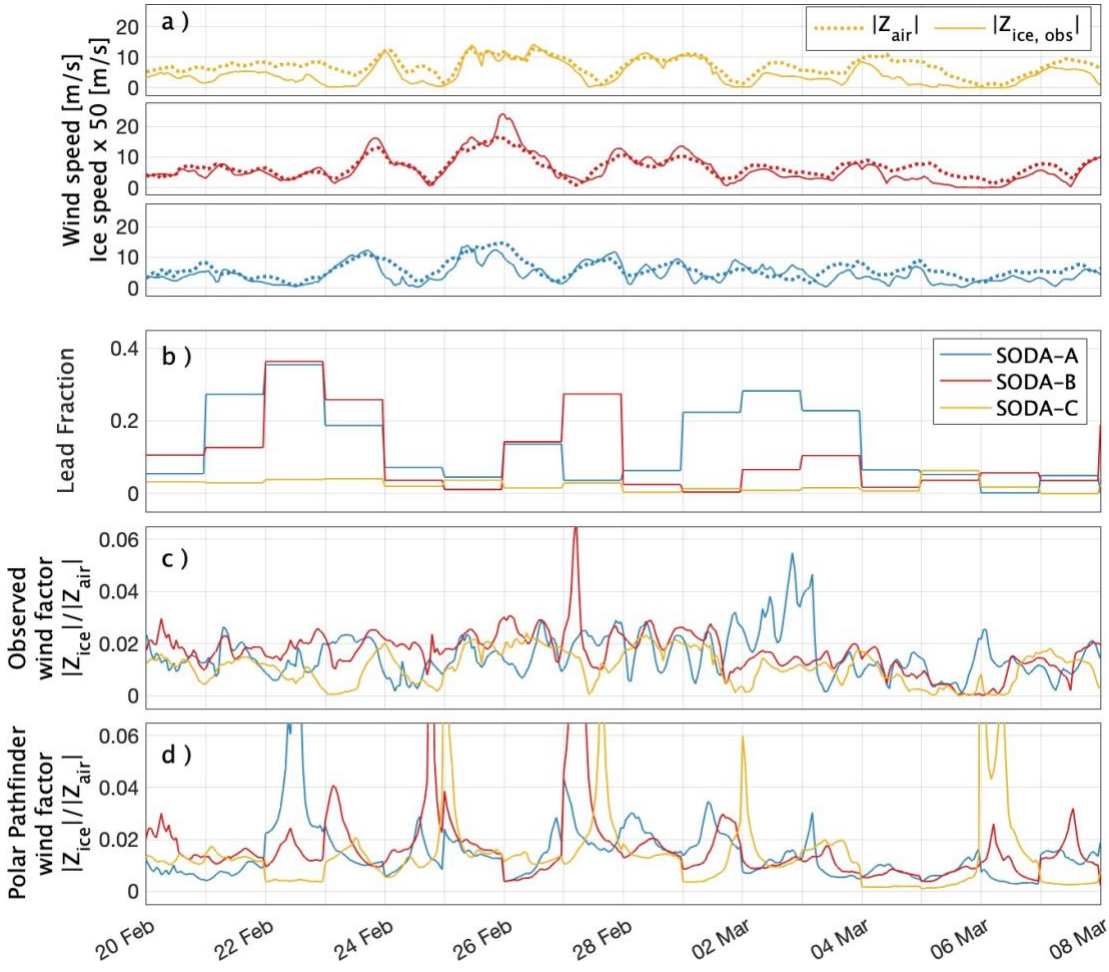

Figure 3.2 Comparison across moorings of (a) wind speed (dotted lines) and observed ice speed scaled by a factor of 50 (solid lines), (b) lead fraction (Willmes et al., 2023) in a 200 km × 200 km box centered on the mooring site, (c) wind factor calculated from ERA5 wind speed and observed ice speed, (d) wind factor calculated from ERA5 wind speed and Polar Pathfinder ice speed (Tschudi et al., 2019). Blue lines are for SODA–A, red lines are for SODA–B, and yellow lines are for SODA–C.

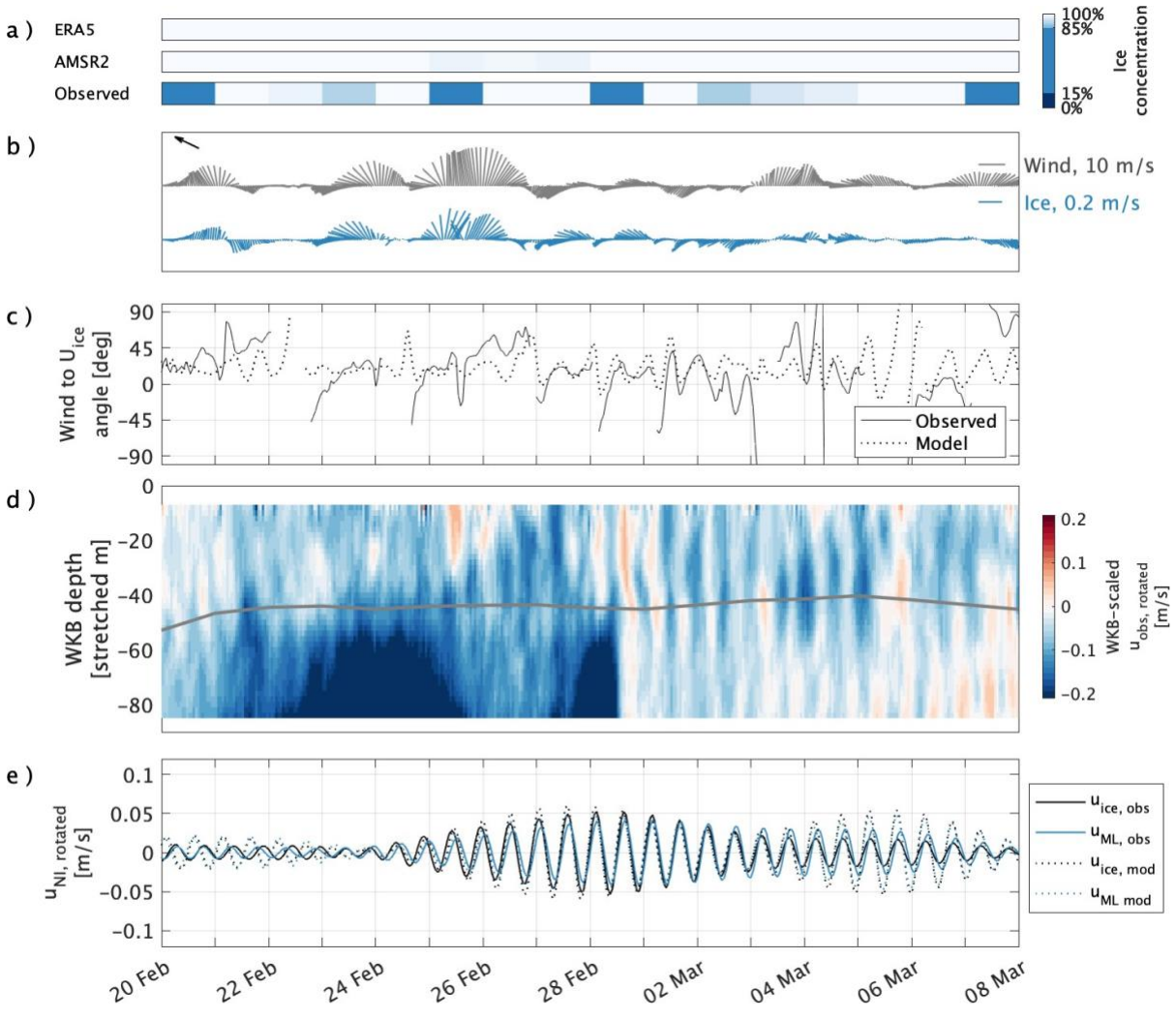

Figure 3.3 Data for the SODA–A mooring site. (a) Sea ice concentration from ERA5, AMSR2, and observed by the mooring altimeter. (b) Wind velocity from ERA5 and ice velocity measured by mooring ADCP. (c) The angle between the wind velocity and the observed (solid line) and modeled (dotted line) ice velocity, with positive values indicating ice deflected to the right of the wind. Angle not plotted for ice speeds below 0.03 m s^{-1}. (d) WKB-scaled velocity (colors) and mixed layer depth (gray line). (e) Observed (solid lines) and modeled (dotted lines) near-inertial sea ice velocity (black) and mixed layer averaged velocity (blue). The direction of maximum wind speed

defined a rotated coordinate system in which all velocities are plotted; north is indicated by the black arrow in the upper left corner of panel (b).

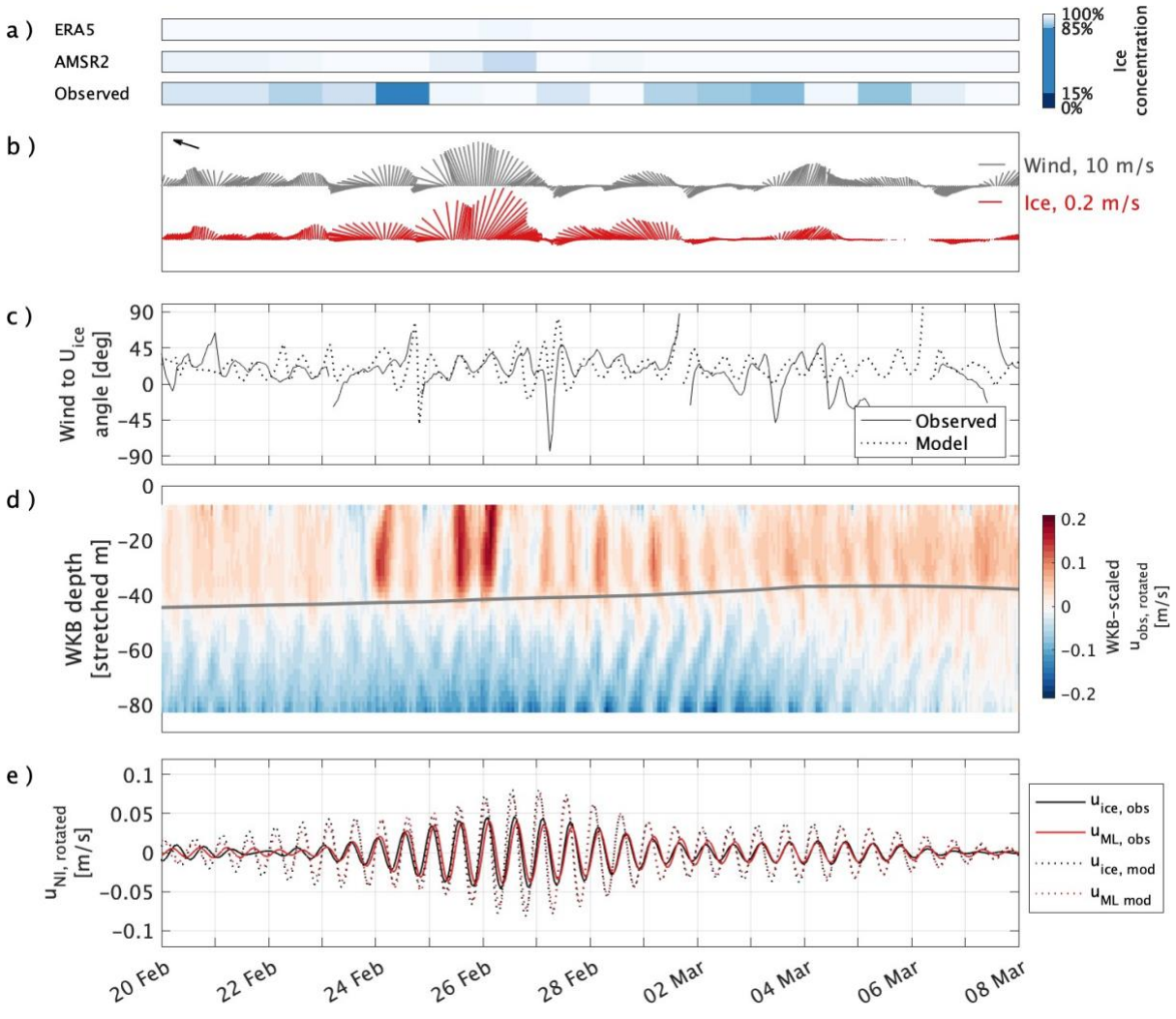

Figure 3.4 Data for the SODA–B mooring site. (a) Sea ice concentration from ERA5, AMSR2, and observed by the mooring altimeter. (b) Wind velocity from ERA5 and ice velocity measured by mooring ADCP. (c) The angle between the wind velocity and the observed (solid line) and modeled (dotted line) ice velocity, with positive values indicating ice deflected to the right of the wind. Angle not plotted for ice speeds below 0.03 m −1. (d) WKB-scaled velocity (colors) and mixed layer depth (gray line). (e) Observed (solid lines) and modeled (dotted lines) near-inertial sea ice velocity (black) and mixed layer averaged velocity (red). The direction of maximum wind speed defined

a rotated coordinate system in which all velocities are plotted; north is indicated by the black arrow in the upper left corner of panel (b).

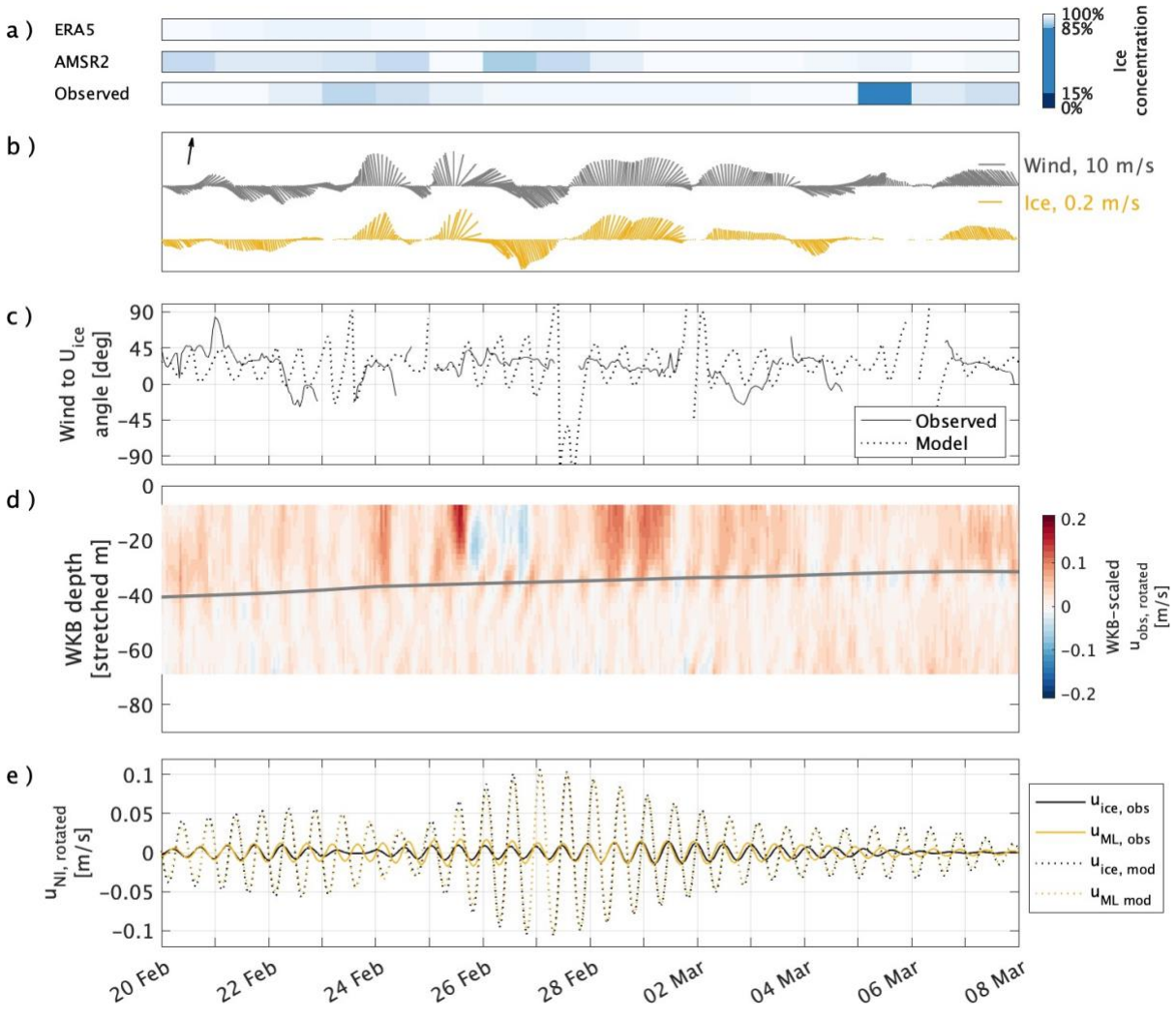

Figure 3.5 Data for the SODA–C mooring site. (a) Sea ice concentration from ERA5, AMSR2, and observed by the mooring altimeter. (b) Wind velocity from ERA5 and ice velocity measured by mooring ADCP. (c) The angle between the wind velocity and the observed (solid line) and modeled (dotted line) ice velocity, with positive values indicating ice deflected to the right of the wind. Angle not plotted for ice speeds below 0.03 m s $^{-1}$. (d) WKB-scaled velocity (colors) and mixed layer depth (gray line). (e) Observed (solid lines) and modeled (dotted lines) near-inertial sea ice velocity (black) and mixed layer averaged velocity (yellow). The direction of maximum wind speed

defined a rotated coordinate system in which all velocities are plotted; north is indicated by the black arrow in the upper left corner of panel (b).

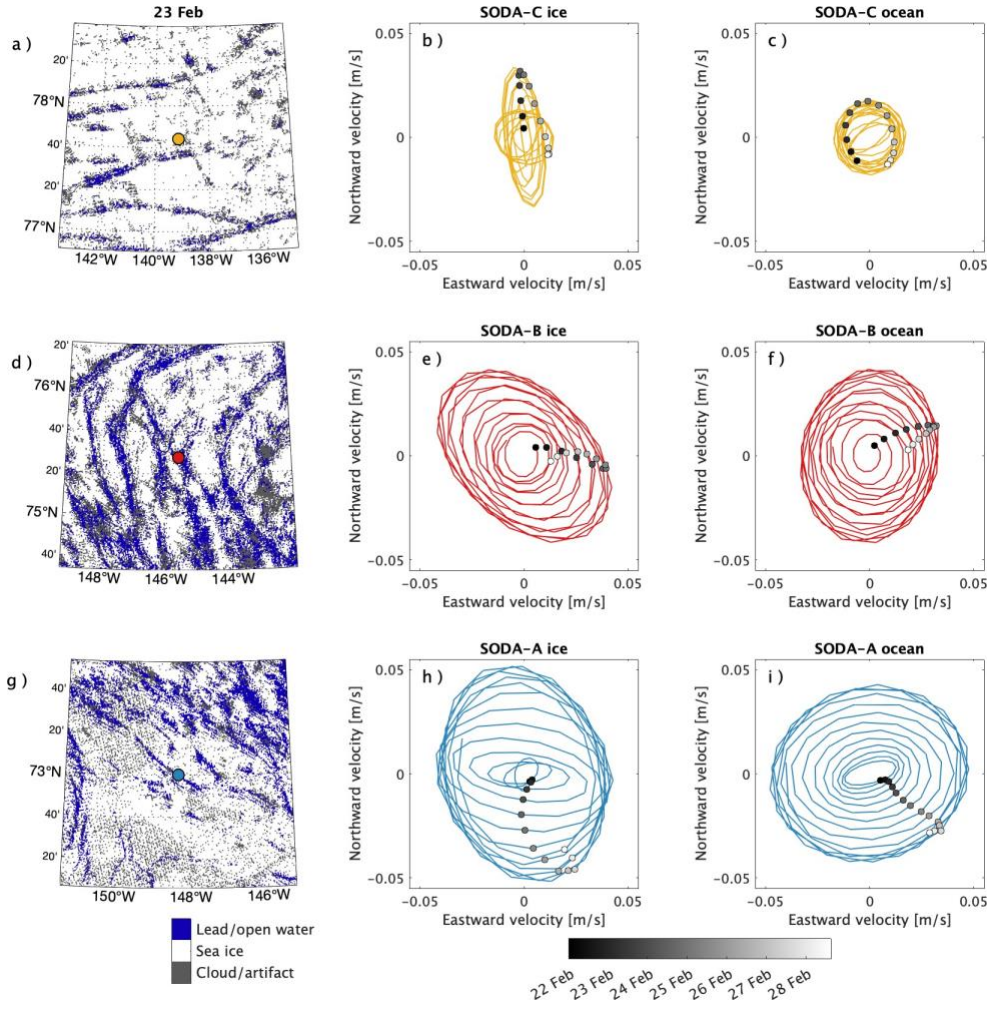

Figure 3.6 Sea ice leads and near-inertial hodographs at each mooring site. (a,d,g) Identified leads (Willmes and Heinemann 2016; Reiser et al., 2020) on 23 February in 200 km × 200 km regions surrounding each mooring, with mooring locations shown by colored dots. Hodographs at each mooring of observed near-inertial (b,e,h) sea ice velocity and (c,f,i) ocean mixed layer velocity. Grayscale points are plotted every inertial period.

Chapter 4 Coherence of Western Arctic sea ice inertial oscillations from satellite imagery

1 Introduction

Near-inertial internal waves (NIWs) are an important link between energy input to the ocean surface by the wind and diapycnal mixing in the ocean interior. These waves, whose frequencies are close to the Coriolis frequency, *f*, are a resonant response to ocean surface stress. In the Arctic Ocean, sea ice mediates atmosphere-ocean momentum transfer, and sea ice mechanics and dynamics modify the generation of inertial motions.

Decades of observations demonstrate that sea ice can suppress near-inertial motions in the Arctic, especially during the winter (Levine et al., 1987; Morison et al., 1985; Rainville and Woodgate, 2009; Brenner et al., 2023a). Inertial oscillations in the ice and ocean mixed layer are thought to be damped by internal stresses within the ice pack (Kawaguchi et al., 2019; Martini et al., 2014; Rainville and Woodgate 2009; Gimbert et al., 2012b), though shoaling of the mixed layer also explains some of observed acceleration of inertial oscillations in summer (Brenner et al., 2023a). In unconsolidated ice with negligible internal stresses, such as in the marginal ice zone, models show that sea ice might actually enhance inertial oscillation strength relative to ice-free conditions due to enhanced air-ice drag (Brenner et al., 2023a).

It has long been recognized that the Arctic internal wave field differs from that found at mid-latitudes for reasons beyond its low overall energy. In the Arctic, the internal wave field retains significant energy at relatively high frequencies (D'Asaro

and Morehead, 1991; Halle and Pinkel, 2003), thought to be a signature of wave generation beneath ice. Near-inertial internal waves generated beneath sea ice also had more energy at higher vertical wavenumbers than those generated in open water, increasing shear (Fine and Cole, 2022). Turbulence in the under-ice boundary layer acts as a sink for internal wave energy, a dissipation mechanism unique to ice-covered waters (Morison et al., 1985; Pinkel, 2005).

It has been hypothesized that Arctic sea ice loss could increase NIW generation and dissipation by enhancing atmosphere-ocean momentum transfer (Fine and Cole, 2022). However, recent studies report that there is no observed interannual trend in NIW energy or dissipation, estimated using a finescale parameterization, over the last several decades (Dosser et al., 2021; Fine and Cole, 2022; Guthrie et al., 2013), despite declining sea ice extent and thickness and increasing ice drift speeds (Comiso et al., 2008; Kwok and Rothrock, 2009; Rampal et al., 2009; Rothrock et al., 2008). While Arctic NIW energy has not increased overall, observations show the Arctic NIW field varies spatially and temporally by orders of magnitude (Chanona et al., 2018; Dosser et al., 2021; Guthrie et al., 2013), as is typical of the NIW field in the rest of the world oceans (Alford and Whitmont, 2007). This extreme variability means the lack of an interannual trend in NIW energy belies the increasing seasonality of the Arctic NIW field.

A seasonal cycle in Arctic NIW energy is emerging, though the precise phenology varies regionally and depends on the seasonality of the atmospheric forcing and ice characteristics, factors which may not optimally align with each other for NIW

generation. For example, the Canada Basin experiences two annual maxima in NIW energy: one peak in summer when sea ice concentrations are low, and a second, weaker peak in early winter when wind speeds are greatest (Dosser and Rainville, 2016). Seasonal cycles in NIW energy on the Beaufort continental slope (Martini et al., 2014) and Chukchi slope (Rainville and Woodgate, 2009) appear driven by the presence or absence of sea ice, while on the Northwind Abyssal Plain pycnocline near-inertial energy was greatest during the ice melting and ice forming periods (Kawaguchi et al., 2019).

The scale of sea ice inertial oscillations increased between 1979-2008, with the strongest effect in summer, likely due to mechanical weakening of the ice cover (Gimbert et al., 2012b). Trends in inertial activity in the ocean interior are more equivocal. Dosser et al. (2021) used a finescale parameterization applied to 18 years of hydrographic profiles to show that the mean summer internal wave-driven turbulent kinetic energy dissipation rate in the Canada Basin doubled in 2011-2019 relative to 2004-2010. Winter dissipation rates in the Canada Basin decreased between these time periods, resulting in the absence of an interannual trend (Dosser et al., 2021) as well as an increase in seasonality. Canada Basin hydrographic profiles also show NIW amplitude variability is increasing, suggesting increased generation of episodic, large-amplitude waves in response to changes in sea ice (Dosser and Rainville, 2016).

While decreasing ice concentration plays an important role in the Arctic NIW changes described above, ice concentration alone is an insufficient proxy for the potential for NIW generation, pointing to the importance of other ice characteristics.

The interannual variability in monthly-averaged amplitude of NIWs observed over 10 years in the Canada Basin was not explained by sea ice concentration or wind speed but was significantly correlated with the wind factor (the ratio of ice drift speed to wind speed), which may be dictated by factors such as ice roughness and internal stress (Dosser and Rainville, 2016). Cole et al. (2018) found that at intermediate ice concentrations typical of the marginal ice zone (15-80%) there was no clear dependence of internal wave energy on ice concentration while at high ice concentrations (>80%), smoother ice generated less energetic internal waves (Cole et al., 2018). A dependence on ice morphology was also suggested by Dosser et al. (2021), who hypothesized that the interannual decline in wintertime internal-wave driven dissipation observed in their study was due to decreased air-ice-ocean drag caused by multiyear ice loss.

Taken together, these studies demonstrate many ways in which sea ice adds an additional layer of complexity to the excitation and evolution of near-inertial currents in the Arctic Ocean. However, the fundamental processes governing the generation and propagation of near-inertial internal waves in ice-free regions are still relevant.

Near-inertial internal waves are generated by horizontal variations in mixed layer inertial oscillations that vertically displace (pump) the top of the pycnocline, transferring near-inertial energy from the mixed layer to the pycnocline (D'Asaro, 1989). The typical horizontal scales of atmospheric forcing are much larger than the horizontal ocean scales needed to match observed decay timescales of mixed layer inertial currents (D'Asaro, 1989), as the vertical group velocity of internal waves

increases with increasing horizontal wavenumber (Gill, 1984). Several mechanisms have been proposed to induce these smaller scales in the mixed layer. These mechanisms include fluctuations in wind stress associated with mesoscale structures in the atmosphere, β-refraction of inertial oscillations caused by change in *f* with latitude (D'Asaro, 1989; D'Asaro et al., 1995), and ζ-refraction of inertial oscillations by background flow in the mixed layer (Kunze, 1985; Young and Ben Jelloul, 1997). Both β- and ζ-refraction act by producing inertial oscillations of slightly different frequencies, eventually resulting in phase decoherence that reduces the horizontal wavelength of inertial oscillations.

In an ice-free, midlatitude setting, the Ocean Storms Experiment investigated the lateral structure and decay of near-inertial oscillations, demonstrating how β-refraction facilitated near-inertial energy transfer from the mixed layer to the ocean interior (D'Asaro et al., 1995). However, β-refraction's importance is limited at high latitudes where *f* varies slowly, and idealized model experiments found that smaller β decreased the efficiency of energy transfer from mixed layer inertial oscillations to the pycnocline (Guthrie et al., 2021). Unlike β-refraction, the effectiveness of ζ-refraction does not directly depend on latitude. Observations and idealized modeling of a North Atlantic mesoscale eddy dipole show ζ-refraction can swiftly reduce the wavelength of inertial oscillations and radiate energy into the ocean interior as internal waves (Asselin et al., 2020; Thomas et al., 2023). Depending on the sign of their vorticity, mesoscale eddies in the Arctic pycnocline have been shown enhance or inhibit the propagation of internal waves (Halle and Pinkel, 2003), but internal wave generation via ζ-refraction

has not been observed in the Arctic.

These midlatitude studies make it clear that the horizontal coherence scales of mixed layer inertial oscillations are critical to understanding the generation and propagation of NIWs, but it is uncommon for studies of Arctic internal waves to focus on these scales. Our work is guided by the hypothesis that spatial variability of sea ice dynamics and floe interactions on regional (10-100 km) spatial scales and near-inertial timescales can generate divergent mixed layer inertial oscillations, promoting near-inertial internal wave generation. Sea ice motion at inertial timescales is a long recognized feature of the Arctic ice pack, perhaps dating to Nansen's description of "tidal" pressure oscillations against the hull of the Fram (McPhee, 1978). Ice buoy data show substantial ice deformation and divergence at inertial timescales (Heil and Hibler, 2002), including periodic opening and closing of individual leads (Hutchings et al., 2005). However, few studies have addressed the horizontal structure of sea ice inertial oscillations, in part because existing data from drifting buoys are too geographically sparse to resolve the scales over which inertial oscillations are coherent.

This study addresses this gap by using satellite imagery to track sea ice motion on spatial scales ranging from local (10 km) to basin-wide (1000 km), interpreting these satellite-derived ice inertial velocities alongside mooring observations, drifting buoy trajectories, and idealized modeling. Tracked sea ice floes have proved useful in studying mesoscale dynamics of the underlying ocean (Lopez-Acosta et al., 2019; Manucharyan et al., 2022). Inertial frequency ice motion has also been observed in SAR imagery (Kwok et al., 2003), but ice floes tracked in satellite imagery have not

been used to study ocean inertial velocities. However, satellite imagery is well suited to studying inertial oscillations in the ocean mixed layer. Unlike lower frequency ice drift and mixed layer velocity, which often differ from each other due to wind forcing and internal ice stresses, the inertial currents of the ice and mixed layer are tightly coupled (Brenner et al., 2023a; McPhee, 1978). Thus, sea ice acts as an effective tracer of ocean mixed layer inertial currents even when the wind or internal ice stresses are active.

The primary aims of this study are to (1) observe the horizontal structure of sea ice inertial oscillations excited by an Arctic storm, (2) compare observed internal wave generation to theoretical inertial pumping produced by the mixed layer structure, and (3) explore possible causes of the observed inertial current structure and comment on its implications for experimental design and internal wave generation under future ice conditions. This chapter is organized as follows. Chapter 4.2 introduces the visual satellite imagery used to derive inertial ice velocities, in situ mooring and buoy observations, and additional remote sensing and reanalysis products. Chapter 4.3 describes analysis methods, and Chapter 4.4 presents the results. Our findings are discussed Chapter 4.5 and summarized in Chapter 4.6.

2 Data and data processing

2.1 Study region and time

This study focuses on the ice-covered part of the Beaufort Sea following a storm in July 2019, analyzing inertial oscillations in a region spanning approximately 72-81°N, 120-170°W. Particular attention is given to an approximately 200 km × 200 km region of the northern Beaufort Sea around a subsurface oceanographic mooring

located at 77.7°N, 139.1°W. This mooring is the northernmost mooring in an array of three moorings deployed from October 2018 to September 2019 as part of the Office of Naval Research-funded Stratified Ocean Dynamics of the Arctic (SODA) experiment. The mooring, called SODA–C, was located north of the seasonal ice zone and was covered by sea ice throughout its deployment.

To put this study period in seasonal context, Figure 4.1 shows the observed mixed layer inertial current speed throughout the SODA–C mooring deployment. Mixed layer near-inertial currents at the mooring were strongly seasonal, increasing in summer and autumn when the mixed layer depth decreased and sea ice concentration declined (Brenner et al., 2023a). This study coincides with the summer onset of shallower mixed layer depths and faster mixed layer inertial currents (Figure 4.1, Figure 4.2b).

This storm was chosen for analysis for several reasons. First, a high atmospheric pressure system followed the storm, providing the relatively cloud-free conditions required for ice motion tracking in satellite imagery. Second, the storm's south-to-north track meant it affected a large part of the Beaufort Sea, from the ice edge to the interior of the ice pack. Its impacts included strong inertial oscillations at the SODA–C mooring, which provided detailed observations of the ice, mixed layer, and pycnocline. Finally, this event was the first significant acceleration of inertial oscillations at SODA–C of the summer, minimizing the impacts of pre-existing inertial currents on the analysis (Figure 4.1).

2.2 VIIRS satellite imagery processing

The trajectories of inertially oscillating sea ice floes were tracked in visible satellite imagery from the Visible Infrared Imaging Radiometer Suite (VIIRS) instruments carried by the polar orbiting NOAA-20 and Suomi NPP satellites. Each of these satellites follows a pole-to-pole orbit and crosses the equator 14 times per day, with Suomi NPP's orbit leading NOAA-20 by 50 minutes (Cao et al., 2017; https://lpdaac.usgs.gov/data/get-started-data/collection-overview/missions/s-npp-nasa-viirs-overview). The VIIRS instrument's 3000 km swath width ensures no gaps in coverage near the equator, and results in significant swath overlap at high latitudes. This swath overlap can be used to produce multiple images per day at high latitude locations.

Level 1b image-resolution, or I-band, swath data and geolocation files for each satellite were downloaded from NASA's Earthdata Search portal. These files are identified by the NASA short-names VNP02IMG, VNP03IMG, VJ102IMG, and VJ103IMG. The NOAA-20 and Suomi NPP satellites collected images of some part of our study area approximately every 50 minutes between 10:00 and 01:00 UTC each day, with approximately 14 images taken per day at a given location. This daily period of repeated image collection was followed by an extended period of no images when the satellite orbits rotated around the globe and did not capture our study region.

Grayscale images were made with data from VIIRS's I1 band, which has a horizontal resolution of 375 m. The I1 band detects wavelengths of 0.6-0.68 μm, corresponding to the visible portion of the spectrum. Satellite imagery from VIIRS was

processed using the Satpy library for Python (Raspaud et al., 2024). I1-band data were resampled from swath coordinates to the NSIDC Sea Ice Polar Stereographic North projection (EPSG 3413) with 375 m horizontal resolution, matching the I-band resolution of the VIIRS instrument. The resulting grayscale images were saved as GeoTIFF files.

Ice motion tracking is possible when there is little or no cloud cover. The most widespread cloud free conditions occurred between 26 July 12:00 UTC to 28 July 00:00 UTC, so we use imagery collected during this period for our analysis. Prior to running the ice motion tracking algorithm, cloudy images were manually identified and removed. The basin-wide images (which had dimensions of approximately 1500 km × 1200 km) were divided into 300 km × 300 km subregions with 50% overlap (Supplementary Figure 4.1a). All of the 300 km × 300 km sub-images were manually inspected to determine if they should be included for ice motion tracking in that subregion. The time range of cloud-free images in each subregion is shown in Supplementary Figure 4.1a. In addition to limiting the impacts of clouds smaller than the entire basin, this sub-image approach allowed an image to be used when the subregion, but not the entire basin, was in the satellite's field of view. This subregion approach meant that differing subsets of the basin-wide image set were used for ice tracking in different parts of the basin. Ice velocities were later interpolated from the irregular image times to hourly resolution by least squares fitting an inertial frequency sinusoid (Chapter 4.3.2), eliminating difficulties associated with images from different times being used in different parts of the basin.

Previously developed ice floe tracking algorithms (e.g., Lopez-Acosta et al., 2019) employ false color imagery for floe tracking, as the combination of wavelengths used to produce false color images facilitate differentiation of clouds from sea ice. Making false color images from VIIRS data requires using data from the 750 m moderate-resolution bands as well as the 375 m image-resolution bands, resulting in lower resolution composite images. We elected to rely only on the higher resolution grayscale images produced by the I1 band to retain the highest resolution possible in the images used in floe tracking. As we focus on a relatively limited number of images, we were able to manually identify and eliminate cloudy images.

Data from additional satellites in the Joint Polar Satellite System fleet (i.e., the NOAA-21 satellite, which was launched in 2022, and the upcoming JPSS-3 and JPSS-4 satellites), were not yet available for our study focused on 2019, but imagery from these satellites will benefit similar studies in the future.

2.3 Mooring data

While the satellite imagery provided information about the spatial structure of inertial oscillations, mooring data provided information about ocean dynamics below the mixed layer. The SODA moorings were heavily instrumented to observe ocean temperature, salinity, and velocity in the upper ~80 m of the water column. Each mooring was equipped with three ADCPs measuring sea ice and ocean velocities. The ADCP data from the upper ADCPs were merged into velocity profiles with 2 m vertical resolution and hourly temporal resolution by Brenner et al. (2023b). We use these processed velocity profiles for this study. The sampling scheme used by the deepest,

downward-looking Workhorse Long Ranger ADCPs resulted in data that were too noisy to resolve inertial velocities so are not used here, but were able to show the depth and structure of intermittently observed pycnocline mesoscale eddies (not shown). Ice velocity data from the central SODA–B and northern SODA–C moorings were used to validate imagery-derived near-inertial velocities (Figure 4.4). Apart from this comparison, data from the southern SODA moorings are not used in this study. Mixed layer and pycnocline data from the northern SODA–C mooring are used to investigate internal wave generation during the study period (Chapter 4.4.4), so the instrument configuration of that mooring is described in detail next.

At the SODA–C mooring, ice and ocean velocity were measured by an upward-looking Nortek Signature-500 5-beam acoustic Doppler current profiler (ADCP) installed on a DeepWater Buoyancy Stablemoor500 float at 27 m depth. Ocean velocity data above 6 m were discarded due to sidelobe reflections. Ocean velocity was additionally measured by an upward-looking Teledyne Workhorse-300 ADCP at 68 m depth. Mixed layer depth was derived from acoustic backscatter and inertial shear in the ADCP data (Brenner et al., 2023b). Additional information about SODA mooring ADCP processing is available in Brenner et al. (2021) and Brenner et al. (2023b).

Temperature, salinity, and pressure at SODA–C were observed by a variety of sensors. A “breakaway chain”, which extended upwards from the Stablemoor float, observed ocean temperature every 2 m at 3-hour intervals. This buoyant instrument chain was designed with weak links that would fail upon impact with large ice keels. Anticipated instrument loss following keel collisions meant recovered data during our

study period extended to a shallowest depth of 19 m. Below the breakaway chain, Sea-Bird Scientific SBE 37 MicroCATs measured temperature, conductivity, and pressure at 38 m, 43 m, 60 m, and 77 m. An additional MicroCAT at 48 m returned temperature data but not pressure nor conductivity data. The MicroCATs were interspersed with Sea-Bird Scientific SBE 56 temperature sensors at 33 m, 55 m, 65 m, and 70 m. Sampling intervals for the MicroCATs and SBE 56s ranged from 1-3 minutes; data from these instruments were averaged in 120-minute time bins. Breakaway chain temperature measurements were interpolated to these same 120-minute timesteps.

2.4 International Arctic Buoy Program data

Satellite-derived ice inertial velocities were compared to the trajectories of Lagrangian buoys from the International Arctic Buoy Program (IABP) archive (https://iabp.apl.uw.edu/WebData/). Buoy positions were interpolated to hourly timesteps and buoy velocity was calculated from displacement. Buoys with data gaps longer than three hours were not used. Two buoys appeared to be stationary; we assume this resulted from faulty GPS readings and removed buoys with average computed velocities below 0.5 cm s^{-1}. Buoys positions were then compared to the locations for which gridded satellite-derived near-inertial ice velocities were available. As the primary use of the buoy velocities was to validate and add context to the gridded VIIRS-derived ice velocities (Chapter 4.3.3), buoys were retained only if satellite-derived velocities were available in one of the nine closest grid cells (a 36 km × 36 km region) encompassing the buoy's position. Eight buoys met these criteria; their locations are shown in Figure 4.4a.

2.5 Atmospheric reanalysis and additional remote sensing products

Surface air pressure and 10-m wind from ERA5 (Hersbach et al., 2023) at hourly temporal resolution and 0.25° spatial resolution were used to understand the atmospheric conditions forcing the ice and ocean dynamics studied here. ERA5 wind and sea ice concentration were also used to force an idealized slab model. The SODA moorings were entirely subsurface to protect the instrumentation from sea ice, so in situ meteorological observations were not collected.

Daily passive microwave sea ice concentration from AMSR2 at 3.125-km horizontal resolution (Spreen et al., 2008) and sea ice motion at 25-km horizontal resolution and daily temporal resolution from NSIDC's Polar Pathfinder product (Tschudi et al., 2019) were used to interpret changes in the ice pack at times when clouds obscured VIIRS imagery.

3 Methods

3.1 Ice motion tracking

Ice motion tracking was performed in satellite images of each geographic subregion. The positions of tracked points were extracted from each image in that subregion's cloud-free image set using MATLAB's implementation of the Kanade-Lucas-Tomasi (KLT) feature-tracking algorithm (https://www.mathworks.com/help/vision/ref/vision.pointtracker-system-object.html). Histogram equalization to enhance contrast was applied to each subregion image prior to ice motion tracking. The tracked points were chosen in the first image using a minimum eigenvalue-based corner detection algorithm. The tracking algorithm then

identified the updated locations of these points in subsequent images. The tracking algorithm was able to track points through the extended periods of no imagery separating one day from the next. Tracks were retained only if a point was identified in at least six images spanning at least 8 hours. This approach is analogous to particle image velocimetry and does not include a segmentation step to determine floe outlines.

3.2 Velocity fitting and binning of tracked ice trajectories

The ice motion tracking procedure yielded each tracked point's geographic coordinates in each image. These coordinate time series were used to calculate the ice velocity at the irregularly spaced image times. To ease further analysis, the velocity was assumed to consist of an inertially oscillating component and a subinertial "background" component. These components were modeled using a nonlinear least squares fit of the form

$$u_{ice}(t) = A_{east}\, cos(\omega(t - t_0) - \phi_{east}) + B_{east}(t - t_0) + C_{east} \quad 4.1$$

$$v_{ice}(t) = A_{north}\, cos(\omega(t - t_0) - \phi_{north}) + B_{north}(t - t_0) + C_{north} \quad 4.2$$

This fitting was performed separately for the eastward northward components of the image-derived ice velocities to find the amplitudes, A, and phases, ϕ, of the eastward and northward inertial currents, and the eastward or northward background currents $B(t-t_0) + C$. Fitting the northward and eastward inertial amplitudes separately permits elliptical orbits, whereas a freely oscillating, purely inertial-frequency oscillation would have a circular orbit. The frequency ω used in the fit was spatially constant and equal to the Coriolis frequency at 76°N (i.e., an *f*-plane was assumed). Rotary spectra of the sea

ice velocities observed by the SODA moorings throughout their deployments showed a strong peak at the inertial frequency (Brenner et al., 2023a their Figure 6), supporting our assumption that the dominant frequency of the oscillatory component of the fitted velocity should be inertial. The reference time t_0 was 20 July 2019.

This procedure assumes the inertial current amplitude, phase, and background flow parameters for a tracked point were constant throughout the image time series. The R^2 value of the fit for both velocity components was required to exceed 0.5 or the tracked point's trajectory was excluded from the analysis. Approximately 29,000 points were tracked through at least six images and successfully fit with velocity and used in the subsequent analysis, with 99% of these points tracked for at least 24 hours (~2 inertial periods) within the 36-hour imagery time range (26 July 12:00 UTC to 28 July 00:00 UTC). Equations 4.1 and 4.2 fit the observed velocities very well, with median R^2 values of 0.96 and 0.97 for the fits to the eastward and northward observed velocities, respectively (Supplementary Figure 4.1). Supplementary Figure 4.1a shows the number of images used, the time range of successful tracking, and the number of tracked points for each geographic subregion. As our aim is to produce a stationary view of inertial motions, rather than examine the evolution of inertial motions over time, these tracking times are adequate.

After finding the ice velocity fitting parameters for each tracked ice trajectory, complex ice velocities $Z_{ice}(t) = u_{ice}(t) + iv_{ice}(t)$ were calculated for each trajectory at hourly intervals. This calculated velocity was restricted to the time range of the subregion images through which the trajectory was tracked. In other words, the

calculated velocity was not extrapolated outside of the time range in which the tracked point was detected in satellite imagery.

Figure 4.3 illustrates this procedure near the SODA–C mooring. Considering first the broad banded ice velocities, Figure 4.3a,c shows ice velocities observed by the SODA–C ADCP (gray lines) along with ice velocities from VIIRS imagery ice tracking within 20 km of the SODA–C mooring (yellow points). Velocities fit to the VIIRS observations following Equations 4.1 and 4.2 are shown by the red lines. At SODA–C, broad banded ice velocities derived from these two methods compared well after tracking began midday on 26 July (Figure 4.3a,c). Prior to midday on 26 July, the SODA–C observed ice velocities were more complicated than simple inertial oscillations atop a subinertial background flow. In this instance, the mooring may have observed localized floe-floe collisions that did not affect the velocity of the nearby tracked floes. Such collisions could also affect the imagery-derived velocities tracked throughout the basin, decreasing the R^2 of an individual fit.

Considering the inertial part of the ice velocity, Figure 4.3 shows the ice and mixed layer averaged near-inertial velocities observed by the SODA–C mooring (gray lines), along with the inertial velocity fit to the satellite imagery (red lines). While the amplitudes and phases generally agree between the methods, this comparison highlights a limitation of the satellite-derived ice velocities: because the inertial amplitude is assumed constant during fitting, the satellite method cannot resolve the acceleration of the near-inertial ice velocities observed by the mooring.

The SODA–C mooring data show that the ice near-inertial velocity can be

treated as a proxy for the mixed layer near-inertial velocity, even when wind or internal stresses cause the broad banded ice and mixed layer velocities to differ (Figure 4.3b,d). This observation agrees with previous studies that found ice and ocean inertial oscillations were tightly coupled (Brenner et al., 2023a; McPhee, 1978) and supports our assumption that sea ice inertial velocities observed by satellites can be used to study underlying mixed layer inertial oscillations.

Hourly-fit ice velocities from satellite imagery were binned and averaged in 12 km × 12 km horizontal resolution spatial bins to create an hourly, gridded ice velocity product. When assigning ice velocity observations to spatial bins, the tracked point's geographic position at the irregular image times was linearly interpolated to hourly positions. This method of approximating the tracked point's position at unobserved times does not account for the looping motions of inertial oscillations. The radius of an inertial orbit is given by $r = U/f$; for an inertial oscillation speed U of 0.2 m s^{-1} at a latitude of 76°N, the inertial radius would be 1.5 km. This value is small relative to the bin size so the linear interpolation of tracked point positions is unlikely to result in significant mis-assignment of averaging bins.

3.3 Summary and assessment of imagery-derived inertial velocities

To summarize, ice motion was tracked in 375 m horizontal resolution grayscale images produced from the VIIRS instruments of the Joint Polar Satellite System between 26 July 12:00 UTC and 28 July 00:00 UTC 2019. Velocities from these ice trajectories were gridded in time by fitting a velocity consisting of an inertial plus a background component. Velocities along individual tracked trajectories were then

binned and averaged into 12 km spatial bins.

The average difference between the inertial speed derived from satellite imagery and available in situ observations was 0.016 m s^{-1} or 20%. These figures were calculated by comparing the average gridded imagery-derived inertial speed to the inertial speed observed by two SODA moorings and eight International Arctic Buoy Program buoys from 26 July 12:00 to 28 July 00:00. Buoys and moorings were included for comparison if any imagery-derived gridded ice velocities were available for comparison in the time range and within the nine closest grid cells (a 36 km × 36 km box) surrounding the in situ instrument. Figure 4.4 shows the location and difference in inertial speed for each in situ observation.

3.4 Near-inertial filtering

Near-inertial filtering was applied to mooring-observed ice and ocean velocities as well as slab model velocities. The near-inertial frequency band was defined as clockwise-rotating horizontal velocities with frequency magnitude between 0.9-1.1*f*. Filtering was accomplished by multiplying the complex velocities by $e^{if t}$, lowpass filtering the resulting frequency-shifted velocities with a fourth-order Butterworth filter with a cutoff frequency of 0.1*f*, and then multiplying the filtered, frequency-shifted velocities by $e^{-if t}$ to return the near-inertially filtered velocities.

3.5 Spatial autocorrelation and decorrelation scales

The autocorrelation of spatially lagged inertial speeds was used to calculate an inertial oscillation decorrelation scale for satellite-observed and slab-modeled inertial oscillation speed. Autocorrelation can be used as a measure of spatial coherence, with

values decreasing from 1 at zero lag toward or below zero at large lags. Larger autocorrelation values indicate greater coherence, and the rate at which the autocorrelation function decays defines the decorrelation scale.

To calculate the decorrelation scale for inertial oscillation speed, we assume inertial oscillation speed autocorrelation in our study region is isotropic and calculate the autocorrelation for series of data pairs that have the same spatial lag Δl. For a given spatial lag, the autocorrelation $\rho_{\Delta l}$ is given by

$$\rho_{\Delta l} = \frac{\sum_{n=1}^{N} p1'_n p2'_n}{\sqrt{\sum_{n=1}^{N}(p1'_n)^2 \ \sum_{n=1}^{N}(p2'_n)^2}} \quad 4.3$$

Here *N* is the number of data pairs, with each data pair ($p1'_n$, $p2'_n$) separated by the spatial distance Δl. The region-wide mean inertial oscillation speed $\bar{p}$ was subtracted from all values of inertial oscillation speed p to define the anomalies p'. Distances between all possible data pairs were calculated, then data pairs were discretized into 12-km spatial lag bins, with calculations performed up to separation distances of 250 km. Autocorrelation was only calculated for spatial lag bins with at least 200 data pairs.

The decorrelation scale was found by fitting a Gaussian to the observed autocorrelation function, modeling the observed autocorrelation as a function of spatial lag distance *x*

$$\rho \ = \ A \ exp\left(-\frac{x^2}{2L_x^2}\right) \quad 4.4$$

The fitting parameter *A* represents the autocorrelation at zero lag. The decorrelation

scale was defined as the fitting parameter L_x. This definition follows that used by Sumata et al. (2018) to calculate decorrelation scales for temperature and salinity in the Arctic Ocean. Other definitions of the decorrelation scale (i.e., the first zero-crossing of the autocorrelation function) are also possible, but the chosen definition is appropriate as our data were well-described by a Gaussian, with the autocorrelation function decaying toward but not crossing zero.

3.6 Coupled ice-ocean slab model

Idealized, one-dimensional "slab" models have been used to successfully simulate the mixed layer's response to surface wind stress in many studies (Pollard and Millard 1970; D'Asaro, 1985; Alford, 2020). Slab models can be adapted to include a sea ice layer (Brenner et al., 2023a; Gimbert et al., 2012a), with the ice and ocean coupled through the ice-ocean stress. Following D'Asaro's (1985) notation, we model the complex velocities $Z = u+iv$ of the sea ice Z_i and depth-averaged mixed layer Z_o as

$$\frac{dZ_i}{dt} + ifZ_i = \frac{T_{ai} - T_{io}}{d} \quad 4.5$$

$$\frac{dZ_o}{dt} + ifZ_o = \frac{T_S}{H - d} - r_o Z_o \quad 4.6$$

The right hand sides represent the action of the complex surface stresses $T = \left(\tau_x + i\tau_y\right)/\rho_o$. The stresses at each interface are defined by Equations 4.7 to 4.10 (below). The linear damping term $r_o Z_o$ represents stress within and below the mixed layer. Here f is the Coriolis parameter, d is the ice thickness, and H is the mixed layer depth.

The air-ocean stress T_{ao}, air-ice stress T_{ai}, and ice-ocean stress T_{io} were calculated using quadratic drag laws as:

$$T_{ao} = \left(\frac{\rho_a}{\rho_o}\right) C_{ao} Z_a |Z_a| \quad 4.7$$

$$T_{ai} = \left(\frac{\rho_a}{\rho_o}\right) C_{ai} Z_a |Z_a| \quad 4.8$$

$$T_{io} = C_{io}(Z_i - Z_o)|Z_i - Z_o| \quad 4.9$$

As the wind speed generally far exceeds the ice or mixed layer speed, the relative velocity was not used in the calculations of T_{ao} and T_{ai}. In mixed open water and sea ice, the total stress on the ocean surface T_s was scaled by the sea ice fraction A:

$$T_s = AT_{io} + (1 - A)T_{ao} \quad 4.10$$

For these calculations, we use a constant ice-ocean drag coefficient C_{io} of .0055, a constant ice thickness of 0.5 m, a constant mixed layer depth of 15 m, and an ocean damping coefficient of $r_o = 0.04f$ (comparable to the best fit values found by Brenner et al., 2023a and in Chapter 3 of this dissertation). The air-ocean drag coefficient C_{ao} varied with wind speed following Large and Yeager (2004) and the air-ice drag coefficient C_{ai} varied with ice concentration following Hersbach et al. (2023).

3.7 Vertical velocity from isotherm displacements

Propagating internal waves in the pycnocline generate vertical motions. These vertical velocities can be estimated from the temperature time series and background temperature gradient measured by instruments installed on the mooring. While temperature has a more complex vertical structure than density at our study site, the higher vertical resolution and shallower available depths of temperature measurements

relative to density measurements (Figure 4.8) mean that the vertical temperature gradient is better resolved. Thus, we are better able to estimate the vertical motion of isotherms than of isopycnals.

At the timescales considered here (< 2 weeks), we assume there is a steady background vertical temperature gradient at the mooring site. This implies that there is no vertical or horizontal mixing, and that there is no horizontal variation in the temperature gradient so that it is unaffected by advection. Under these assumptions, the observed temperature variation $\frac{\partial T(t)}{\partial t}$ is due to vertical motion *w* of the temperature field relative to the instrument

$$\frac{\partial T(t)}{\partial t} = w(t)\frac{\partial T}{\partial z} \qquad 4.11$$

Here *w* includes contributions from the instrument itself moving up and down, and from the vertical motion of the water column. The instrument's vertical velocity can be calculated from its recorded pressure variations and removed. Rearranging Equation 4.11 gives

$$w(t)_{water\ column} = \frac{\partial T(t)}{\partial t}\left(\frac{\partial T}{\partial z}\right)^{-1} - \frac{\partial z(t)_{instrument}}{\partial t} \qquad 4.12$$

Thus, the vertical velocity of the water column at an instrument's (potentially varying) depth can be calculated using the temperature time series $\frac{\partial T(t)}{\partial t}$ observed by that instrument, the observed instrument vertical velocity $\frac{\partial z(t)_{instrument}}{\partial t}$ induced by vertical motions of the mooring line, and a time-averaged background temperature gradient $\frac{\partial T}{\partial z}$ calculated using observations from neighboring temperature sensors

installed on the mooring.

3.8 Inertial pumping

Inertial pumping at the mixed layer base, caused by the divergence of purely horizontal inertial oscillations, generates vertical velocities in the stratified transition layer below the mixed layer. Expected vertical velocities *w(z)* can be calculated by depth integrating the horizontal convergence of mixed layer near-inertial currents Z_{NI} (D'Asaro, 1989) as

$$w(z) = -\int_0^z \nabla_H \cdot Z_{NI}\, dz \qquad 4.13$$

The expected vertical velocity at SODA–C was calculated using the 12 km gridded near-inertial velocities derived from VIIRS imagery.

4 Results

4.1 Beaufort Sea near-inertial ice velocity structure

On 19 July 2019, a cyclone moved northward through the Beaufort Sea. Clockwise rotating winds developed along the storm's eastern flank as it parallelled the mooring array (Figure 4.5a), with the low pressure center located west of the moorings. The low pressure system then remained in the northern Beaufort Sea on 20 and 21 July 2019, creating westerly and southwesterly winds in the study region (Figure 4.5c). Regionwide, maximum ERA5 wind speeds exceeded 10 m s^{-1} (Figure 4.5a), and the maximum ERA5 wind speed at the SODA–C mooring was 10 m s^{-1} (Figure 4.2b). At the SODA–C mooring, the clockwise turning of the wind was particularly evident in the rapid change in sign of the zonal component on 19 July (Figure 4.2b). A second

cyclone with wind speeds up to 20 m s^{-1} transited eastward across the southern Beaufort Sea on 20-21 July (Figure 4.5c); the resonant, clockwise-rotating winds caused by that storm were mostly restricted to the southern open water region between the coast and the ice edge.

Moorings and Lagrangian buoys throughout the Beaufort Sea demonstrate regional variation in the strength and timing of inertial speeds in the days following the storm (Figure 4.4c). Some instruments showed one peak in inertial speeds after 20 July, while others showed a second acceleration of near-inertial speed around 24 July. At the SODA–C mooring, the sea ice and ocean mixed layer oscillated in unison with closely matched amplitude and phase immediately following the storm (Figure 4.2e). The near-inertial ice and mixed layer speeds reached 0.15 m $s^{-1}$and 0.14 m s^{-1}, respectively, on 21 July (Figure 4.2e).

The relatively large horizontal spacing of the available in situ observations makes regional patterns in inertial oscillation speed difficult to interpret (Figure 4.4a,c), but velocities derived from satellite imagery can be used to map the spatial structure of the inertial oscillations. The satellite-derived inertial ice speeds, which result from the fitting procedure described in Chapter 4.3.2, show the horizontal structure of the sea ice's inertial oscillations (Figure 4.6a,c). The primary feature of the near-inertial ice velocity field was an area of faster oscillations extending southward and eastward from the SODA–C mooring. This region, which measured approximately 120 km meridionally and 300 km zonally, had near-inertial ice speeds that exceeded 0.2 m s^{-1}.

The magnitudes of the northward and eastward components of ice inertial

velocity showed some differences in regional structure. Maps of inertial velocities three hours (about a quarter inertial period) apart highlight changes in inertial speed coincident with a transition from velocities directed along one horizontal axis to a perpendicular axis (Figure 4.6a,c). Inertial orbits are elliptical where such differences are present. This ellipticity can be quantified as the ratio of the ellipse minor axis length to the major axis length, with this ratio decreasing for increasing ellipticity.

Orbital ellipticity varied throughout the study area, with a notable region of more elliptical orbits found west of SODA–C (Figure 4.6e). While super-inertial frequencies can cause elliptical orbits, VIIRS velocities were assumed inertial in the fitting procedure. It is instead possible that the orbital ellipticity reflects preferential orientation of internal ice stresses, leading to asymmetrical damping of inertial oscillations. The region of increased ellipticity west of SODA–C (Figure 4.6e) coincided with regions of decreased inertial oscillation speed (Figure 4.6a,c) and increased sea ice concentration (Figure 4.4a), supporting the idea that internal stresses restricted inertial motion.

4.2 Inertial oscillation decorrelation scales

The observed basin-wide inertial oscillation speed decorrelation scale was approximately 65 km. This result was computed using the hourly, 12 km gridded maps of imagery-derived inertial oscillation speed. To illustrate this calculation, Figure 4.6c,d shows the calculated autocorrelation as a function of spatial lag between paired observations on 27 July 2019 at 00:00 UTC and 03:00 UTC (Equation 4.3), along with the Gaussian fits defining the decorrelation scales at those times (Equation 4.4). This

calculation was repeated for each imagery-derived hourly map from 26 July 12:00 to 28 July 00:00 UTC, then temporally averaged. There was some temporal variability in the calculated decorrelation scale, which ranged from 51-73 km over this time period. This variability may be due to differing strengths of eastward and northward velocities, which cause changing patterns of overall inertial speed throughout an inertial period, and differing spatial bins with available data at a given timestep (related to local cloudiness). Restricting the autocorrelation calculations to a 500 km × 500 km region encompassing the strong inertial response along 140°W reduced the time-averaged decorrelation scale somewhat, to 56 km.

The change in inertial oscillation horizontal structure that occurred between the storm's passage and the cloud-free satellite imagery measures the reduction of inertial oscillation scales over time. Ice motion tracking cannot be used to study this temporal evolution because the region was cloud-covered during and immediately following the storm. Instead, the horizontal structure generated by the storm can be estimated using a slab model.

A slab model was run at each ERA5 grid point in the study region. The slab model was initiated on 16 July 2019 and forced with that ERA5 grid point's time-varying wind and sea ice concentration. A spatially and temporally constant mixed layer depth of 15 m was assumed; the mooring-observed mixed layer depth averaged from 19 to 25 July 2019 was 15 m at SODA–A, 15 m at SODA–B, and 14 m at SODA–C. Figure 4.2e shows that the slab model reproduced the generation of ice and ocean near-inertial currents well at SODA–C until 24 July 2019. Figure 4.5d compares slab-

modeled inertial speeds to those observed by moorings and Lagrangian buoys throughout the Beaufort Sea. The average difference in inertial speed between the model and observations on 20 and 21 July was 0.04 m s^{-1}. While imperfect, this difference is smaller than region-wide gradients in inertial speed, so we proceed with the assumption that the slab model can predict the region-wide structure of inertial oscillation speed. Possible reasons for observation-model differences are discussed in Chapter 4.5.1.1.

The structure of mixed layer inertial oscillation speed generated by the slab model was reminiscent of the structure of sea ice oscillation speed later observed in the satellite imagery (Figure 4.5d), indicating that the structure of the wind field played a primary role in setting the structure of the inertial response. The model predicted inertial oscillations with speeds up to 0.2 m s^{-1} in a region nearby to and south of the SODA–C mooring. This patch of elevated inertial speeds roughly corresponds to the location of elevated inertial speeds found in satellite imagery (Figure 4.6c,d). The model also predicted very strong inertial oscillations west of the SODA–B mooring; satellite-derived inertial speeds were also elevated in this region, though the spatial coverage of satellite-derived ice velocities in this region was limited by the ice edge (Figure 4.4a), with no tracking possible in open water. Finally, the model predicted strong oscillations along the track of the second storm in the open water south of the ice edge (Figure 4.5d), where no ice tracking was possible due to the lack of ice. Modeled mixed layer, rather than sea ice, near-inertial speed is shown as it enables a basin-wide picture of modeled inertial oscillation behavior.

To estimate the spatial scales at which the storm excited inertial oscillations in the ice and mixed layer, we calculated the decorrelation scale of slab modeled inertial oscillation speed. Prior to this calculation, slab model results were interpolated from the ERA5 grid to the same 12 km × 12 km grid onto which ice tracking results were gridded. At the latitude of the SODA–C mooring, ERA5 grid cells measure approximately meridionally 28 km and 6 km zonally. Slab model results were subsampled at the same geographic bins as had satellite-derived ice velocity data on 27 July 00:00 UTC, then autocorrelations of pairs of spatially lagged slab model results were calculated. Averaged on 20 and 21 July, the decorrelation length scales for slab model inertial oscillation speed were 102 km and 103 km for the sea ice and mixed layer, respectively, reflecting the tight coupling of oscillations in both media.

4.3 Subinertial ice velocities

Shifting focus from inertial oscillations, subinertial velocities were also fit to the ice trajectories derived from satellite imagery. Figure 4.7 shows the 12 km gridded subinertial ice velocities averaged on July 26 and on July 27, compared to ice velocities from Polar Pathfinder, a daily gridded ice motion product derived from a wide variety of sensors and drifting buoys (Tschudi et al., 2019). Regional patterns in ice speed and direction generally agreed between the two products, giving further confidence in the ice tracking method developed here. Ice velocities derived here from the VIIRS imagery show some mesoscale structure that was not present in the lower resolution 25 km Polar Pathfinder product. Understanding these small-scale structures in ice velocity, which may reflect a combination of local wind forcing, internal ice stresses,

and mesoscale mixed layer features, is outside the scope of the current study, but would be a fruitful use of ice velocity fields extracted from similar satellite imagery in the future.

4.4 Internal wave generation at SODA–C

We now focus on internal wave generation at the SODA–C mooring. Figure 4.2 provides an overview of temperature and velocity observed at the mooring site during the study period. The water column structure consisted of a recently formed, 15 m deep summer mixed layer on top of the remnant cold winter mixed layer, which occupied the depth range of roughly 20-35 m (Figure 4.2d). The shallowest salinity data were collected at 38 m, so the mixed layer depth was determined from ADCP backscatter and inertial shear rather than direct density measurements (Brenner et al., 2023b). Thus, the strength of the stratification in the newly formed pycnocline directly beneath the summer mixed layer cannot be determined. The perennial thermocline atop the temperature maximum of the Pacific Summer Water layer began at around 35 m (Figure 4.2d). The mean vertical temperature and density profiles at the mooring, averaged from 18 July to 1 August 2019, are shown in Figure 4.8.

Within the mixed layer, vertical bands of alternating current direction show inertial oscillations after 20 July (Figure 4.2c). The strength of mixed layer average inertial oscillations initially peaked on 21 July and then decayed over several days, with the ice oscillating more slowly than the mixed layer after 23 July (Figure 4.2e). On 25 July 2019, the near-inertial ice and ocean velocities at SODA–C accelerated to a second peak (Figure 4.2e) The second peak's maximum ice and mixed layer near-inertial

speeds, which occurred about a week after the first event's peak, were the fastest observed throughout the annual mooring record (Figure 4.1). The maximum near-inertial ice speed was 0.20 m s^{-1} on 29 July 2019 (Figure 4.2e). Mixed layer velocities were in phase with the ice but slightly slower at the event's apex, peaking at 0.15 m s^{-1} on 27 July 2019 (Figure 4.2e). Unlike the first peak in near-inertial velocities, which were forced by the 19 June cyclone, the second acceleration of near-inertial velocities at SODA–C occurred during a period of high atmospheric pressure (not shown). ERA5 showed easterly winds accelerated late on 25 July, around the time the mooring-observed near-inertial speeds increased (Figure 4.2b).

The inertial-frequency velocity bands deepened in the days following the storm, indicating accelerating near-inertial currents in the pycnocline (Figure 4.2c). Near-inertial horizontal kinetic energy ($HKE_{NI} = \frac{1}{2}\rho_0|Z_{NI}|^2$), depth integrated from the mixed layer base to the deepest ADCP bin at 66 m, remained steady until 25 July, then more than doubled to a maximum of 24 J m^{-2} on 27 July 2019 (Figure 4.9). WKB scaling, which can account for the refraction of internal waves propagating through varying stratification, was not applied prior to these calculations as stratification was not observed in the upper pycnocline. This simplification will mostly affect the magnitude of calculated near-inertial horizontal kinetic energy rather than trends over time or the relative energy contained in upward- and downward-propagating components.

Pycnocline velocities can be decomposed into upward- and downward-propagating components on the basis of the sign of the vertical wavenumber k_z. For

anticyclonic rotation (negative frequency), positive k_z corresponds to downward phase propagation and upward energy propagation, whereas for cyclonic rotation positive k_z corresponds to downward energy propagation (Pinkel, 2008). To separate upward- and downward-propagating motions in the mooring observations, ADCP data were 2D Fourier transformed, filtered to retain only the upward or downward propagating quadrants, then inverse transformed to return the upward or downward propagating (broadband) velocity. The results were then inertially filtered.

Downward-propagating near-inertial horizontal kinetic energy in the pycnocline increased after 23 July, while upward-propagating near-inertial kinetic energy was minimal throughout the study (Figure 4.9e), confirming that the observed pycnocline waves were surface forced. Low vertical wave numbers were dominant; in the discretization required to perform the Fourier transform, there was significant energy in a k_z=0 bin. This bin does not represent truly non-propagating energy with zero vertical wavenumber, but rather reflects the modest ADCP depth range which limited the smallest permitted value of k_z. Vertical propagation direction cannot be determined for this low wavenumber energy, which was the dominant contributor to the total depth-integrated near-inertial HKE at most times (Figure 4.9e).

In addition to the horizontal near-inertial velocities used in the above HKE calculations, propagating internal waves also produce vertical velocities. The vertical velocity of the water column at SODA–C was calculated from mooring-observed temperatures using Equation 4.12. At 38 m, near the top of the thermocline, near-inertial vertical velocities remained below 0.4×10^{-4} m s^{-1} before 25 July, then increased

to a maximum speed of 1.6×10^{-4} m s^{-1} (Figure 4.11). Time-integrating the mooring-observed near-inertial vertical velocity gives maximum internal wave amplitudes of 1.1 m. The near-inertial vertical velocities calculated from the mooring-observed temperature time series were sensitive to the time bins into which temperature observations were averaged prior to inertial filtering; binning temperature observations into 1-hour bins resulted in maximum near-inertial internal wave amplitudes of 1.3 m, while binning temperature observations into 3-hour bins resulted in maximum internal wave amplitudes of 0.8 m.

The observed vertical velocities can be compared against those predicted from inertial current divergence. Figure 4.10 shows the 12 km gridded satellite-derived near-inertial velocity and velocity divergence in an approximately 200 km region around the SODA–C mooring. The horizontal gradients in inertial current speed, along with regional variation in inertial current direction, led to alternating convergences and divergences as the current vectors rotated through an inertial period. The absolute value of divergence was order 10^{-6} s^{-1} (Figure 4.10b,d), about an order of magnitude larger than observed in SAR imagery by Kwok et al. (2003), though their data were averaged over several weeks with variable wind and inertial oscillation speeds. Inertial current divergence averaged in a 36 km region surrounding the mooring was depth-integrated from the surface to 38 m following Equation 4.13 to predict the vertical velocities generated by this inertial pumping. When imagery-derived ice velocities were available, the expected vertical velocity at the mooring site reached speeds of up to 0.6×10^{-4} m s^{-1} (Figure 4.11), corresponding to near-inertial internal wave amplitudes of

0.5 m.

When calculating inertial pumping, we assume that the near-inertial ice velocities derived from the satellite imagery can be used as a proxy for the underlying near-inertial mixed layer velocities. Comparing the SODA–C mooring-observed ice and mixed layer velocities suggests this assumption may underestimate the magnitude of mixed layer inertial oscillations and pycnocline vertical velocities on 26-27 July, when mooring near-inertial mixed layer speeds exceeded near-inertial ice speeds (Figure 4.2e). After 28 July, SODA–C near-inertial ice speeds exceeded near-inertial mixed layer speeds (Figure 4.2e).

5 Discussion

5.1 Processes underlying decreasing inertial oscillation length scales

Comparing the inertial oscillation speed decorrelation scale computed from slab model results immediately following the storm (~100 km) to the satellite-derived decorrelation scale computed roughly one week later (~65 km) suggests a reduction in inertial oscillation scales over this time period. Such a reduction is required for internal waves to efficiently radiate energy away from the mixed layer (D'Asaro et al., 1995; Gill, 1984).

Here we discuss processes in the atmosphere, sea ice, and ocean mixed layer that could establish the scale of inertial oscillations. These processes can further be divided into those that influenced the initial scales of mixed layer inertial oscillations at the time of generation, as simulated by the slab model, and those that affected the evolution or decay of inertial oscillations until the time of satellite-derived ice velocity

observations.

5.1.1 Uncertainties in the slab model

While the slab model performed well at the SODA–C mooring, within the core region of strong inertial oscillations observed in the satellite imagery, its performance elsewhere in the Beaufort Sea was mixed (Figure 4.5d). Unmodeled processes that could lead to energy injection scales that differed from those predicted by the slab model are discussed next.

The first reason that the slab model could produce over-large inertial oscillation scales at the time of the storm is due to inaccuracies in the reanalysis wind field. Mesoscale atmospheric features can be important for sea ice deformation and air-ice-ocean momentum flux (Brümmer and Hoeber, 1999; Guest et al., 1995; Persson et al., 2023; Watkins et al., 2024). Watkins et al. (2024) studied a mid-winter Arctic cyclone and found that a mesoscale low-level atmospheric jet structured the inertial response of the ice and ocean. However, correlations between observed winds and ERA5 in the Arctic are generally high (Graham et al., 2019). During the event studied here, the location of the wind front in ERA5 aligned well with the cold front in concurrent satellite imagery (Figure 4.5a,b), giving confidence in the wind field in the reanalysis.

A second possibility is that internal stresses in the ice pack, which were not included in the slab model, modified the generation of inertial oscillations. Inertial oscillations in the Beaufort Sea were significantly damped at sea ice concentrations above 0.85 (Brenner et al., 2023a), a proxy for times when internal stresses make a significant contribution to the sea ice momentum balance. Most of the study region had

AMSR2 ice concentrations below 0.85 (Figure 4.4a), meaning internal ice stresses were not expected to damp inertial oscillations in those areas. However, notable exceptions were found in southward-reaching tongues of high ice concentration roughly coincident with the lower inertial oscillation speed bands along approximately 132°W and 144°W (Figure 4.4a, Figure 4.6a). Focusing on the region around SODA–C, zonally increasing near-inertial speeds roughly aligned with a zonal decrease in sea ice concentration on 25 July (Figure 4.10a,c; Figure 4.12b,c). However, AMSR2 ice concentration was more uniform around SODA–C on 20 July (Figure 4.12a), meaning that a gradient in internal stresses was unlikely to create a gradient in inertial oscillation speed *at the time of generation*. The change in ice concentration near SODA–C over time, and its potential implications *for the evolution* of inertial oscillations, is discussed in Chapter 4.5.1.2.

A final unmodeled process is regional variation in mixed layer depth, which was assumed spatially invariant on the basis of consistent mixed layer depths observed across the SODA mooring array. Shallower mixed layers concentrate near-inertial energy in a thinner "slab" and, in the slab model, mixed layer inertial oscillation speed depends on mixed layer depth (Equation 4.6). Concurrent mixed layer depth measurements from platforms other than the SODA mooring array are limited. Several weeks later, on 14 August 2019, profiles collected by the Seasonal Ice Zone Reconnaissance Surveys (SIZRS) program along 150°W between 72°N and 77°N had mixed layer depths ranging from 11-14 m, defined as a density change of 0.1 kg m^{-3} relative to the density at 5 m (Peralta-Ferriz and Woodgate, 2015). Based on the available observations, mixed layer depth at the time of our study appears relatively

uniform across the Beaufort Sea and in line with the assumed mixed layer depth used in the slab model.

Despite the uniformity of the sparsely observed basin-wide mixed layer depth, it is notable that, at SODA–C, the mixed layer shoaled to 15 m from the bottom of the cold winter mixed layer at around 40 m on 18 July, just days before the storm considered in this study. The recent mixed layer shoaling at SODA–C was presumably due to freshening by local ice melt, though lacking mixed layer salinity measurements this hypothesis cannot be directly tested. Regional variation in ice concentration could reflect varying amounts of ice melt, restratification and mixed layer shoaling, as well as the effects of ice advection. If present, weaker stratification and deeper mixed layers in areas of higher ice concentration would compound the damping effect of internal ice stresses on inertial oscillation speed.

5.1.2 Evolution of inertial oscillations from generation to satellite observation

The slab model is better suited to simulating inertial oscillation generation than evolution. The model employs a simple, linear damping term to simulate mixed layer inertial oscillation decay (Equation 4.6), standing in for various physical processes including internal wave radiation, mixed layer deepening, and boundary layer turbulence. While the slab model replicated SODA–C near-inertial velocities and their decay well until 24 July, it performed poorly after that time, with modeled near-inertial ice and mixed layer speeds being slower than and out of phase with mooring observations (Figure 4.2e). The slab model's poor performance at this time means it cannot be used to investigate the evolution of the horizontal structure of inertial

oscillations until VIIRS imagery observed the inertial oscillation scales.

If we assume that the slab model was able to simulate the inertial oscillation field well enough to qualify the typical length scales of inertial oscillation coherence *at the time of generation*, while acknowledging that the aforementioned unmodeled processes might contribute to local differences between the model and observations, we can conclude that the inertial oscillation field evolved toward smaller length scales in the week following the storm. We next consider processes that might contribute to this evolution.

Through a process known as β-refraction, variation in *f* with latitude can reduce the meridional wavenumber of inertial oscillations over time (D'Asaro, 1995). β-refraction reduces the scales of inertial oscillations by producing oscillations of latitudinally-varying frequency which eventually oscillate out of phase with each other, producing divergence. At SODA–C, the observed near-inertial divergence is due in large part to a zonal gradient in speed rather than a meridional gradient in phase (Figure 4.10a,c), thus having little in common with the theoretical current structure that would be produced by β-refraction. While the decorrelation scale calculated here is not directly comparable to a meridional wavenumber, the theoretical meridional wavenumber is $k_{y0} - \beta t$ (D'Asaro et al., 1995). Assuming an initial meridional wavenumber k_{y0}= 0, at SODA–C's latitude of ~78°N, the absolute value of the meridional wavenumber k_y would be expected to decrease to 3×10^{-6} m^{-1} in a week, equivalent to a wavelength $\lambda_y = 2\pi/k_y$ of 2,200 km. This value is much larger than the observed inertial oscillation scales, meaning β-refraction cannot explain our

observations.

In a process similar to β-refraction, vertical vorticity caused by mixed layer currents can also reduce mixed layer inertial oscillation scales. This process, called ζ-refraction, essentially creates gradients in f_{eff} that dephase inertial oscillations and very efficiently radiate near-inertial energy from the mixed layer into the pycnocline (Asselin et al., 2020; Thomas et al., 2023). However, ζ-refraction is unlikely to be a primary means through which inertial oscillation scales decreased in our data. While mesoscale eddies are commonly found in the Arctic halocline, they are not common in the Arctic mixed layer under ice and away from the ice edge, likely due to frictional spin-down in the ice-ocean boundary layer (Manley and Hunkins, 1985; Manucharyan et al., 2022; Ou and Gordon, 1986; Zhao et al., 2014). The SODA–C mooring record does not show any mixed layer mesoscale eddies during our study period (Figure 4.2c). While the satellite-derived subinertial ice velocity showed lateral current shear (Figure 4.7b,d), ice velocity cannot be taken as a passive tracer of mixed layer velocities at subinertial frequencies due to wind-driven ice drift. Lacking additional observations of mixed layer currents, we defer to past studies and assume that, under ice and away from the ice edge, there were few mixed layer eddies or strong gradients in the background flow.

Finally, it is possible that spatially and temporally varying internal stresses in the ice pack could change the rate at which inertial oscillations were damped. In the summer-type ice pack that we consider here, subinertial ice divergence could, over several inertial periods, compact the ice atop pre-existing mixed layer inertial currents.

Such an increase in ice concentration could increase internal stresses, damping out inertial oscillations in the sea ice. Given the tight coupling between ice and mixed layer velocities within the inertial frequency band, ice-ocean drag caused by differences between the mixed layer inertial velocity and damped ice inertial velocity could then slow oscillations in the higher-inertia mixed layer.

Assuming high ice concentrations are a proxy for more active internal stresses, we consider the spatial gradient in inertial oscillation speed near SODA–C and its relationship to ice concentration in more detail. AMSR2 shows that the sea ice concentration decreased in the east of SODA–C between 20-25 July 2019 (Figure 4.12a,b). The decrease in sea ice concentration east of the mooring is likely due to local redistribution of sea ice rather than large-scale advection. ERA5 winds averaged from 20-25 July 2019 were southwesterly and divergent on the east side of the mooring. The region of wind divergence coincides with the region of decreasing ice concentration (Figure 4.12b,d), suggesting the ice pack spread out in response to surface forcing. Integrated ice motion vectors from Polar Pathfinder showed ice in the study region moved an average of 27 km from 20 to 25 July (Figure 4.12a,b), a distance that precludes large-scale advection of the ice pack from causing the decrease in ice concentration. The persistence of compact ice west of the mooring could more rapidly damp ice and mixed layer inertial oscillations, while the loosening of ice east of the mooring could allow the ice and mixed layer oscillations to persist uninhibited. Conceivably, this effect could sharpen gradients in inertial oscillation speed already imposed by the strength and resonance of the wind at the time of generation.

5.2 Inertial oscillation coherence and internal wave generation

The SODA–C mooring observed near-inertial internal wave generation following the storm, evidenced by increased depth-integrated pycnocline near-inertial horizontal kinetic energy and increased vertical velocity at the base of the remnant winter mixed layer. The amplitude of these mooring-observed internal waves was about 1 m, though the estimate is somewhat dependent on details of the calculation. This amplitude is typical of Beaufort Sea internal waves at this latitude (Dosser and Rainville, 2016). The dominant frequency of the vertical velocity from 25-29 July was about 1.1*f*, with super-inertial frequencies required for internal waves to propagate.

Depth-integrating the divergence of imagery-derived inertial velocity underestimated internal wave amplitude by more than a factor of two relative to that estimated from the mooring temperature time series. However, this result was also sensitive to details of the calculation. For example, decreasing the gridding resolution for ice trajectories, or decreasing the radius around the mooring in which divergence was averaged, increased the estimated internal wave amplitude. There was also a frequency mismatch between these methods, as the dominant frequency of the divergence was itself inertial. Given the sensitivities of the internal wave amplitude calculations, it is difficult to directly compare the methods. However, it is promising that the imagery tracking method produced inertial velocity divergence of the right overall magnitude, suggesting that applying this method to a large set of images might help identify internal wave generation hotspots in the Arctic.

5.3 Discussion summary

While the possibility cannot be eliminated, we do not expect errors in the reanalysis wind field caused significant inaccuracies in the decorrelation length scales calculated from the slab model. In addition, the limited in situ observations show no evidence of substantial mixed layer depth spatial heterogeneity at the time of inertial oscillation generation, meaning our assumption of spatially constant mixed layer depth in the slab model is reasonable. With these assumptions, the slab model results show that regional patterns in the strength and resonance of the wind field caused patterns of modeled inertial oscillation strength that had much in common with the inertial oscillation field observed in VIIRS satellite imagery about a week later. Thus, as expected, the wind field played a primary role in setting the overall structure of the inertial oscillation field.

Focusing on processes that could have reduced the inertial oscillation scales by ~30% over about a week, we do not expect two processes that have been important in other studies in ice-free regions, namely β-refraction and ζ-refraction, to be of primary importance here. Rather, we expect that sea ice is primarily responsible for reducing inertial oscillation scales from those imposed by the atmosphere. Spatial variability in internal ice stresses is the most likely factor in modifying the ice and mixed layer inertial oscillation scales. Gradients in internal stress could impact the initial generation strength of inertial oscillations for a given wind forcing. Changing spatial patterns of internal stresses could also impact the evolution of inertial oscillations. Such a process may be suggested by a diverging ice pack in the region around SODA–C, where lower

ice concentrations were found in areas of higher observed inertial oscillation speed. However, given the large number of unobserved variables, the results presented here are best viewed as motivation for further research rather than strong evidence supporting a single process reducing inertial oscillation scales in the summer ice pack.

6 Summary and conclusion

This study mapped basin-wide sea ice inertial oscillations in the ice-covered Beaufort Sea in July 2019, deriving inertial ice velocities from more than 29,000 points tracked in high temporal resolution satellite imagery. These ice-derived velocities, which were validated against Lagrangian buoys and mooring data, provide an unprecedented view of the spatial structure of inertial oscillations a week after the passage of two cyclones. Very few studies have considered the spatial structure of inertial oscillations in the Arctic (but see Watkins et al. (2024) for discussion of a dense network of buoys in a roughly 100 km x 100 km region in the Arctic, and Hutchings et al. (2012) for a dense 70 km triangular buoy array in the Antarctic). While large-scale drifter experiments are more commonly used to study inertial oscillations outside of the Arctic (e.g., Chaigneau et al., 2008; D'Asaro et al., 1995; Elipot et al., 2010), our approach of using sea ice as de facto Lagrangian drifters generated a map of inertial oscillations that is distinguished by its simultaneously large geographic range and dense horizontal resolution.

About a week after assumed generation, inertial oscillation coherence scales were about 65 km, smaller than predicted by a slab model forced by reanalysis wind at the time of the storm. Neither β-refraction nor ζ-refraction appeared to be primary

factors in the apparent reduction of inertial oscillation scales. Instead, we hypothesize that spatial gradients in sea ice characteristics are the most likely drivers of the reduction in inertial oscillation scales. Gradients in internal ice stresses could create gradients in inertial oscillation speed at their time of generation or could create spatial gradients in the rate of inertial oscillation decay. At the SODA–C mooring, a location that was considered in detail in this study, wind-driven subinertial sea ice divergence may have allowed oscillations to persist in areas with lower ice concentration while damping them in regions with higher ice concentration.

Mooring observations showed that internal waves with amplitudes of approximately 1 m were generated by this event. Depth-integrated near-inertial velocity divergence calculated from satellite imagery predicted internal waves with amplitudes that were about a factor of two smaller than the mooring observations, although there were substantial uncertainties associated with both methods. Internal wave generation is a key pathway for redistributing energy from the atmosphere through the sea ice and ocean mixed layer to the Arctic Ocean's stratified interior. At present, internal waves in ice-covered waters must be detected by sparsely distributed instruments that directly observe the pycnocline. Our results demonstrate that internal wave generation events might be detected from the divergence of satellite-observed near-inertial ice velocities. Even if the magnitude of generated waves cannot be precisely determined, this method could guide future observational efforts by identifying key regions or seasons of enhanced internal wave generation.

This study underscores the challenges of studying episodic internal wave

generation posed by the sparse spatial coverage of available in situ observations, as the existing buoy network cannot resolve the horizontal scales of inertial oscillations observed here. While satellite imagery provided adequate horizontal resolution, cloud cover inhibited continuous ice motion tracking so inertial oscillation evolution and decay could not be studied in detail. Nonetheless, the combined use of mooring and buoy data, satellite-derived ice velocities, and idealized modeling enabled an analysis of inertial oscillations from storm-forced generation to internal wave radiation. Future studies should employ a network of Lagrangian drifters deployed with order 30-60 km horizontal spacing, or cloud penetrating high temporal resolution satellite imagery, to better capture the temporal and spatial evolution of inertial oscillations. Such an observational network would resolve uncertainties related to our use of a slab model to estimate the rate at which inertial oscillation coherence scales were reduced.

As Arctic sea ice cover continues to change, it is essential to understand the dynamics controlling individual internal wave generation events so that energetic waves punctuating a quiescent background are accurately predicted. While ongoing changes in the Arctic ice pack will likely continue to increase near-inertial energy in the sea ice and mixed layer (Brenner et al., 2023a; Gimbert et al., 2012b; Rainville and Woodgate, 2009), the impacts on the interior internal wave field have been, in many ways, more mixed, surprising, and unintuitive. The partitioning of mixed layer near-inertial energy between turbulent deepening of the mixed layer and internal wave radiation determines if energy dissipation and mixing occur near the surface or in the ocean interior. This balance has implications for the Arctic's heat and salt budgets, as

well as for nutrient distribution, potentially impacting marine ecosystems. Accurately predicting the fate of mixed layer near-inertial energy is therefore essential for predicting future Arctic conditions.

7 Acknowledgments

This research was funded through the Office of Naval Research (Laura Crews, Craig Lee, Luc Rainville) and the National Science Foundation (LC). The SODA project, including the collection and analysis of the data presented here, was funded by ONR grant N00014-14-1-2377 (CL, LR). Data analysis and synthesis were also supported by ONR grant N00014-18-1-2694 (LC). This material is based upon work supported by the National Science Foundation Graduate Research Fellowship Program under Grant DGE-1762114 (LC). Any opinions, findings, and conclusions or recommendations expressed in this material are those of the author(s) and do not necessarily reflect the views of the National Science Foundation.

The satellite image processing methods used in this project were largely developed during my participation in the 2023 OceanHackWeek workshop. In particular, I am grateful to my OHW project team of Alex Kerney, Myranda Shirk, Colin Sauze, Dalton Sasaki, Michael Cappola, and Aditya Sharma for following me into the mystifying labyrinth of satellite image processing and producing working code by the end of the week. I deeply appreciate the discussions with Jennifer Hutchings, Daniel Watkins, and Tim Stanton that developed many of the ideas presented here.

8 Data availability statement

VIIRS Level1b data are available from NASA's Earthdata Search portal at https://search.earthdata.nasa.gov/search?q=VIIRSandfl=1B%2B-%2BRadiance%252C%2BSensor%2BCoordinates

ADCP ocean velocity measurements, temperature and salinity observations, and mixed layer depth for the full deployments of the SODA moorings are available at http://hdl.handle.net/1773/49495

International Arctic Buoy Program buoy data are available at https://iabp.apl.uw.edu/WebData/

ERA5 reanalysis (Hersbach et al., 2023) is available at https://doi.org/10.24381/cds.adbb2d47

Daily NSIDC Polar Pathfinder sea ice drift (Tschudi et al., 2019) is available at https://nsidc.org/data/nsidc-0116/versions/4

AMSR2 sea ice concentration (Spreen et al., 2008) is available at https://seaice.uni-bremen.de/sea-ice-concentration/amsre-amsr2/

Hydrographic profiles collected by the Seasonal Ice Zone Reconnaissance Surveys (SIZRS) program are available at https://psc.apl.uw.edu/research/projects/sizrs/data-2/

9 References

Alford, M. H. (2020). Revisiting near-inertial wind work: Slab models, relative stress, and mixed layer deepening. *Journal of Physical Oceanography*, 50 (11), 3141–3156. doi:10.1175/JPO-D-20-0105.1

Alford, M. H., and Whitmont, M. (2007). Seasonal and spatial variability of near-inertial kinetic energy from historical moored velocity records. *Journal of Physical Oceanography*, 37, 2022–2037. doi:10.1175/JPO3106.1

Asselin, O., L. N. Thomas, W. R. Young, and L. Rainville (2020): Refraction and Straining of Near-Inertial Waves by Barotropic Eddies. *Journal of Physical Oceanography*, 50, 3439–3454, doi:10.1175/JPO-D-20-0109.1

Brenner, S., Rainville, L., Thomson, J., Cole, S., and Lee, C. (2021). Comparing observations and parameterizations of ice-ocean drag through an annual cycle across the Beaufort Sea. *Journal of Geophysical Research: Oceans*, 126 (3), e2020JC016977. doi:10.1029/2020JC016977

Brenner, S., Thomson, J., Rainville, L., Crews, L., and Lee, C. (2023a). Wind driven motions of the ocean surface mixed layer in the western Arctic. *Journal of Physical Oceanography*, 53 (7), 1787–1804. doi:10.1175/JPO-D-22-0112.1

Brenner, S., Thomson, J., Rainville, L., Torres, D., Doble, M., Wilkinson, J., and Lee, C. (2023b). Acoustic sensing of ocean mixed layer depth and temperature from uplooking ADCPs. *Journal of Atmospheric and Oceanic Technology*, 53–64. doi:10.1175/JTECH-D-22-0055.1

Brümmer, B., and Hoeber, H. (1999). A mesoscale cyclone over the Fram Strait and its effects on sea ice. *Journal of Geophysical Research: Atmospheres*, 104 (D16), 19085–19098. doi:10.1029/1999JD900259

Cao, C., Xiong, X., Wolfe, R., DeLuccia, F., Liu, Q., Blonski, S., Lin, G., Nishihama, M., Pogorzala, D., Oudrari, H., and Hillger, D. (2017). *Visible Infrared Imaging Radiometer Suite (VIIRS) sensor data record (SDR) user's guide, version 1.3* (NOAA Technical Reports). U.S. Department of Commerce, National Oceanic and Atmospheric Administration, National Environmental Satellite, Data, and Information Service. Washington, D.C. https://ncc.nesdis.noaa.gov/documents/documentation/viirs-users-guide-tech-report-142a-v1.3.pdf

Chaigneau, A., Pizarro, O., and Rojas, W. (2008). Global climatology of near-inertial current characteristics from Lagrangian observations. *Geophysical Research Letters*, 35 (13). doi:10.1029/2008GL034060

Chanona, M., Waterman, S., and Gratton, Y. (2018). Variability of internal wave-driven mixing and stratification in Canadian Arctic shelf and shelf-slope waters. *Journal of Geophysical Research: Oceans*, 123 (12), 9178–9195. doi:10.1029/2018JC014342

Cole, S. T., Toole, J. M., Rainville, L., and Lee, C. M. (2018). Internal waves in the Arctic: Influence of ice concentration, ice roughness, and surface layer stratification. *Journal of Geophysical Research: Oceans*, 123 (8), 5571–5586. doi:10.1029/2018JC014096

Comiso, J. C., Parkinson, C. L., Gersten, R., and Stock, L. (2008). Accelerated decline in the Arctic sea ice cover. *Geophysical Research Letters*, 35, L01703. doi:10.1029/2007GL031972

D'Asaro, E. A., Eriksen, C. C., Levine, M. D., Paulson, C. A., Niiler, P., and Van Meurs, P. (1995). Upper-ocean inertial currents forced by a strong storm. Part I: Data and comparisons with linear theory. *Journal of Physical Oceanography,* 25 (11), 2909–2936. doi:10.1175/1520-0485(1995)025⟨2909:UOICFB⟩2.0.CO;2

D'Asaro, E. A. (1989). The decay of wind-forced mixed layer inertial oscillations due to the β effect. *Journal of Geophysical Research*, 94 (C2), 2045–2056. doi:10.1029/JC094iC02p02045

D'Asaro, E. A., and Morehead, M. D. (1991). Internal waves and velocity fine structure in the Arctic Ocean. *Journal of Geophysical Research: Oceans*, 96 (C7), 12725–12738. doi:10.1029/91JC01071

Dosser, H. V., Chanona, M., Waterman, S., Shibley, N. C., and Timmermans, M.-L. (2021). Changes in internal wave-driven mixing across the Arctic Ocean: Finescale estimates from an 18-year pan-Arctic record. *Geophysical Research Letters*, 48 (8), e2020GL091747. doi:10.1029/2020GL091747

Dosser, H. V., and Rainville, L. (2016). Dynamics of the changing near-inertial internal wave field in the Arctic Ocean. *Journal of Physical Oceanography*, 46 (2), 395–415. doi:10.1175/JPO-D-15-0056.1

Elipot, S., Lumpkin, R., and Prieto, G. (2010). Modification of inertial oscillations by the mesoscale eddy field. *Journal of Geophysical Research: Oceans*, 115 (C9). doi:10.1029/2009JC005679

Fine, E. C., and Cole, S. T. (2022). Decadal observations of internal wave energy,

shear, and mixing in the western Arctic Ocean. *Journal of Geophysical Research: Oceans*, 127 (5). doi:10.1029/2021JC018056

Gill, A. E. (1984). On the behavior of internal waves in the wakes of storms. *Journal of Physical Oceanography,* 14 (7), 1129–1151. doi:10.1175/1520-0485(1984)014⟨1129:OTBOIW⟩2.0.CO;2

Gimbert, F., Jourdain, N. C., Marsan, D., Weiss, J., and Barnier, B. (2012a). Recent mechanical weakening of the Arctic sea ice cover as revealed from larger inertial oscillations. Journal of *Geophysical Research: Oceans*, 117 (C11). doi:10.1029/2011JC007633

Gimbert, F., Marsan, D., Weiss, J., Jourdain, N. C., and Barnier, B. (2012b). Sea ice inertial oscillations in the Arctic basin. *The Cryosphere*, 6 (5), 1187–1201. doi:10.5194/tc-6-1187-2012

Graham, R. M., Cohen, L., Ritzhaupt, N., Segger, B., Graversen, R. G., Rinke, A., et al. (2019). Evaluation of six atmospheric reanalyses over Arctic sea ice from winter to early summer. *Journal of Climate*, 32(14), 4121–4143. doi:10.1175/JCLI-D-18-0643.1

Guest, P.S., Davidson, K.L., Overland, J.E. and Frederickson, P.A. (1995). Atmosphere-Ocean Interactions in the Marginal Ice Zones of the Nordic Seas. In Arctic Oceanography: Marginal Ice Zones and Continental Shelves (eds W.O. Smith and J.M. Grebmeir). doi:10.1029/CE049p0051

Guthrie, J. D., and Morison, J. H. (2021). Not just sea ice: Other factors important to near-inertial wave generation in the Arctic Ocean. *Geophysical Research Letters*, 48 (3). doi:10.1029/2020GL090508

Guthrie, J. D., Morison, J. H., and Fer, I. (2013). Revisiting internal waves and mixing in the Arctic Ocean. *Journal of Geophysical Research: Oceans*, 118 (8), 3966–3977. 10.1002/jgrc.20294

Halle, C., and Pinkel, R. (2003). Internal wave variability in the Beaufort Sea during the winter of 1993/1994. *Journal of Geophysical Research: Oceans*, 108 (C7). doi:10.1029/2000JC000703

Heil, P., and Hibler, W. D. (2002). Modeling the high-frequency component of Arctic sea ice drift and deformation. *Journal of Physical Oceanography*, 32, 3039–3056. doi:10.1175/1520-0485

Hersbach, H., Bell, B., Berrisford, P., Biavati, G., Horanyi, A., Munoz Sabater, J., Nicolas, J., Peubey, C., Radu, R., Rozum, I., Schepers, D., Simmons, A., Soci, C., Dee, D., and Thepaut, J.-N. (2023). ERA5 hourly data on single levels from

1940 to present [Copernicus Climate Change Service (C3S) Climate Data Store (CDS)]. doi:10.24381/cds.adbb2d47

Hutchings, J. K., Heil, P., and Hibler III, W. D. (2005). Modelling linear kinematic features in sea ice. *Monthly Weather Review*, 133, 3481–3497. doi:10.1175/MWR3045.1

Hutchings, J. K., Heil, P., Steer, A., and Hibler III, W. D. (2012), Subsynoptic scale spatial variability of sea ice deformation in the western Weddell Sea during early summer, *Journal of Geophysical Research*, 117, C01002, doi:10.1029/2011JC006961

Kawaguchi, Y., Itoh, M., Fukamachi, Y., Moriya, E., Onodera, J., Kikuchi, T., and Harada, N. (2019). Year-round observations of sea-ice drift and near inertial internal waves in the Northwind Abyssal Plain, Arctic Ocean. *Polar Science*, 21, 212–223. doi:10.1016/j.polar.2019.01.004

Kunze, E. (1985). Near-inertial wave propagation in geostrophic shear. *Journal of Physical Oceanography*, 15 (5), 544–565. doi:10.1175/1520-0485(1985)015⟨0544:NIWPIG⟩2.0.CO;2

Kwok, R., Cunningham, G. F., and Hibler, W. D., III. (2003). Sub-daily sea ice motion and deformation from RADARSAT observations. *Geophysical Research Letters*, *30*(23), 2218. doi:10.1029/2003GL018723

Kwok, R., and Rothrock, D. (2009). Decline in Arctic sea ice thickness from submarine and ICESat records: 1958–2008. *Geophysical Research Letters*, 36 (15), L15501. doi:10.1029/2009GL039035

Large, W. G., and Yeager, S. G. (2004). Diurnal to decadal global forcing for ocean and sea-ice models: The data sets and flux climatologies (Technical Note NCAR/TN-460+STR). National Center for Atmospheric Research. Boulder, Colorado.

Levine, M. D., Paulson, C. A., and Morison, J. H. (1987). Observations of internal gravity waves under the Arctic pack ice. *Journal of Geophysical Research: Oceans*, 92 (C1), 779–782. doi:10.1029/JC092iC01p00779

Lopez-Acosta, R., Schodlok, M. P., and Wilhelmus, M. M. (2019). Ice floe tracker: An algorithm to automatically retrieve Lagrangian trajectories via feature matching from moderate-resolution visual imagery. Remote Sensing of Environment, 234, 111406. doi:10.1016/j.rse.2019.111406

Manley, T. O., and Hunkins, K. (1985). Mesoscale eddies of the Arctic Ocean. *Journal of Geophysical Research: Oceans*, 90 (C3), 4911–4930.

doi:10.1029/JC090iC03p04911

Manucharyan, G.E., Lopez-Acosta, R. and Wilhelmus, M.M. (2022) Spinning ice floes reveal intensification of mesoscale eddies in the western Arctic Ocean. *Scientific Reports*, 12, 7070. doi:10.1038/s41598-022-10712-z

Martin, T., Steele, M., and Zhang, J. (2014). Seasonality and long-term trend of Arctic Ocean surface stress in a model. *Journal of Geophysical Research: Oceans*, 119 (3), 1723–1738. doi:10.1002/2013JC009425

McPhee, M. G. (1978). A simulation of inertial oscillation in drifting pack ice. *Dynamics of Atmospheres and Oceans*, 2 (2), 107–122. doi:10.1016/0377-0265(78)90005-2

Morison, J. H., Long, C. E., and Levine, M. D. (1985). Internal wave dissipation under sea ice. *Journal of Geophysical Research: Oceans*, 90 (C6), 11959–11966. doi:10.1029/JC090iC06p11959

Ou, H. W., and Gordon, A. L. (1986). Spin-down of baroclinic eddies under sea ice. *Journal of Geophysical Research: Oceans*, 91 (C6), 7623–7630. doi:10.1029/JC091iC06p07623

Peralta-Ferriz, C., and Woodgate, R. A. (2015). Seasonal and interannual variability of pan-arctic surface mixed layer properties from 1979 to 2012 from hydrographic data, and the dominance of stratification for multiyear mixed layer depth shoaling. *Progress in Oceanography*, 134, 19–53. doi:10.1016/j.pocean.2014.12.005

Persson, O., Cox, C., Gallagher, M., Shupe, M., Hutchings, J., Watkins, D., and Perovich, D. (2023). Arctic Cyclone Cloud and Boundary-Layer Features Producing Thermodynamic and Dynamic Impacts on Arctic Sea Ice During MOSAiC, *EGU General Assembly 2023*, Vienna, Austria, 24–28 Apr 2023, EGU23-17554, 10.5194/egusphere-egu23-17554

Pinkel, R. (2005). Near-inertial wave propagation in the western Arctic. *Journal of Physical Oceanography*, 35 (5), 645–665. doi:10.1175/JPO2715.1

Pinkel, R. (2008). Advection, phase distortion, and the frequency spectrum of finescale fields in the sea. *Journal of Physical Oceanography*, 38 (2), 291–313. doi:10.1175/2007JPO3559.1

Pollard, R., and Millard, R. (1970). Comparison between observed and simulated wind generated inertial oscillations. *Deep Sea Research and Oceanographic Abstracts*, 17 (4), 813–821. doi:10.1016/0011-7471(70)90043-4

Rainville, L., and Woodgate, R. A. (2009). Observations of internal wave generation in the seasonally ice-free Arctic. *Geophysical Research Letters*, 36 (23), L23, 604. doi:10.1029/2009GL041291

Rampal, P., Weiss, J., and Marsan, D. (2009). Positive trend in the mean speed and deformation rate of Arctic sea ice, 1979–2007. *Journal of Geophysical Research*, 114, C05013. doi:10.1029/2008JC005066

Raspaud, M., Hoese, D., Lahtinen, P., Holl, G., Finkensieper, S., Proud, S., Meraner, A., Dybbroe, A., Strandgren, J., Yukaribbba, Feltz, J., Joro, S., BENR, Zhang, X., Ghiggi, G., Roberts, W., Youva, de Buyl, P., Rasmussen, L. Ø., Samain, O., et al. (2024). *Pytroll/Satpy* (Version 0.51.0) [Software]. Zenodo. doi:10.5281/zenodo.596324

Rothrock, D., Percival, D., and Wensnahan, M. (2008). The decline in Arctic sea-ice thickness: Separating the spatial, annual, and interannual variability in a quarter century of submarine data. *Journal of Geophysical Research*, 113, C05003. doi:10.1029/2007JC004252

Spreen, G., Kaleschke, L., and Heygster, G. (2008). Sea ice remote sensing using AMSR-E 89 GHz channels. Journal of Geophysical Research: Oceans, 113 (C2). doi:10.1029/2005JC003384

Sumata, H., Kauker, F., Karcher, M., Rabe, B., Timmermans, M.-L., Behrendt, A., Gerdes, R., Schauer, U., Shimada, K., Cho, K.-H., and Kikuchi, T. (2018). Decorrelation scales for Arctic Ocean hydrography – part I: Amerasian Basin. *Ocean Science*, 14, 161–185. doi:10.5194/os-14-161-2018

Thomas, L. N., Skyllingstad, E. D., Rainville, L., Hormann, V., Centurioni, L., Moum, J. N., Asselin, O., and Lee, C. M. (2023). Damping of inertial motions through the radiation of near-inertial waves in a dipole vortex in the Iceland Basin. *Journal of Physical Oceanography*, 53 (7), 1821–1833. doi:10.1175/JPO-D-22-0202.1

Tschudi, M., Meier, W. N., Stewart, J. S., Fowler, C., and Maslanik, J. (2019). Polar Pathfinder daily 25 km EASE-Grid sea ice motion vectors, version 4. doi:10.5067/INAWUWO7QH7B

Watkins, D. M., Persson, P. O. G., Stanton, T., Solomon, A., Hutchings, J. K., Haapala, J., and Svensson, G. (2024). Air-ice-ocean coupling during a strong mid-winter cyclone: Observing coupled dynamic interactions across scales. *Journal of Geophysical Research: Atmospheres*, 129 (17), e2024JD041057. doi:10.1029/2024JD041057

Young, W. R., and Jelloul, M. B. (1997). Propagation of near-inertial oscillations

through a geostrophic flow. *Journal of Marine Research*, 55 (4).

Zhao, M., Timmermans, M.-L., Cole, S., Krishfield, R., Proshutinsky, A., and Toole, J. (2014). Characterizing the eddy field in the arctic ocean halocline. Journal of Geophysical Research: Oceans, 119 (12), 8800–8817. doi:10.1002/2014JC010488

10 Figures

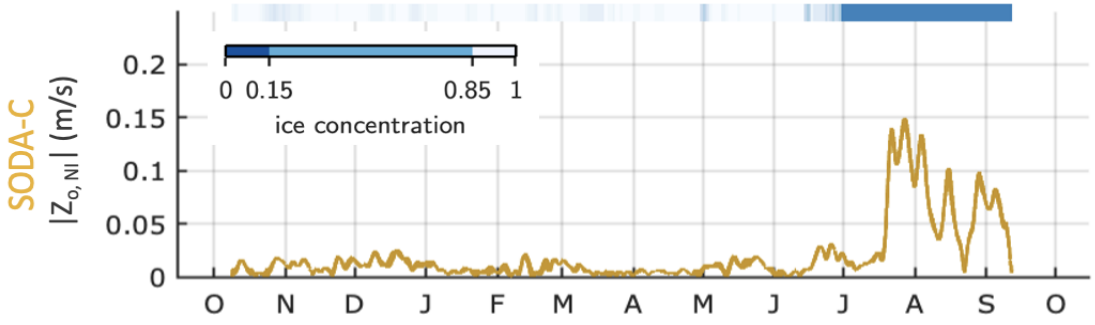

Figure 4.1 Mixed layer averaged near-inertial velocity at the SODA–C mooring throughout its 2018-2019 deployment. The sea ice fraction from ERA5 is shown at the top, with values below 0.85 approximating marginal ice conditions in which sea ice internal stresses are minimized.

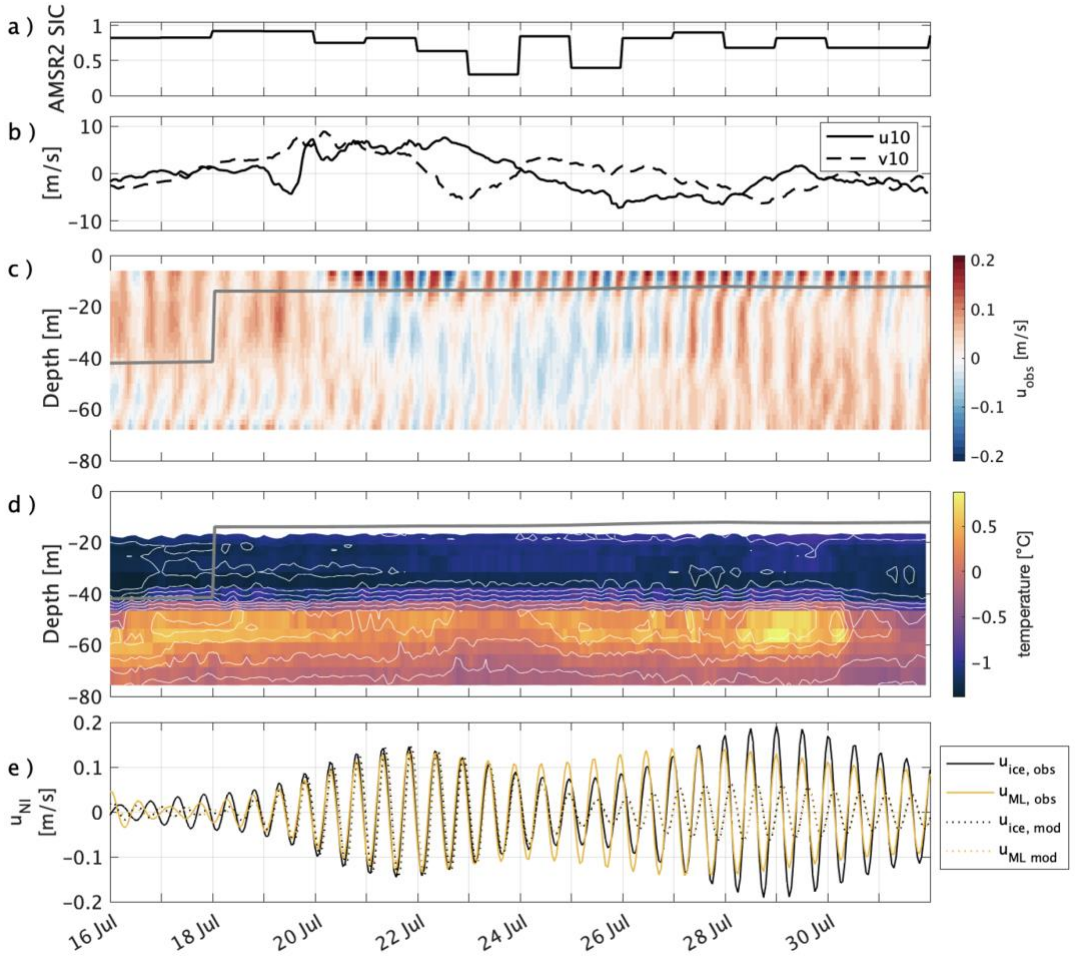

Figure 4.2 Conditions at the SODA–C mooring site during the study period in July 2019. (a) AMSR2 ice fraction at the mooring site. (b) The eastward (u10) and northward (v10) components of wind at 10 m from ERA5 at the mooring site. (c) ADCP-measured eastward velocity at the mooring, with the mixed layer depth shown by the thick gray line. (d) Temperature observed by the mooring (colors, thin contours) with the mixed layer depth shown by the thick gray line. (e) Sea ice (black lines) and mixed layer average (yellow lines) near-inertial eastward velocity observed by ADCPs (solid lines) and predicted by the slab model (dotted lines).

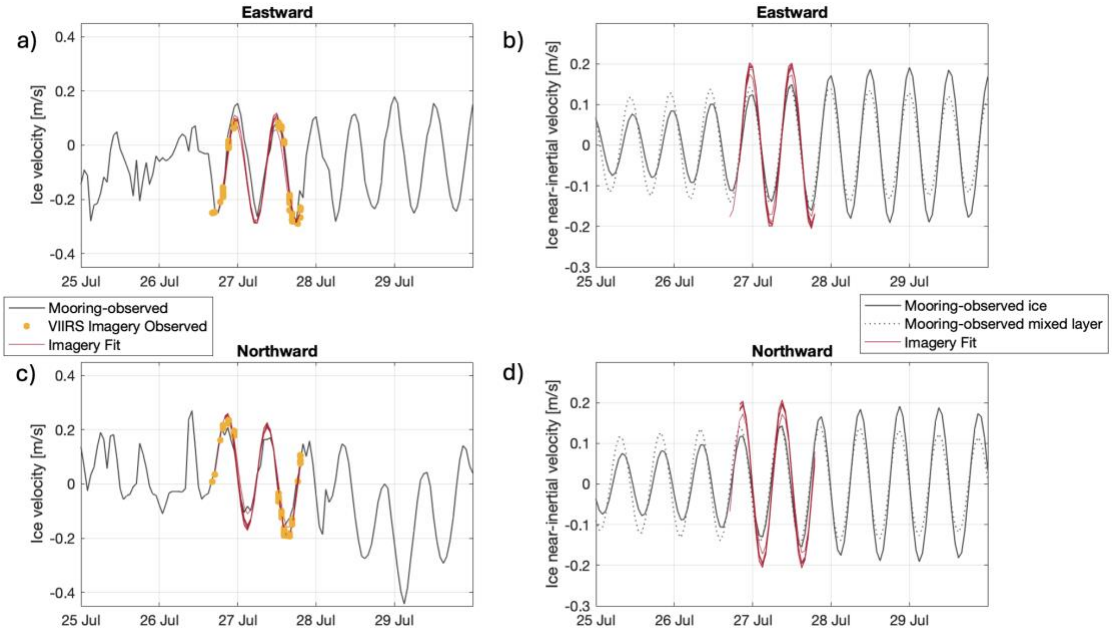

Figure 4.3 Comparison of broadband (a, c) and near-inertial (b,d) ice velocity observed by mooring ADCP (solid black lines) and derived from ice motion tracking on VIIRS images (yellow points) for (a) eastward and (c) northward component of velocity. VIIRS data are shown for the eight tracked points within 20 km of the mooring. The red lines in (a, c) show the least squares fit velocity for each tracked point, and the red lines in (b, d) show the inertial part of the least squares fit velocity. The dotted black lines in (b, d) show the mixed layer averaged near-inertial velocity.

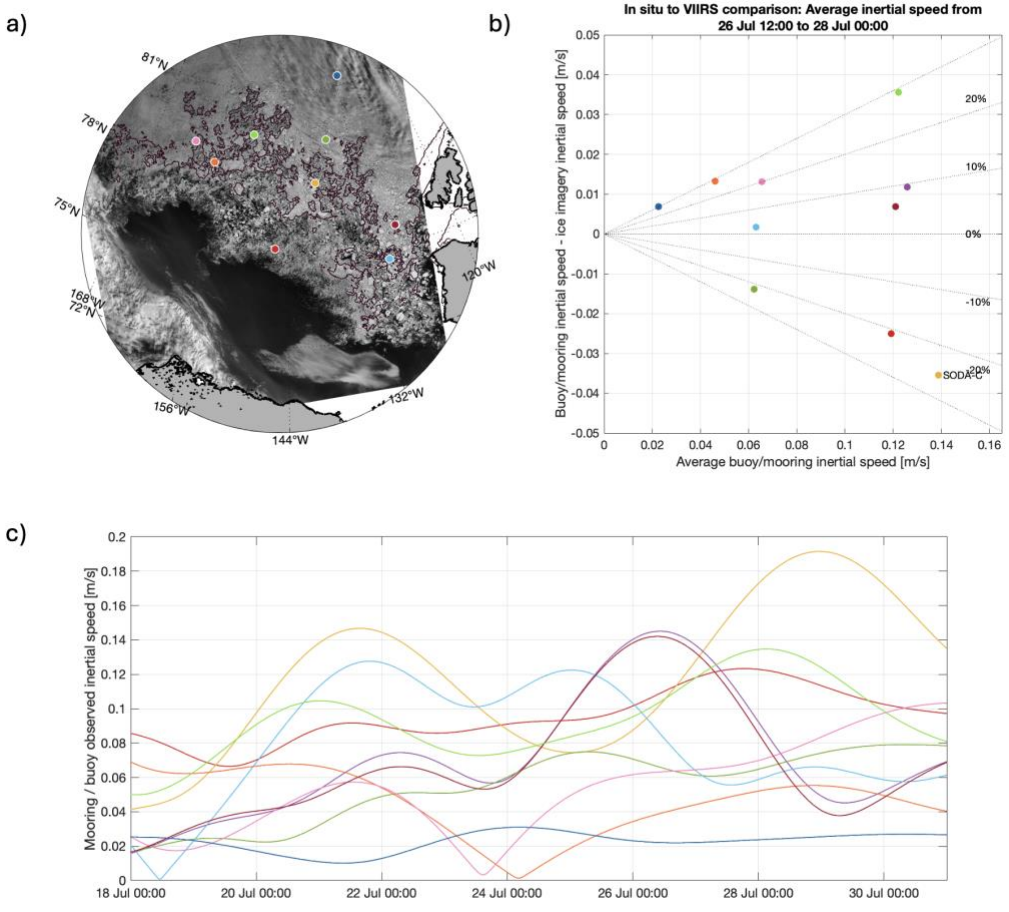

Figure 4.4 (a) Map of locations of SODA moorings and IABP buoys with co-located inertial velocities from VIIRS satellite image tracking. The SODA–C mooring is shown by the yellow dot. The underlying satellite image shows data from the VIIRS image band 1 taken on 27 July 2019 at 18:24 UTC. The purple contour shows where the AMSR2 ice fraction exceeded 0.8. Gray areas show the coast. (b) The difference in time-averaged (26 July 12:00 to 28 July) near-inertial speed between a mooring/buoy and VIIRS-derived ice velocity in a 36 km × 36 km region surrounding the in situ observation. (c) Near-inertial speed observed by the moorings or buoys. Note that the buoys represented by dark red and purple were located less than 2 km apart, so the purple buoy's location is obscured in (a).

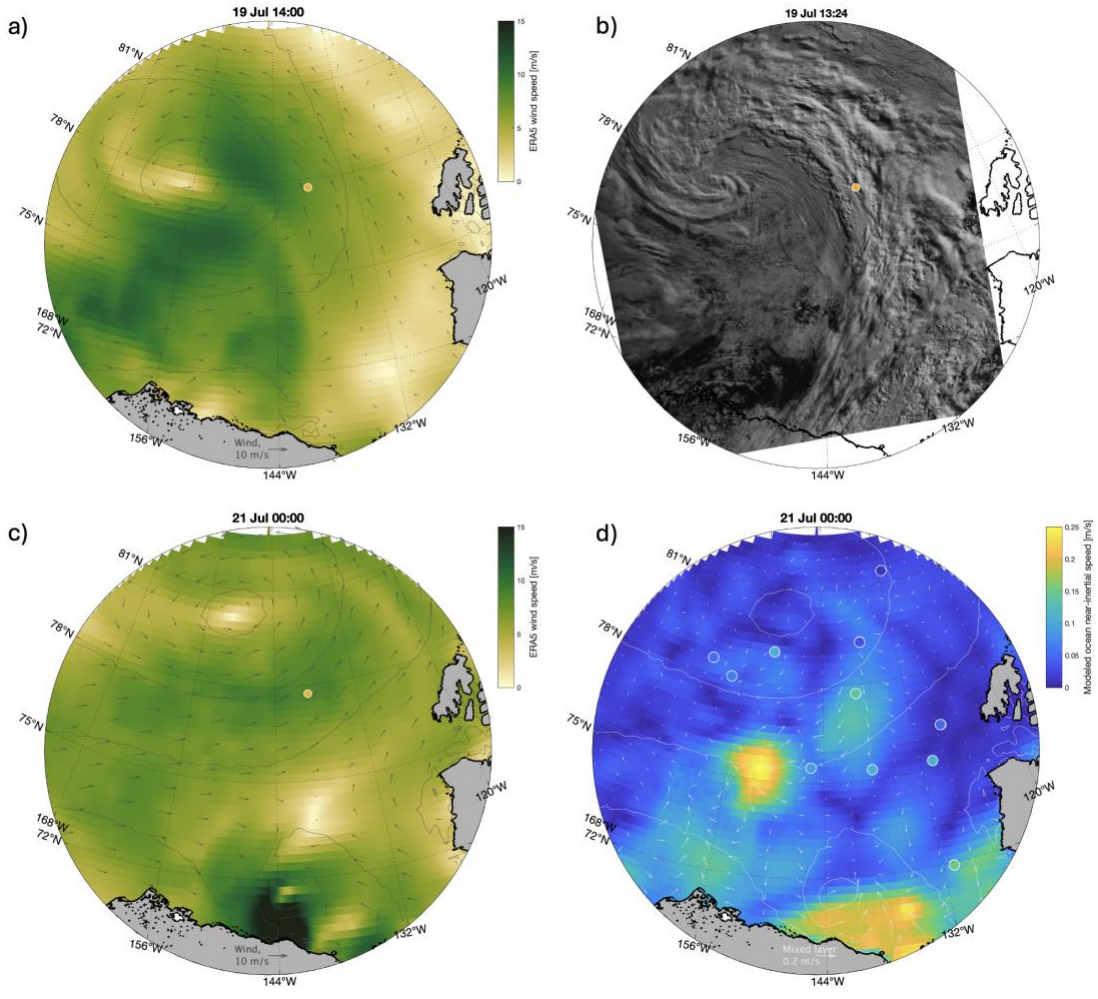

Figure 4.5 (a, c) Regional wind (colors, vectors) and ERA5 surface pressure (gray contours) on 19 July 2019 14:00 UTC and 21 July 2019 00:00 UTC. The SODA–C mooring location is shown by the yellow dot. Land is shown in gray. (b) Satellite image from VIIRS image band 1 taken on 19 July 2019 at 13:24 UTC. (d) Slab modeled mixed layer near inertial velocity (colors, vectors) and ERA5 surface pressure (white contours) on 21 July 2019 00:00 UTC. Colored dots show near-inertial speed observed by in situ observations (SODA mooring ice velocities and IABP buoy trajectories with co-located VIIRS ice velocities).

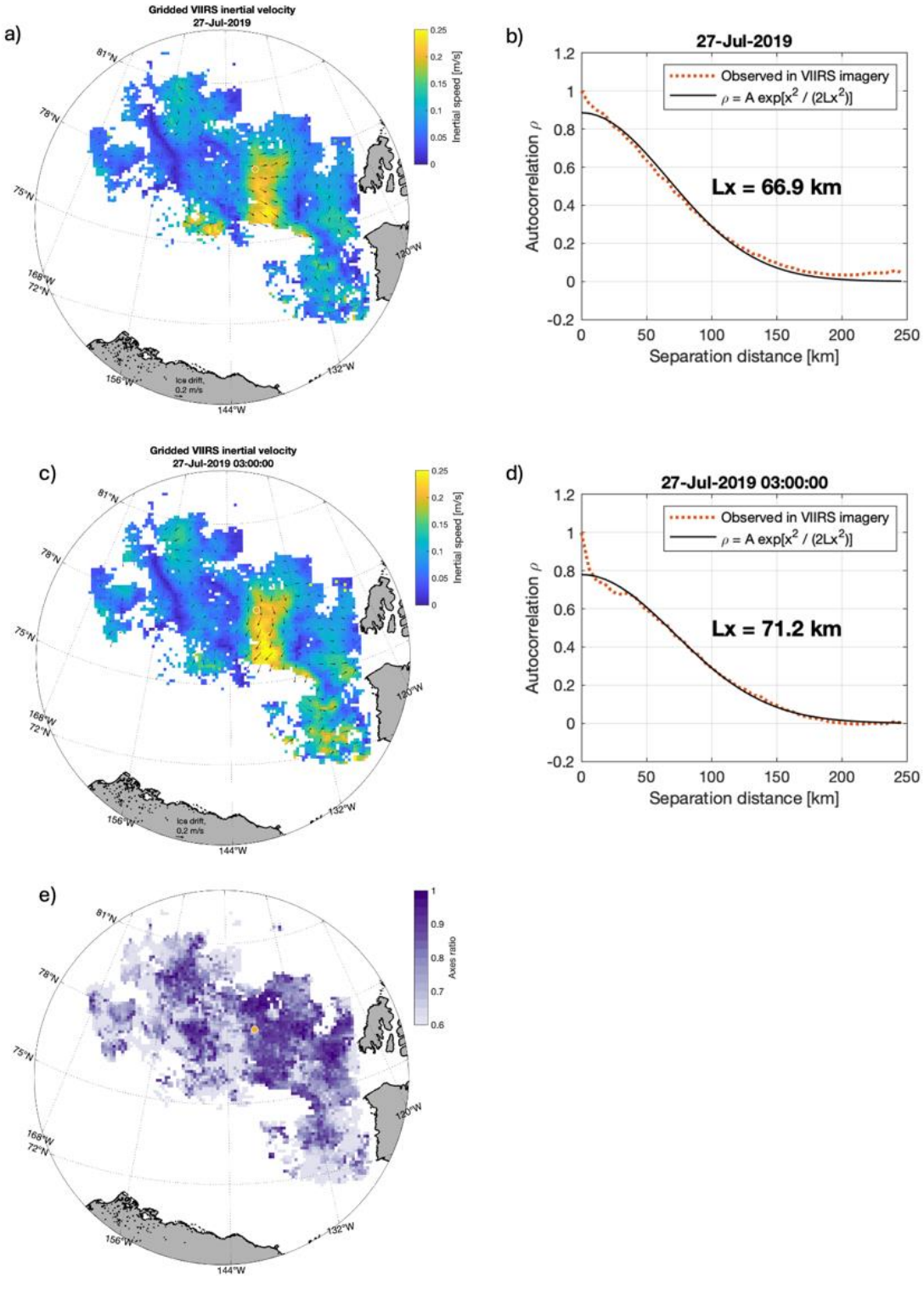
a)
Gridded VIIRS inertial velocity
27-Jul-2019
Inertial speed [m/s]
81°N
78°N
75°N
168°W
72°N
120°W
132°W
156°W
144°W
Ice drift,
0.2 m/s
b)
27-Jul-2019
Observed in VIIRS imagery
ρ = A exp[x² / (2Lx²)]
Lx = 66.9 km
Autocorrelation ρ
Separation distance [km]
c)
Gridded VIIRS inertial velocity
27-Jul-2019 03:00:00
d)
27-Jul-2019 03:00:00
Lx = 71.2 km
e)
Axes ratio

Figure 4.6 (a,c) Near-inertial ice velocity (colors, vectors) from trajectories of points tracked in VIIRS images, gridded to a 12 km horizontal resolution grid, on 27 July 2019 at (a) 00:00 UTC and (c) 03:00 UTC. The SODA–C mooring location is shown by the yellow dot. (b,d) The dotted red line shows autocorrelation as a function of spatial lag distance, calculated from paired inertial oscillation speed observations shown in panels a and c. The solid black line shows a Gaussian fit to the observations, with the fitting parameter L_x defining the decorrelation scale. (e) Ratio of minor to major axes lengths for ellipses fit to the inertial velocity timeseries at each grid point.

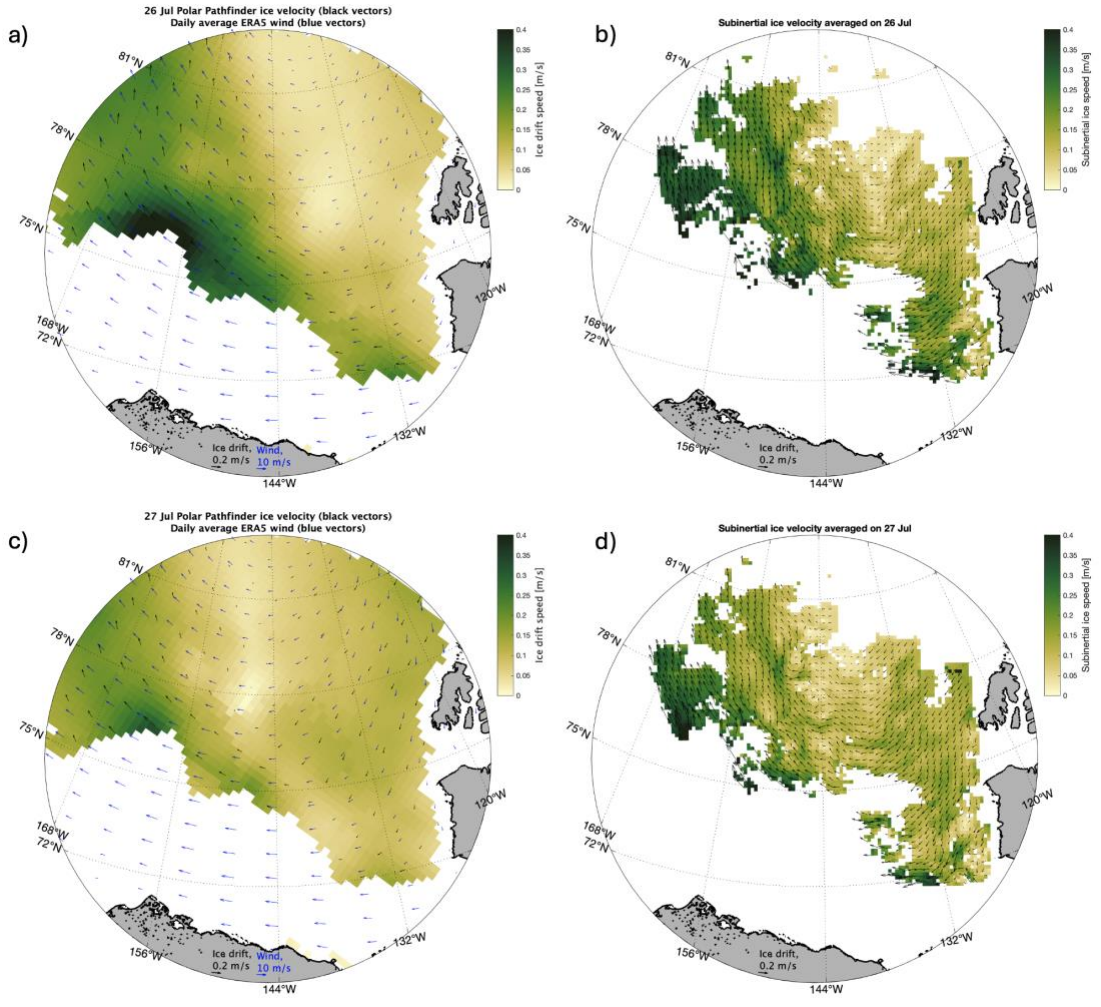

Figure 4.7 Panels (a) and (c) show Polar Pathfinder ice velocity (color, black vectors) and daily averaged ERA5 wind (blue vectors) on 26 and 27 July 2019. Panels (b) and (d) show daily averaged subinertial ice velocities on 26 and 27 July 2019, derived from points tracked in VIIRS imagery and gridded to 12 km horizontal resolution.

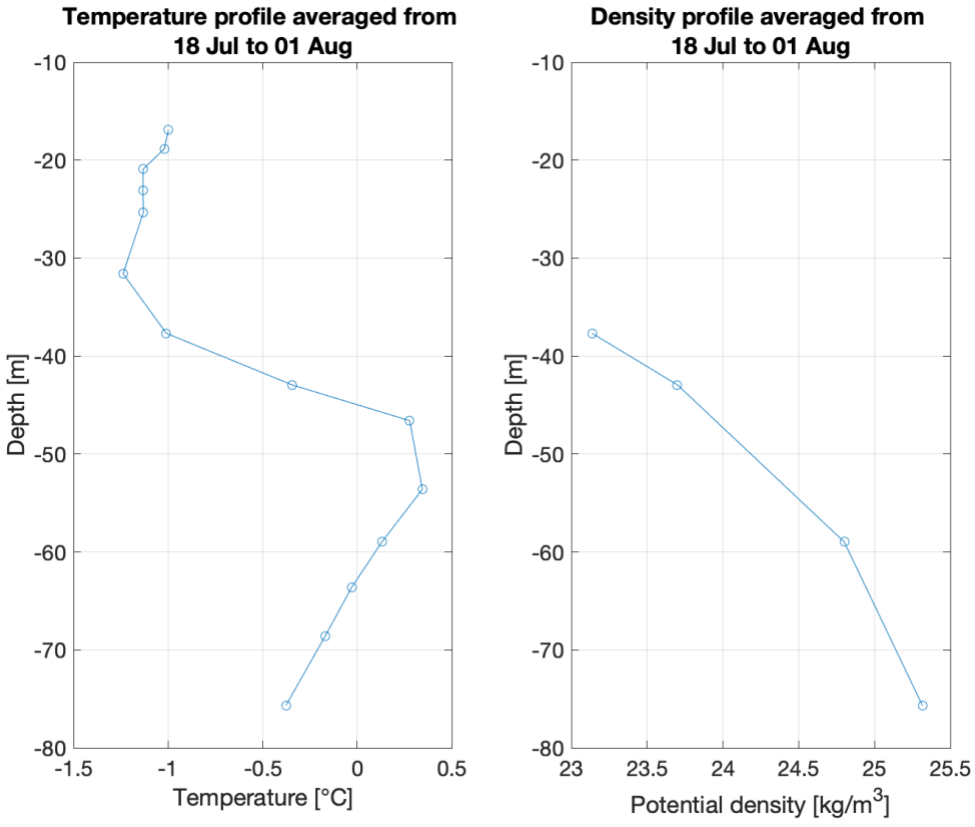

Figure 4.8 Average temperature vertical profile (left) and density vertical profile (right) measured at the SODA–C mooring from 18 July to 1 August 2019, with the instrument depths shown by open circles.

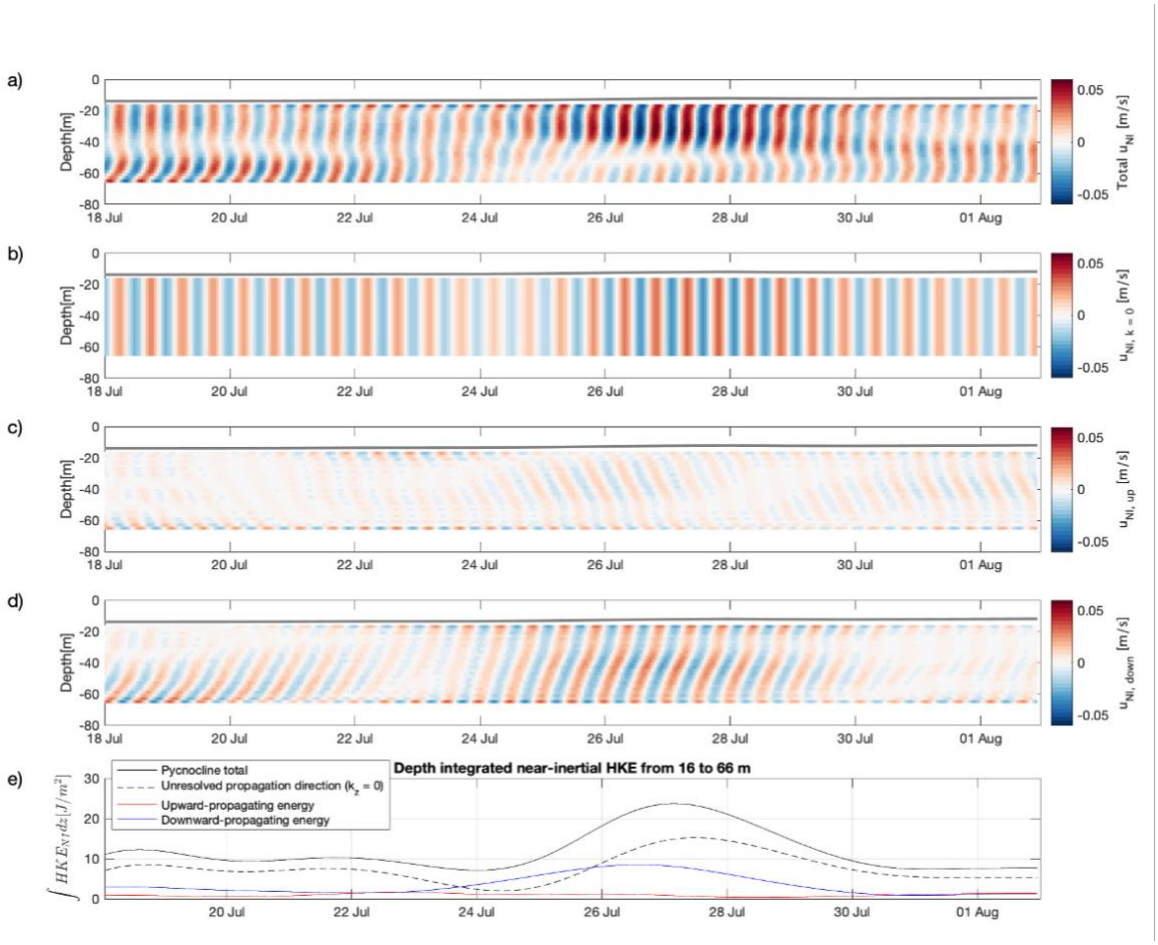

Figure 4.9 (a) Near-inertial eastward velocity observed in July 2019 by SODA–C mooring ADCPs below the mixed layer. This velocity was separated into components with (b) low wavenumber and unresolved vertical direction of energy propagation, (c) upward energy propagation, and (d) downward energy propagation. In panels a-d, the gray line is the mixed layer depth. Panel (e) shows the depth-integrated near-inertial horizontal kinetic energy of each of these components.

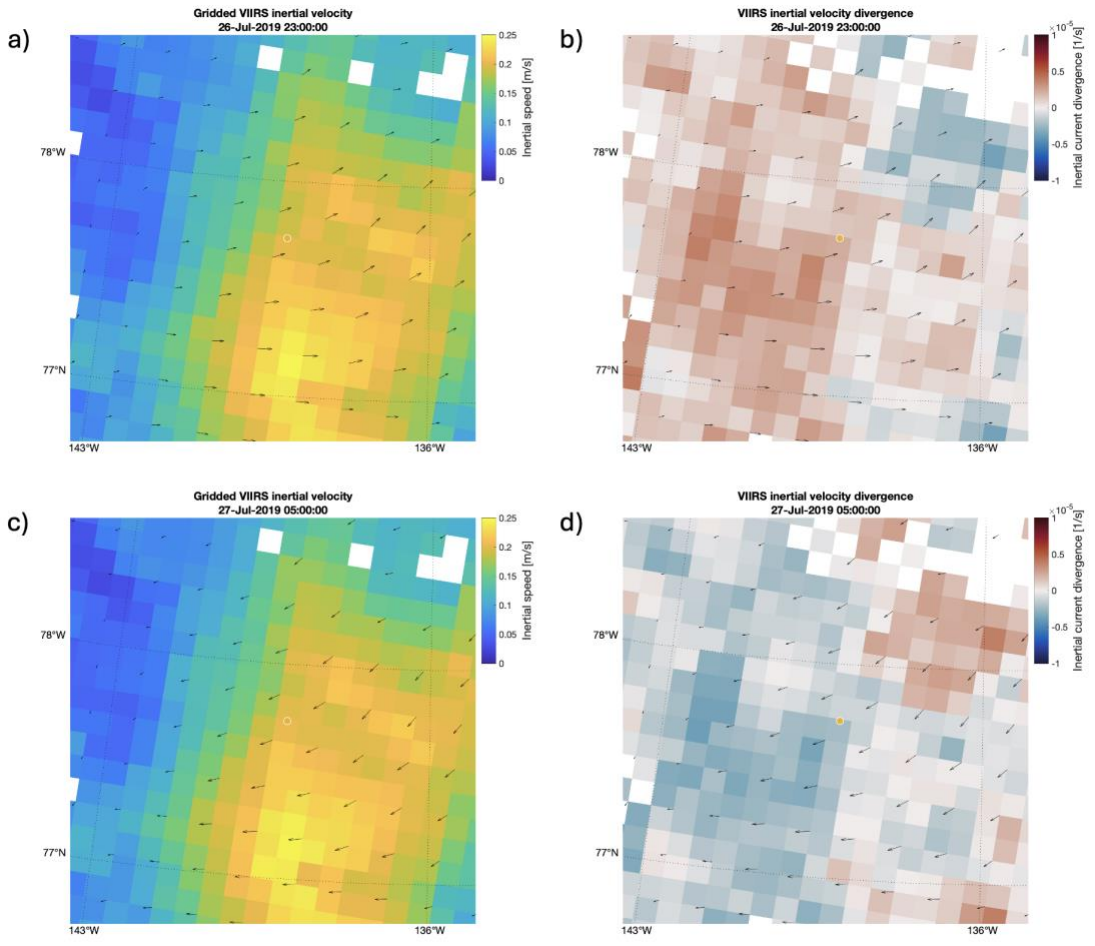

Figure 4.10 (a,c) Near-inertial ice velocity from trajectories of points tracked in VIIRS images, gridded to a 12 km horizontal resolution grid, in an approximately 200 km × 200 km region around the SODA–C mooring (yellow dot) for (a) 26 July 23:00 2019 and (b) 27 July 05:00 2019. (b,d) Near-inertial velocity (vectors) and divergence (colors) for the same region and times. Every other velocity vector is shown for clarity.

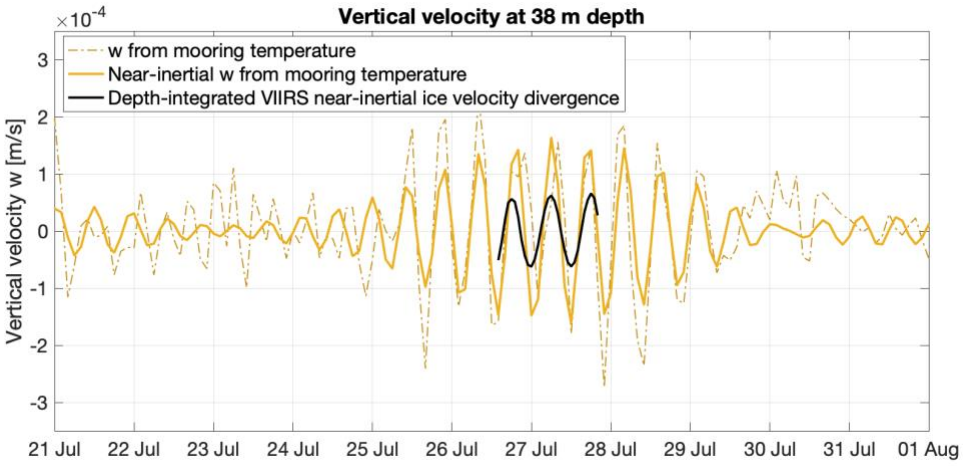

Figure 4.11 Vertical velocity at the SODA–C mooring at 38 m depth estimated using mooring-observed temperature time series (yellow lines) and depth-integrated divergence of near-inertial velocity derived from VIIRS satellite images (black line). The mooring observed broad banded vertical velocity is shown by the dot-dashed yellow line, while the near-inertial vertical velocity is shown by the solid yellow line.

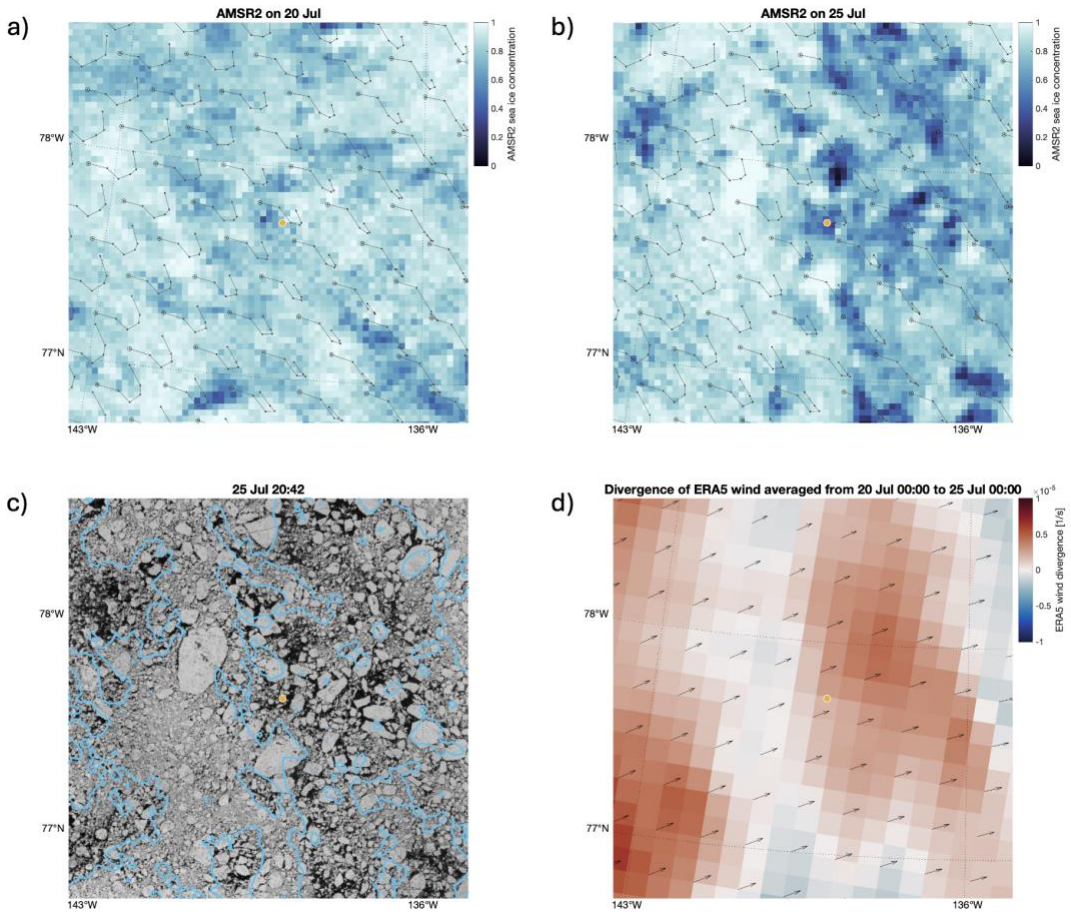

Figure 4.12 (a,b) AMSR2 sea ice fraction in an approximately 200 km × 200 km region around the SODA–C mooring (yellow dot) for (a) 20 July 2019 and (b) 25 July 2019. The black lines are identical between panels (a) and (b) and show integrated Polar Pathfinder ice motion vectors from 20-25 July, simulating ice displacement over this time. The black open circles represent the starting positions, with the closed circles showing the updated positions on each day. (c) Example VIIRS satellite image for the same region with the AMSR2 0.85 ice fraction contour shown in blue. (d) Divergence calculated from 20-25 July averaged ERA5 wind.

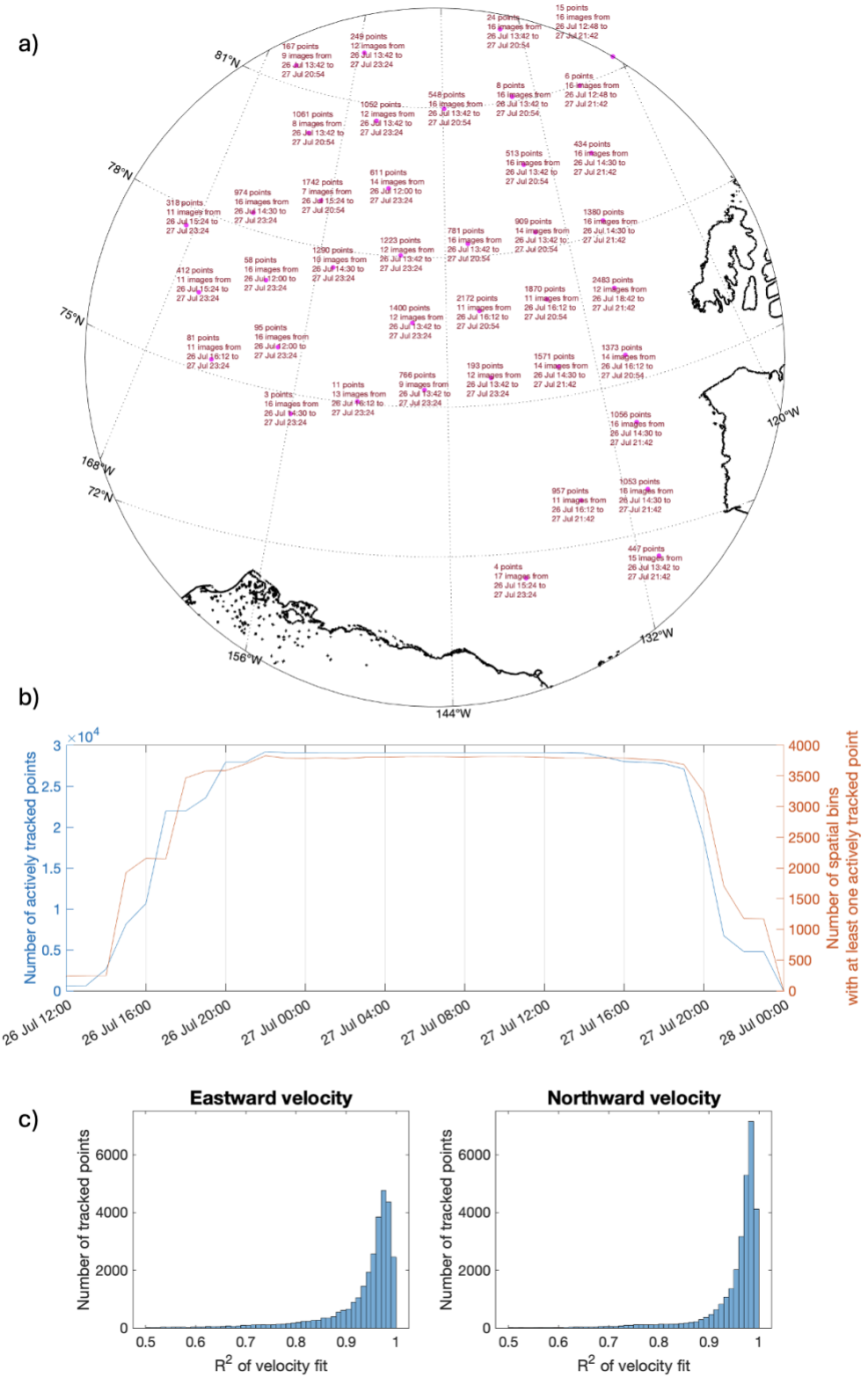
a)
81°N
78°N
75°N
72°N
168°W
156°W
144°W
132°W
120°W
b)
Number of actively tracked points
Number of spatial bins with at least one actively tracked point
×10^4
26 Jul 12:00
26 Jul 16:00
26 Jul 20:00
27 Jul 00:00
27 Jul 04:00
27 Jul 08:00
27 Jul 12:00
27 Jul 16:00
27 Jul 20:00
28 Jul 00:00
c)
Eastward velocity
Northward velocity
Number of tracked points
R^2 of velocity fit

Supplementary Figure 4.1 (a) Pink points show the centers of each 300 km x 300 km geographic subregion into which basin-wide satellite images were divided prior to floe tracking. Subregions had 50% overlap, meaning the boundaries of an individual subregion are denoted by the eight points surrounding a center point. Each subregion is labeled with text stating the number of points tracked in imagery, the number of images in which points were tracked, and the time range over which those points were tracked. (b) The number of actively tracked points at a given time in the entire study region, and the number of 12 km × 12 km spatial bins with at least one actively tracked point at that time. (c) Histograms of the R^2 of the fit to Equations 4.1 and 4.2 for each tracked point's observed velocity.

Chapter 5 Conclusion

1 Chapter summaries

1.1 Chapter 2

Sea ice freeze up in autumn is patchy on spatial scales that suggest an oceanographic influence. Chapter 2 studied how freeze up timing was impacted by melting sea ice that lingered in the southern Beaufort Sea in September 2018 and created a cold, fresh, and shallow mixed layer. Ship-based, Seaglider, and satellite observations were used to study the mixed layer's evolution as this meltwater advected roughly 100 km during the three weeks preceding freeze up. By cooling and shoaling the mixed layer, the meltwater hastened freeze up. Ice advanced in meltwater-affected areas several days earlier than in surrounding areas where meltwater was absent.

The mixed layer heat budget for the autumn cooling period showed that, outside of the meltwater, regional-scale heat loss to the atmosphere was the dominant means of mixed layer cooling. Within the area affected by meltwater, horizontal advection was nearly as important as heat loss to the atmosphere for seasonally integrated mixed layer heat loss, while heat gained by the mixed layer from the pycnocline was less important.

These results regarding freeze up timing highlight the coupled nature of spatial variability in the sea ice and ocean mixed layer. Mixed layer lateral variability in temperature and stratification drove lateral variability in the development of newly formed ice, imposing smaller scales on ice formation date than would be predicted from integrated heat loss to the atmosphere.

1.2 Chapter 3

Sea ice selectively damped high frequency mixed layer velocities across the SODA mooring array, with year-round observations showing an order of magnitude reduction in near-inertial horizontal kinetic energy but no significant differences in Ekman transport at high ice concentration (Brenner et al., 2023). Chapter 3 studied the ice and ocean responses to a February 2019 storm at two mooring sites. During this event, frequency-selective damping was active at one site only, presenting an opportunity to investigate its underlying causes.

Sea ice lead opening at the southern mooring site relieved internal stresses in the ice pack and preconditioned undamped inertial oscillation development in the ice and mixed layer. This conclusion was reached after considering many other possible causes for the difference in inertial motion damping between moorings. The storm's potential to produce inertial oscillations was similar at both sites, as simulated by a coupled ice-ocean slab model that was used to control for regional differences in the strength and resonance of the wind forcing, mixed layer depth, and ice-ocean drag associated with observed under-ice roughness. Ice fraction from satellite passive microwave sensors exceeded 0.85 at both sites and was somewhat higher at the weakly-damped southern site. Daily ice drift speeds were also comparable between sites.

This Chapter shows how the ice and ocean near-inertial responses to a winter storm could only be understood in the context of the ice pack's lateral structure. The results suggest that floe size and the lateral scales of ice fracturing, determined in part by distant ice-coast interactions, may modulate ocean inertial oscillations.

1.3 Chapter 4

Predicting near-inertial internal wave generation in the presence of sea ice remains a vexing problem as some storms produce near-inertial internal waves beneath sea ice while others do not (e.g., Halle and Pinkel, 2003; Martini et al., 2014). Chapter 4 considered the hypothesis that sea ice can generate near-inertial internal waves by promoting spatially divergent inertial oscillations. To investigate this hypothesis, tracked points in high temporal resolution satellite imagery were used to create a basin-wide map of sea ice inertial oscillations following a July 2019 storm.

The coherence scale of inertial oscillation speed was ~65 km, smaller than predicted from the wind field. These scales were not resolved by the existing Lagrangian buoy network. Neither β-refraction nor ζ-refraction, processes that are important for dephasing inertial oscillations in other regions, appeared to be primary factors in the apparent reduction of inertial oscillation scales observed in our data. Instead, we hypothesize that spatial gradients in sea ice characteristics, including ice concentration, are the most likely drivers of the reduction in inertial oscillation scales. While theoretical inertial pumping calculated from the observed inertial oscillation structure underestimated the observed internal wave amplitudes, this might approach might be useful for finding internal wave generation hotspots.

Decades of mid-latitude investigation have demonstrated that the reduction of the lateral scales of inertial oscillations is essential to near-inertial internal wave generation. Chapter 4 demonstrated that sea ice likely plays a role in setting the scales at which inertial oscillations are generated or the rate at which they decay. Thus, floe-

floe interactions and gradients in internal ice stresses on scales of 10-100 km may contribute to the strength of the near-inertial internal wave field in the ocean interior, again demonstrating the importance of the lateral structure of the ice pack to ocean dynamics.

2 Open questions and implications for future research

2.1 Freshwater layers and freeze up

Autumn observations show that some, but not all, ice edges have strong (~1 g kg^{-1}) salinity fronts. While Brenner et al. (2020) observed a similarly strong meltwater front during the ONR Marginal Ice Zone program (their Figure 2) to that considered in Chapter 2, Figure 5.1 shows contrasting surface conditions observed in two marginal ice zones sampled on the same Seaglider transect in September-October 2018. The mixed layer on southern end of the transect, discussed extensively in Chapter 2, was cold, fresh, and shallow, while the mixed layer on the northern end of the transect was comparably cold, but saltier and deeper. What accounts for this difference in stratification? One hypothesis is that the northern ice edge retreated dynamically with minimal ice melt, exposing the underlying cold ocean without stratifying it. The contrasting stratification arrangements seen in Figure 5.1 suggest that sea surface temperature and proximity to the ice edge are insufficient for predicting the mixed layer shoaling that played a role in freeze up timing in Chapter 2. It may instead be necessary to consider the local history of ice melt and advection.

Chapter 2 was unable to monitor the fate of heat released from the subsurface stratification after freeze up, so cannot determine its impact on seasonally integrated ice

growth. Observing the evolution of the heat and stratification associated with the meltwater layer on seasonal timescales is challenging (but see Jackson et al., 2012). In the Arctic, the Lagrangian observations needed to observe the evolution of a mesoscale ocean feature like the Chapter 2 meltwater layer are usually collected from ice-based buoys. Differences in ice and mixed layer velocities mean these observations do not track the same region of ocean. Alternate observational approaches, which advect with the mixed layer and can be collected under ice, might be required.

As a process study, Chapter 2 did not quantify the prevalence of strong and shallow freshwater layers with the potential to modify freeze up timing. A forthcoming modeling study (van Straaten et al., 2024) found that low salinity anomalies from ice melt and river runoff are ubiquitous in the Arctic, surviving for weeks to months and traveling long distances. Sea ice formation was enhanced in these low salinity features. These model results bolster our finding that understanding the thickness and advection of such freshwater features should contribute to improved sea ice forecasting at seasonal timescales.

2.2 Inertial oscillations and sea ice leads

Chapter 3 reached its conclusion that inertial oscillations were less damped in areas with sea ice leads by contrasting the inertial response at two mooring sites and considering and ultimately rejecting other variables that might differentiate the sites. Those tested and rejected variables included the strength and resonance of the wind, the depth of the mixed layer, the nearby passive microwave sea ice concentration, and ice mobility as measured by daily ice drift speeds. We were unable to rule out the existence

of other salient differences between the mooring sites that might have contributed to inertial oscillation damping. To further test our conclusion, the number of storm events and study sites considered should be increased.

The Ice Tethered Profiler (ITP) dataset is well-suited to extending this analysis. ITPs are Lagrangian, ice-mounted instrument clusters that profile the upper ocean and directly observe mixed layer depth (Toole et al., 2016). In this proposed analysis, inertial oscillation events of interest observed by the ITPs should be identified using the following criteria. First, sea ice fraction in the ITP's vicinity should exceed a minimum, perhaps 0.8, to identify times when the ice was compact and damping might be expected. Next, following the approach described in Chapter 3, a slab model with no ice damping should be run using each ITP's time-varying observed mixed layer depth and the reanalysis wind at the ITP's time-varying location. Slab modeled inertial speeds should exceed a minimum, perhaps 0.05 m s^{-1}, to ensure focus is placed on times when the wind had at least modest potential to generate inertial oscillations. Once events are identified according to the ice concentration and modeled inertial speed criteria, the amount of damping during an individual event could be calculated from the difference between the ITP-observed inertial oscillation speed (calculated from the buoy's displacement) and the modeled inertial oscillation speed. Damping statistics from many events could then be compared to the lead fraction calculated during those events in the vicinity of ITPs.

Figure 5.2 illustrates these calculations along the trajectory of ITP-33, which was deployed in the Beaufort Sea from 2009-2010. As this example illustrates, these

wintertime events of interest may only occur a few times a year. Despite the limited number of events, these ITP results generally align with the results of Chapter 3. In early January 2010, a large increase in lead fraction around the ITP accompanied elevated observed and slab modeled near-inertial speeds (though the observations were still damped relative to the model). The modeled near-inertial accelerations in March 2010 and May 2010 did not develop in the observations, indicating strong damping by ice at those times, and lead fraction remained small around the ITP during those events.

2.3 Evolution of inertial oscillation coherence scales

The results presented in Chapter 4 provide ample guidance for the design of a future experiment to better understand processes influencing the evolution of inertial oscillation coherence scales. Tracking the spatial scales over which inertial oscillations were coherent shows that Lagrangian buoys placed tens of kilometers apart would be adequate to resolve spatial variability of inertial oscillations. In our study period and region, the average distance from an IABP buoy to its nearest neighbor was more than 150 km (Figure 4.4a), insufficient to resolve the observed inertial oscillation coherence scales. While the visual satellite imagery provided a very dense network of ice velocity observations, it would best serve to provide context to observations from an adequately dense network of GPS-tracked Lagrangian drifters. Such a drifter network would eliminate problems with clouds and shortcomings of the slab model but would come with the significant challenge of anticipating where and when Lagrangian buoys should be deployed to observe a storm and its aftermath.

Alternatively, this study shows that high temporal resolution ice velocity

observations derived from SAR or passive microwave satellite imagery need not have particularly high spatial resolution to study inertial oscillations. A key advantage of sea ice satellite imagery is that it does not require additional instruments to be deployed. The satellites used in Chapter 4 carry Advanced Technology Microwave Sounder (ATMS) instruments in addition to the VIIRS instruments used here. Passive microwave ice motion algorithms (NSIDC Technical Report) applied to these data could perhaps be used to produce comparably high temporal resolution maps of ice velocity as were produced in Chapter 4 using visual imagery, without interference from clouds.

Observations of the temporal evolution of inertial oscillation spatial structure, from buoys or imagery, would eliminate the uncertainties associated with Chapter 4's use of a slab model. This study's uncertainties could further be reduced with a comprehensive survey of background mixed layer oceanographic conditions. Impacts of spatially varying mixed layer depth and inertial oscillation refraction by subinertial flow could be largely accounted for with one background survey of the upper ocean temperature, salinity, and velocity field, which should evolve relatively slowly compared to the generation and decay timescales of inertial oscillations.

Having constrained uncertainties about the generation scales of inertial oscillations, the temporal evolution of those scales, and the potential role played by mixed layer structure on that evolution, one could investigate Chapter 4's hypothesis that spatial variability of internal ice stresses can either impose small horizontal scales on sea ice oscillations at their time of generation or reduce the scales of sea ice

oscillations over time. An experiment should then take place in a region of spatially varying internal stresses. An area with an ice concentration gradient, for example moving from the ice edge into the ice pack, would be a good candidate for such a location. Such a study should also employ ice-based or moored ADCPs to assess internal wave generation in conjunction with inertial oscillation scales.

3 Figures

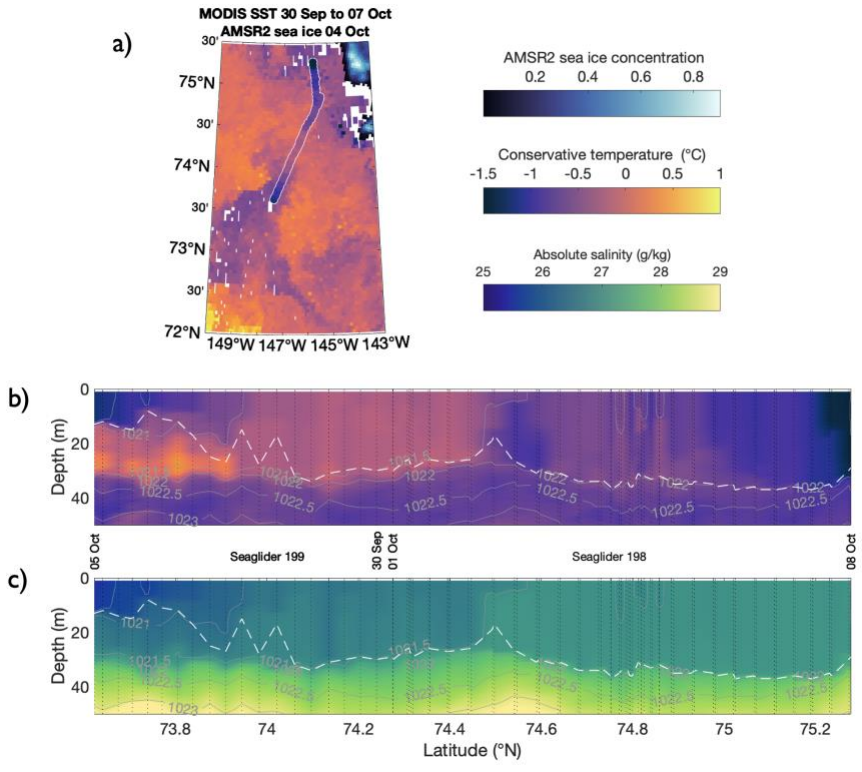

Figure 5.1 Ocean temperature and salinity observed in autumn 2018. Panel (a) shows conservative temperature from Seagliders averaged in the upper 5 m (scatter points) and MODIS-Terra SST (background color). The AMSR2 ice concentration is shown where it exceeded zero. The time periods for the satellite products are specified in the map title. Panels (b-c) show conservative temperature and absolute salinity in latitude-depth sections measured by two Seagliders from 30 September to 8 October. Profile locations are shown as white-outlined dots in panel (a). Sampling began partway through the transect with one Seaglider sampling outward in each direction, indicated by the dates. The gray lines on the section plots mark potential density contours at 0.5 kg m^{-3} intervals and the dashed white lines mark mixed layer depth defined as a density difference of 0.25 kg m^{-3} relative to the surface. Sections show only the upper 50 m of the 1000-m profiles, with vertical lines indicating individual profiles.

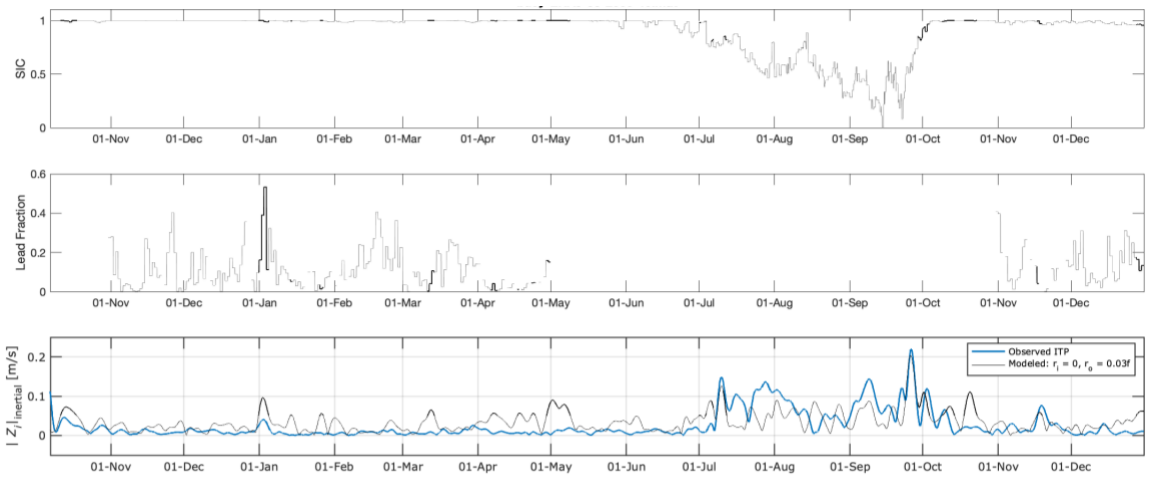

Figure 5.2 Inertial oscillation damping along the trajectory of ITP-33, deployed in the Beaufort Sea from 2009-2010. The top panel shows the AMSR2 sea ice fraction in the grid cell nearest the ITP's position. The center panel shows the lead fraction calculated in a 100 km × 100 km box around the ITP's position. The lead fraction was calculated as (number of pixels classified as lead) / (number of pixels classified as lead + number of pixels classified as ice) in the data of Reiser et al. (2020) and Willmes and Heinemann (2016) which is available at https://meteo.uni-trier.de/v2/arcleads.php. Lead fraction is only plotted at times when lead data are available (November-May) and when the region around the ITP was not excessively cloudy. The bottom panel shows the ITP's observed near-inertial speed (blue line) as well as near-inertial speed produced by a slab model with no ice damping (black line). Events of interest, defined as times when the AMSR2 ice fraction was at least 0.8 and the slab model predicted near-inertial speeds of at least 0.05 m s^{-1}, are highlighted with bold lines.

4 References

Brenner, S., Thomson, J., Rainville, L., Crews, L., and Lee, C. M. (2023). Wind-driven motions of the ocean surface mixed layer in the western Arctic. *Journal of Physical Oceanography*, 53(7), 1787–1804. doi:10.1175/JPO-D-22-0112.1

Brenner, S., Rainville, L., Thomson, J., and Lee, C. (2020). The evolution of a shallow front in the Arctic marginal ice zone. *Elementa: Science of the Anthropocene*, 8–17. doi:10.1525/elementa.413

Halle, C., and R. Pinkel (2003). Internal wave variability in the Beaufort Sea during the winter of 1993/1994, *Journal of Geophysical Research: Oceans*, 108(C7), doi:10.1029/2000JC000703

Jackson, J. M., Williams, W. J., and Carmack, E. C. (2012). Winter sea-ice melt in the Canada Basin, Arctic Ocean. *Geophysical Research Letters*, 39, L03603. doi:10.1029/2011GL050219

Martini, K. I., H. L. Simmons, C. A. Stoudt, and J. K. Hutchings (2014). Near-inertial internal waves and sea ice in the Beaufort Sea, *Journal of Physical Oceanography*, 44(8), 2212–2234, doi:10.1175/JPO-D-13-0160.1

NSIDC National Snow and Ice Data Center. (n.d.). Measuring sea ice motion (technical report). National Snow and Ice Data Center (NSIDC). Boulder, CO. https://nsidc.org/sites/default/files/measureseaicemotion-0116-0748_0.pdf

Reiser, F., Willmes, S., and Heinemann, G. (2020). A new algorithm for daily sea ice lead identification in the Arctic and Antarctic winter from thermal-infrared satellite imagery. *Remote Sensing, 12*(12), 1957. doi:10.3390/rs12121957

Toole, J. M., Krishfield, R. A., O'Brien, J. K., Houk, A., Cole, S. T., and the Woods Hole Oceanographic Institution Ice-Tethered Profiler Program. (2016). Ice-Tethered Profiler observations: Vertical profiles of temperature, salinity, oxygen, and ocean velocity from an Ice-Tethered buoy system [Dataset]. NOAA National Centers for Environmental Information. doi:10.7289/v5mw2f7x

van Straaten, C., Lique, C., and Kolodziejczyk, N. (2024). The life cycle of the low salinity lenses at the surface of the Arctic Ocean [Preprint]. *ESS Open Archive.* doi:10.22541/essoar.172408092.25227238/v1

Willmes, S., and Heinemann, G. (2016). Sea-ice wintertime lead frequencies and regional characteristics in the Arctic, 2003–2015. *Remote Sensing, 8*(1), 4. doi:10.3390/rs8010004